

**Investigations of Ultrafast Photoisomerization of Photochromic  
Molecular Switches by fs-Time-Resolved Transient Absorption  
Spectroscopy**

Dissertation  
zur Erlangung des Doktorgrades  
der Mathematisch-Naturwissenschaftlichen Fakultät  
der Christian-Albrechts-Universität zu Kiel

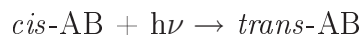
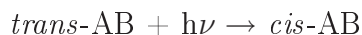
vorgelegt von  
Magdalena Foca, geb. Horoiu

Kiel 2005

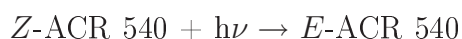
**To my parents**

## Abstract

The photoinduced isomerization of *trans*- and *cis*- azobenzene



and the *cis-trans* photoisomerization of the furylfulgide:



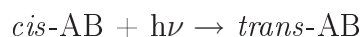
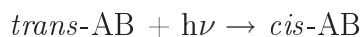
were studied with a pump-probe setup. The detection of the ultrafast transient absorption was realized using supercontinuum (SC) broadband probe pulses generated in sapphire or CaF<sub>2</sub>. A study of the cross-phase modulation showed that the SC could be described as linearly chirped pulses. Stimulated Raman amplification contribution was used to find the best setting for the pulse compression for the NOPA pump pulses.

The photoinduced isomerization of azobenzene in CCl<sub>4</sub> and ethanol at room temperature was studied after excitation at  $\lambda_{pump} = 466$  nm and  $\lambda_{pump} = 387$  nm. In the first case ( $\lambda_{pump} = 466$  nm), two wavelength-independent decay components of  $\overline{\tau}_1 = 0.52(2)$  ps and  $\overline{\tau}_2 = 3.22(2)$  ps were found, in agreement with previous work. The shortest time constant was interpreted as very fast motion of the excited state wavepacket out of the Franck-Condon region and ultrafast conversion to the  $S_0$  state *via* a conical intersection (CI), the second component was attributed to molecules that do not take the direct path. A much weaker third component of  $\tau = 18$  ps only found at  $\lambda = 510$  nm was assigned to the relaxation of vibrationally hot molecules in the  $S_0$  state. For excitation at  $\lambda_{pump} = 387$  nm leading to  $S_2$  state, three decay components with  $\overline{\tau}_1 = 0.08(5)$  ps,  $\overline{\tau}_2 = 0.4(3)$  ps and  $\overline{\tau}_3 = 13(3)$  ps were found. The fastest component ( $\tau_1$ ) could be related to the conversion from the  $S_2$  to the  $S_1$  state. The second decay time ( $\tau_2$ ) was attributed to motion in the  $S_1$  state towards the  $S_1/S_0$ -CI and the slowest component was assigned to cooling of vibrationally hot molecules in  $S_0$  state. It is not clear why, in contrast to literature, no  $\tau \approx 3$  ps component was observed.

The photoisomerization of the furylfulgide *Z*-ACR 540 was studied after excitation at  $\lambda_{pump} = 387$  nm in toluene and ethanol. In toluene, a short-lived component only present within the first 0.3 ps and a long lived second component were found. The latter had a rise time of  $\tau = 16$  ps and did not decay within 136 ps. That component was also observed in pure toluene and was assigned to the photoinduced formation of toluene excimers. In ethanol only one single fast decay component of  $\tau = 248(2)$  fs was found. The time scale of the process could be interpreted as motion from the  $S_1$  state to the  $S_0$  state *via* a CI.

## Kurzzusammenfassung

Die Photoisomerisierung von *trans*- und *cis*-Azobenzol



und die *cis-trans* Photoisomerisierung eines Furylfulgids



wurden untersucht. Die dazu notwendigen Abfrage- und Abtastpulse (Weißlicht, WL) wurden in Saphir oder  $\text{CaF}_2$  erzeugt. Eine Analyse der Kreuzphasenmodulation zeigte, dass die WL-Pulse in guter Näherung als linear gechirpt beschrieben werden konnten. Aus der stimulierten Raman-Streuung wurde die jeweils optimale Einstellung für die Kompression der NOPA-Anregungspulse bestimmt.

Die Photoisomerisierung von *trans*-Azobenzol wurde bei Anregung mit  $\lambda = 466$  nm und  $\lambda = 387$  nm in Tetrachlorkohlenstoff und Ethanol untersucht. Im ersten Fall konnten die Zeitprofile mit zwei von der Abfragewellenlänge unabhängigen Zeitkonstanten  $\bar{\tau}_1 = 0.52(2)$  ps und  $\bar{\tau}_2 = 3.22(2)$  ps beschrieben werden. Die kürzeste Zeitkonstante wurde als Herauslaufen des Wellenpakets aus der Franck-Condon-Region des angeregten Zustands mit anschließender direkter Konversion in den  $S_0$ -Zustand über eine konische Durchschneidung (KD) interpretiert. Die zweite Komponente wurde Molekülen zugeordnet, die nicht über diesen direkten Weg reagieren. Bei der Abfragewellenlänge  $\lambda = 510$  nm tritt eine dritte, sehr viel langsamere Komponente mit  $\tau = 18$  ps auf, die der Relaxation von schwingungsangeregten Molekülen im  $S_0$ -Zustand zugewiesen wurde. Bei Anregung mit  $\lambda = 387$  nm, die in den  $S_2$ -Zustand führt, wurden drei Zeitkonstanten,  $\bar{\tau}_1 = 0.08(2)$  ps,  $\bar{\tau}_2 = 0.4(3)$  ps und  $\bar{\tau}_3 = 13(3)$  ps, ermittelt. Die schnellste Komponente ( $\tau_1$ ) wurde als Übergang aus dem  $S_2$ -Zustand in den  $S_1$ -Zustand interpretiert. Die zweite Komponente ( $\tau_2$ ) wurde der Dynamik im  $S_1$ -Zustand in Richtung der  $S_0/S_1$  KD zugeordnet. Die langsamste Komponente wurde als Abkühlung von schwingungsangeregten Molekülen im  $S_0$ -Zustand gedeutet. Es konnte nicht geklärt werden, warum im Gegensatz zur Literatur keine Komponente mit  $\tau \approx 3$  ps beobachtet wurde.

Die Photoisomerisierung des Furylfulgids *Z*-ACR 540, wurde nach Anregung mit  $\lambda = 387$  nm in Toluol und Ethanol untersucht. In Toluol wurden eine kurzlebige (innerhalb der ersten 0.3 ps) und eine langlebige Komponente beobachtet. Letztere hatte eine Anstiegszeit von  $\tau = 16$  ps und blieb bis zu 136 ps nahezu konstant. Diese Komponente konnte der photoinduzierten Bildung von Toluol-Excimeren zugeordnet werden. In Ethanol wurde nur eine schnelle Komponente mit  $\tau = 248$  fs gefunden. Dieses Prozesses kann als Hinweis auf eine mögliche Beteiligung einer KD bei der Isomerisierung interpretiert werden.

# Contents

<b>1</b>	<b>Introduction</b>	<b>1</b>
<b>2</b>	<b>Ultrafast Photochromic Molecular Switches</b>	<b>4</b>
2.1	Photochromism . . . . .	4
2.2	Basic principles of photochemistry . . . . .	5
2.2.1	Photophysical processes . . . . .	6
2.2.2	Born-Oppenheimer and electronic adiabatic approximation . . . . .	7
2.2.3	Franck-Condon principle . . . . .	7
2.2.4	Nonadiabatic transition through conical intersection . . . . .	8
<b>3</b>	<b>Experimental section</b>	<b>10</b>
3.1	Principles of ultrafast spectroscopy . . . . .	10
3.1.1	The fs-Ti:Sa laser . . . . .	10
3.1.2	Characterization of Ultrashort Pulses . . . . .	12
3.1.3	Methods for Wavelength Conversion . . . . .	18
3.1.4	Supercontinuum laser pulses . . . . .	25
3.1.5	Pump-probe detection scheme . . . . .	28
3.2	Experimental setup . . . . .	30
3.2.1	Description of the Ti:Sa laser . . . . .	31
3.2.2	Pump pulse generation . . . . .	34
3.2.3	Probe pulse generation . . . . .	35
3.2.4	fs-pump-probe-setup . . . . .	39
3.3	Data acquisition . . . . .	40
3.3.1	Data fitting procedure . . . . .	43
<b>4</b>	<b>Results and Discussion</b>	<b>45</b>
4.1	Characterization of the fs-pump-probe transient absorption spectrometer . . . . .	45
4.1.1	Cross-Phase Modulation and time-zero correction . . . . .	46

4.1.2	Stimulated Raman Amplification . . . . .	61
4.1.3	Impulsive Stimulated Raman Scattering . . . . .	65
4.1.4	Conclusions and implications for the design of the TA setup . . . . .	68
4.2	Photoinduced <i>cis-trans</i> isomerization of azobenzene . . . . .	70
4.2.1	Background . . . . .	70
4.2.2	Results for <i>trans-cis</i> isomerization of azobenzene . . . . .	73
4.2.3	Results for <i>cis-trans</i> isomerization of azobenzene . . . . .	82
4.2.4	Discussion . . . . .	83
4.3	Photoinduced isomerization of Fulgides . . . . .	87
4.3.1	Results on photoisomerization of <i>Z</i> -ACR 540 . . . . .	88
4.3.2	Discussion . . . . .	95
<b>5</b>	<b>Summary</b>	<b>96</b>

# List of Figures

1.1	<i>Isomerization scheme of azobenzene.</i>	2
1.2	<i>Molecular structure and reaction scheme of Aberchrome 540.</i>	3
2.1	<i>a) keto-enol tautomerism of 2-hydroxybenzotriazoles; b) schematic diagram of the tautomerization mechanism.</i>	5
2.2	<i>Electrocyclic ring opening and closing reaction of 1,3,5-hexatriene.</i>	5
2.3	<i>Schematical representation of the Jablonski diagram.</i>	6
2.4	<i>a) Avoided crossing for diatomic molecules, b) conical intersection for potential surfaces with different symmetry.</i>	9
3.1	<i>Absorption and fluorescence spectra of Ti:Sa.</i>	11
3.2	<i>Schematic principle of the chirped pulse amplification.</i>	11
3.3	<i>Measured spectrum of the fundamental laser pulse. The center wavelength is <math>\lambda \approx 775</math> nm, the pulse width is 8 nm (FWHM).</i>	12
3.4	<i>Schematic diagram of the non-collinear autocorrelator. Two identical beams with the frequency <math>\omega</math> are overlapped in a non-linear crystal. The frequency doubled signal (SHG) is recorded as a function of the relative delay. The iris blocks the input beams and the SHG (indicated as blue arrows) generated by each input pulse alone.</i>	14
3.5	<i>Non-collinear autocorrelation function of the fundamental pulse (circles) together with a Gaussian fit (red line). The FWHM of the autocorrelation function is 210 fs.</i>	15
3.6	<i>Interferometric autocorrelation function of the fundamental pulse. The fringes in the autocorrelation trace wash out as the spectral phase becomes more complex.</i>	16
3.7	<i>FROG spectrogram (instantaneous frequency versus delay) for a negatively chirped pulse.</i>	17
3.8	<i>Schematic representation of the SPIDER set-up and principle.</i>	17
3.9	<i>Schematic view of the three wave mixing process.</i>	19

3.10	<i>Illustration of the effect of an external electrical field interacting with a non-linear medium.</i>	20
3.11	<i>In regular materials, due to the dispersion effect the refractive indices are different at different frequencies (a). However, in birefringent materials conditions can be achieved under which <math>n_o(\omega) = n_e(2\omega)</math>. This is indicated with the dashed line (b).</i>	21
3.12	<i>The refractive index ellipses of a negative uniaxial crystal. The angle under which the phase matching for the SHG takes place is indicated.</i>	22
3.13	<i>Non-collinear phase matching.</i>	22
3.14	<i>Schematic view of the non-collinear geometry phase matching.</i>	23
3.15	<i>Group velocities of signal and idler a) for non-collinear geometry and b) for collinear geometry.</i>	24
3.16	<i>Schematic view of the NOPA concept.</i>	24
3.17	<i>a) Intensity profile of a Gaussian laser beam. b) Illustration of the path of a laser beam that enters a transparent medium. Red arrows indicate the weak power beam path, whereas a high power beam will follow the path indicated by the green arrows.</i>	26
3.18	<i>a) Pulse with constant frequency. b) Pulse after passing through an optical medium with GVD.</i>	27
3.19	<i>Mechanism for SPM of a Gaussian laser pulse: a) time-dependent non-linear refractive index, b) time rate of frequency shift, c) time-dependent electrical field.</i>	28
3.20	<i>Schematic view of the pump-probe principle.</i>	29
3.21	<i>Schematic sketch of processes that can contribute to the TA signal: a) ground state bleaching; b) excited state absorption; c) hot ground state absorption; d) stimulated emission.</i>	30
3.22	<i>Schematic setup of the transient absorption experiment.</i>	31
3.23	<i>Schematic view of the SErF oscillator: WP = waveplates, PBS = polarization beam splitter, BRP = birefringent filter.</i>	32
3.24	<i>Photograph of the top level of the CPA-2001 laser system.</i>	32
3.25	<i>The so-called regen-trace from the regenerative amplifier. The four peaks represent the gradual amplification of the seed pulse in the cavity. Only after saturation, that corresponds to the fourth peak, the pulse is coupled out from the cavity.</i>	33
3.26	<i>Schematic view of the non-collinear optical parametric amplification.</i>	35



List of Figures

---

3.27	<i>Setup of the transient absorption experiment. <math>I</math> = variable diaphragm, <math>M</math> = off-axis parabolic mirror, <math>BS</math> = 5 mm fused silica plate, <math>L_1</math>: <math>f</math> = 50 mm for sapphire, <math>f</math> = 100 mm for <math>CaF_2</math>, <math>L_2</math>: <math>f</math> = 200 mm, <math>L_3</math>: <math>f</math> = 100 mm, <math>F_1</math>, <math>F_2</math> and <math>F_3</math> = filters, <math>Sh</math> 1, <math>Sh</math> 2 and <math>Sh</math> 3 = shutters. . . . .</i>	36
3.28	<i>Device for rotation of the calcium fluoride plate. . . . .</i>	37
3.29	<i>Photograph of a white light spot generated in sapphire. . . . .</i>	37
3.30	<i>a) Typical stability of white light generated in sapphire (black line) and calcium fluoride (red line) when 7500 laser shots are averaged. b) Stability of white light generated in sapphire when 4800 laser shots are averaged, under perfectly optimized conditions. . . . .</i>	38
3.31	<i>Normalized white light spectra generated in sapphire (red line) and calcium fluoride (black line). For the <math>CaF_2</math> supercontinuum an additional BG 18 filter reduces the intensity above 600 nm. . . . .</i>	39
3.32	<i>a) Photograph of the sample cell. b) Cross section of the sample cell. . . . .</i>	40
3.33	<i>Image of the dispersed probe and reference tracks on the CCD detector. . . . .</i>	41
3.34	<i>Spectral lines of the pen-ray lamp used for wavelength calibration. . . . .</i>	41
3.35	<i>Wavelength calibration using the pen-ray lamp and interference filters. . . . .</i>	42
4.1	<i>Simulated XPM signals for a linearly chirped probe pulse. The following parameters are used: <math>\omega_p = 3.943 \text{ fs}^{-1}</math>, <math>\tau_p = 50 \text{ fs}</math>, <math>\Omega_{pr} = 3.754 \text{ fs}^{-1}</math>, <math>\tau_{pr} = 250 \text{ fs}</math>, <math>\beta = 3.9 \times 10^{-4} \text{ fs}^{-2}</math>. . . . .</i>	47
4.2	<i>Contour plot representation of the XPM signal generated in a 0.2 mm sapphire window. The probe pulse is <math>CaF_2</math>-SC, the pump pulse is a compressed NOPA pulse centered at 478 nm (<math>E_{478nm} = 0.15 \mu\text{J}</math>). . . . .</i>	49
4.3	<i>XPM signal generated in a 0.2 mm sapphire window. The <math>CaF_2</math>-SC was focused with an achromatic lens. The red curves represent the fit of the XPM signal for linearly chirped probe pulse. The blue curves represent the pump-probe cross-correlation. See also text. . . . .</i>	50
4.4	<i>a) Experimental <math>CaF_2</math>-SC spectrum when using BG18 and OG515 filters, b) wavelength dependence of time-zero function <math>t_0</math>, c) cross-correlation width <math>\tau_{cc}</math> and d) amplitude of the XPM signal generated in a 0.2 mm sapphire window. . . . .</i>	51
4.5	<i>Autocorrelation function of the NOPA pulse <math>\lambda_{pump} = 478 \text{ nm}</math> (circles) together with a Gaussian fit (red line). . . . .</i>	52
4.6	<i>Contour plot representation of the XPM signal generated in pure <math>CCl_4</math>. The probe pulse is sapphire-SC, the pump pulse is a compressed NOPA pulse centered at 466 nm (<math>E_p = 0.45 \mu\text{J}</math>) . . . . .</i>	53

4.7	<i>XPM signal generated in pure CCl<sub>4</sub>. The sapphire-SC was focused with an off-axis parabolic mirror. The red curves represent the fit of the XPM signal for a linearly chirped probe pulse. The blue curves represent the pump-probe cross-correlation. For the fit parameters, see text. . . . .</i>	54
4.8	<i>a) Experimental sapphire-SC spectrum when using BG18 and OG515 filters, b) wavelength dependence of time-zero function <math>t_0</math>, c) cross-correlation width <math>\tau_{cc}</math>, d) amplitude of XPM signal generated in CCl<sub>4</sub>. . . . .</i>	55
4.9	<i>Time-zero function obtained from XPM signal generated in CCl<sub>4</sub>. The red line represents the linear fit and the blue line is the fit with a third order polynomial. . . . .</i>	56
4.10	<i>Contour plot representation of the XPM signal generated in pure ethanol. The probe pulse is the sapphire-SC, the pump pulse is SHG centered at 387nm (<math>E_{387nm} = 0.65 \mu J</math>) . . . . .</i>	57
4.11	<i>XPM signal generated in pure ethanol. The sapphire-SC was focused with an off-axis parabolic mirror. The red curves represent the fit of the XPM signal for a linearly chirped probe pulse. The blue curves represent the pump-probe cross-correlation. For the fit parameters, see text. . . . .</i>	58
4.12	<i>a) Experimental sapphire-SC spectrum when using BG38 and cut off 700 filters, b) wavelength dependence of time-zero function <math>t_0</math>, c) amplitude of XPM signal generated in a 0.2 mm sapphire window. . . . .</i>	59
4.13	<i>Dependence of the XPM signal generated in hexane on the pump energy (<math>\lambda_{pump} = 466 \text{ nm}</math>) for different probe wavelengths. The pump energy was varied using different neutral filters (NG11, NG5 and NG4) from 0.58 <math>\mu J</math> to 1.2 <math>\mu J</math> . . . . .</i>	60
4.14	<i>Time-zero behavior for SC generated in sapphire (blue lines and symbols) and CaF<sub>2</sub> (red lines and symbols) for different focusing: squares for use of an achromatic lens and stars for the off-axis parabolic mirror. . . . .</i>	61
4.15	<i>Comparison of different SRA profiles for a) and b) an inhomogeneous NOPA pulse, c) and d) a homogeneous NOPA pulse. . . . .</i>	62
4.16	<i>Autocorrelation function of the pump pulses (measured with the APE autocorrelator) used for generation of the SRA signals. The pulse widths (FWHM) are: a) 98fs, b) 59 fs, c) 75 fs, d) 85 fs. . . . .</i>	63
4.17	<i>The generated SRA signal in pure n-hexane and as inset the spectrum of the 466 nm pump pulse (measured with APE CCD spectrometer). . . . .</i>	64
4.18	<i>Dependence of the SRA signal from pure n-hexane on the pump energy (<math>\lambda_{pump} = 466 \text{ nm}</math>) at <math>\lambda_{probe} = 535 \text{ nm}</math>. . . . .</i>	65

---

4.19	Contour plot representation of the XPM and ISRS signal generated in pure $CCl_4$ . The probe pulse is sapphire-SC, the pump pulse is a compressed NOPA pulse centered at 466 nm ( $E_p = 0.65 \mu J$ ) . . . . .	66
4.20	XPM and ISRS signals of pure $CCl_4$ for different probe wavelengths. . . . .	67
4.21	Fourier spectra of the ISRS oscillations generated in pure $CCl_4$ . . . . .	67
4.22	Isomerization scheme of azobenzene. . . . .	70
4.23	UV-VIS absorption spectra of $0.1 \times 10^{-3}$ mol/l trans- and cis-AB solutions in $CCl_4$ . . . . .	71
4.24	Isomerization mechanism of AB. . . . .	72
4.25	Contour plot of the time corrected TA signal after 466 nm excitation of: a) pure $CCl_4$ and b) $5 \times 10^{-3}$ mol/l trans-AB in $CCl_4$ (XPM not subtracted). . . . .	74
4.26	Contour plot of the time corrected TA signal of $5 \times 10^{-3}$ mol/l trans-AB after subtraction of the XPM contribution: a) first 3 ps and b) full range up to 13 ps. . . . .	75
4.27	TA signal for the first 0.4 ps of trans-AB in $CCl_4$ after 466 nm excitation at different probe wavelengths. The blue lines represent the measured signal of trans-AB in $CCl_4$ ; the green lines represent the solvent signal; the circles give the subtracted signal; the red lines are the fits. . . . .	76
4.28	TA signal of trans-AB in $CCl_4$ after 466 nm excitation for $\lambda_{probe} = 510$ nm (a)) and $\lambda_{probe} = 535$ nm (b)). . . . .	77
4.29	TA signal of trans-AB in $CCl_4$ after 466 nm excitation for $\lambda_{probe} = 550$ nm (a)) and $\lambda_{probe} = 560$ nm (b)). . . . .	78
4.30	Contour plot of the $\chi^2$ -values for fits of the $\lambda = 535$ nm data. . . . .	79
4.31	Contour plot of the time corrected TA signal of $5 \times 10^{-3}$ mol/l trans-AB after 387 nm excitation (XPM subtracted): a) first 3 ps and b) full range up to 24 ps. . . . .	80
4.32	TA signal of trans-AB at 500 nm after 387 nm excitation: the upper part shows the corrected data together with the fit functions; the inset shows the raw TA data as blue line, the ethanol contribution as orange line, the corrected trans-AB signal as circles and the fit as red line. . . . .	81
4.33	Contour plot of time corrected TA signal of $5 \times 10^{-3}$ mol/l cis-AB in $CCl_4$ with excitation at 466 nm. . . . .	82
4.34	Temporal profile of cis-AB at $\lambda_{probe} = 540$ nm after 466 nm excitation. No attempt was made to fit the decay. . . . .	83
4.35	Molecular structure and reaction scheme of Aberchrome 540. . . . .	87
4.36	UV-VIS absorption spectra of Z- and E-ACR 540 in different solvents for a concentration of $1 \times 10^{-4}$ mol/l. . . . .	89

List of Figures

---

4.37	<i>Contour plot of the TA signal of pure toluene after 387 nm excitation (<math>E_{387} = 0.65 \mu\text{J}</math>: a) first 1.5 ps and b) full range (136 ps).</i>	90
4.38	<i>TA spectrum of pure toluene after 387 nm excitation at a delay of 100 ps . . .</i>	91
4.39	<i>Time corrected TA signal of Z-ACR 540 after subtraction of toluene contribution.</i>	91
4.40	<i>TA signal at <math>\lambda_{\text{probe}}=504</math> nm after 387 nm excitation of: the TA signal of the raw Z-ACR 540 data (green circles), pure toluene (black circles), Z-ACR 540 after subtraction of the toluene contribution (red circles).</i>	92
4.41	<i>Time profile of TA signal for pure toluene at <math>\lambda_{\text{probe}} = 504</math> nm after 387 nm excitation. As inset is shown Fig. 3 of Handschuh et al. and represents the TA signal of E-ACR 540.</i>	93
4.42	<i>Contour plot of the time corrected TA signal of Z-isomer in ethanol after 387 nm excitation (<math>E_{387} = 0.65 \mu\text{J}</math>, contributions of the ethanol are subtracted): a) first 1.2 ps and b) the complete measured dynamic (4.4 ps) . . . . .</i>	94
4.43	<i>Time profile of the TA signal for Z-ACR 540 (circles) at <math>\lambda_{\text{probe}} = 470</math> nm after 387 nm excitation. The red lines show the fit result. In the lower part the residual is shown.</i>	94

# 1 Introduction

The study of the kinetics of chemical reactions is an integral part of chemistry. In 1889 Arrhenius found empirically his famous equation for the reaction rate as a function of temperature [1], which has been used widely ever since. However, the Arrhenius equation does not give insight into the detailed molecular mechanism of a chemical reaction. For such a detailed description, the individual motion of the nuclei during the reaction is of interest. This motion occurs on the time scale of molecular vibrations, which is of the order of 100 fs or even less. Ultrafast pulsed laser techniques have enabled researchers to explore the molecular dynamics on this time scale by spectroscopic experiments. Since the first laser was invented in 1960 [2], the duration of the shortest laser pulses has decreased tremendously [3, 4, 5, 6]. The first fs-pulses became available in the 1980s [7], and even attosecond pulse are in use today [8].

Femtosecond spectroscopy has become an important tool for the study of chemical reaction dynamics and has been rewarded with a Nobel prize to A. Zewail in 1999 [9]. Among the many reactions studied are biologically relevant elementary processes of photosynthesis [10, 11], *cis-trans* isomerization of rhodopsin which is the basis of vision [12, 13, 14], or the mechanism of radiationless deactivation of the nucleobases and the nucleosides [15, 16, 17]. Much of the interest into the photoinduced molecular dynamics also arises from the desire to gain insight into the processes that are the basis for functional molecules in present and future applications such as light-driven switches [18] or molecular machines [19, 20].

Since no electronic device is fast enough for detection at the fs time scale, ultrafast spectroscopy is performed using a so-called pump-probe scheme, where first a pump pulse excites the sample and sets the point of time zero. Then, the temporal evolution of the system is interrogated with a series of temporally delayed probe pulses. A variation of the delay between the pump and probe pulses can be achieved by simply changing the relative optical path length of the pump *versus* the probe beam. Many different ultrafast spectroscopical methods have been developed, such as time-resolved mass-spectrometry [21, 22], time-gated fluorescence detection by up-conversion [23, 24] and transient absorption [25, 26]. In this thesis, the popular method of transient absorption detection is used.

Suitable ultra-broadband probe pulses can be generated by focusing femtosecond pulses into transparent non-linear optical materials, the so-called supercontinuum generation [27]. The

complex process is still not fully understood and involves a variety of non-linear optical phenomena [27, 28]. Another complication in transient absorption experiments are the coherent contributions to the detected signal due to the interaction of the pump and probe pulses inside the sample at zero time delay, such as cross phase modulation, stimulated Raman scattering and others. For the desired temporal resolution, a thorough characterization of the relevant parameters is required.

It was the goal of this work to set up an experiment for ultra-broadband detection of the transient absorption on a time scale of 100 fs and less. Typical absorption changes of photoexcited molecules are small and can be of the order of only one part per thousand or even less [29, 30, 31]. The reliable detection of such small signals with femtosecond resolution is a major experimental challenge that is usually tackled in a pump-probe-reference setup [25]. This is to be combined with a broadband spectral range of probe wavelengths for a complete detection of the ultrafast dynamics.

In this thesis, the method of transient absorption is applied to study the molecular dynamics of selected photochemical switches [19, 32]. A detailed knowledge of the underlying dynamics of the switching process is essential for the construction of improved functional molecular devices and might even open up new applications.

The photoinduced *cis-trans* isomerization of azobenzene (AB) was studied first. Figure 1.1 shows the isomerization from *trans*-AB to *cis*-AB and back. The isomerization can be induced

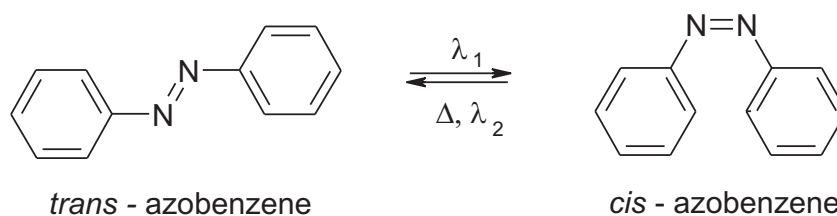


Figure 1.1: *Isomerization scheme of azobenzene.*

by irradiation at UV and visual wavelengths and is basis for the high application potential of azobenzenes. For example, ABs have been used to induce conformational changes in proteins, phase transitions in liquid crystal systems and emulsions, or construct so-called "nano-muscles" [33, 34, 35, 36, 37]. Despite much experimental and theoretical work (see *e.g.* [38, 39]) the exact mechanism of the isomerization is still not fully understood.

The second reaction of interest in this thesis is the photoinduced ring opening and closure of fulgides [40, 41, 42]. The reaction scheme of the fulgide Aberchrome 540 (ACR 540) (full name: 1-[1-(2,5-dimethyl-3-furyl)ethylidene]-2-isopropylidensuccinimide) is shown in Fig. 1.2. This class of molecules shows a reversible light-induced change (photochromism) in the absorption spectrum. Since the switching cycle can be repeated many times without significant

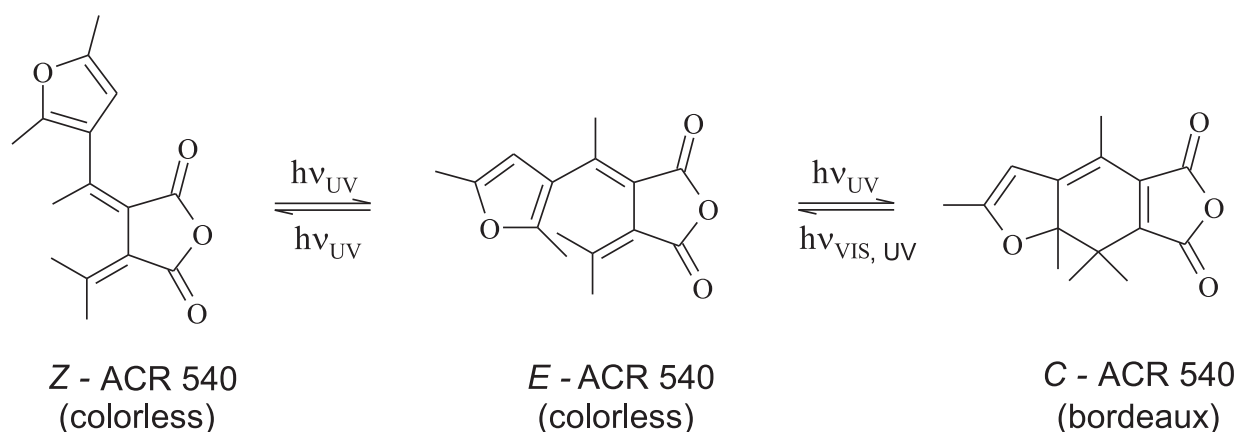


Figure 1.2: *Molecular structure and reaction scheme of Aberchrome 540.*

photodamage, fulgides are promising candidate molecules for use as optical memory devices. The electrocyclic reaction has not been studied extensively by ultrafast spectroscopy before. Only a few studies are available [43, 44, 45] and not much is known about the details of the underlying molecular dynamics, such as the nature of the excited states that are involved. For the  $Z - E$  isomerization, which is studied in this thesis, no ultrafast measurements are known.

The work presented in this thesis is organized as follows: Chapter two includes sections on photochromism and photochemistry. In the first section of chapter three, relevant aspects of ultrafast spectroscopy will be described. Details of the experimental setup and data acquisition procedures are given in section two and three of chapter three. The results and their discussion are given in chapter four. It is divided into three parts, one covering the generation of the supercontinuum probe pulses and the other two the photoisomerizations of respectively: AB and the  $Z$  isomer of the fulgide Aberchrome 540.

# 2 Ultrafast Photochromic Molecular Switches

Miniaturization of electronic devices to achieve faster data processing and higher data storage capacities is a major trend in information technology. However, it is anticipated that soon the physical limits of lithography will be reached. The use of molecules as building blocks opens a promising route to construct nanoscale devices. In this context photochromic molecules, which can act as bistable optical switches are at the centre of interest. For an optimal design of the devices, not only the static properties of the compounds must be known, but also a detailed understanding of the ongoing photophysical and photochemical processes is crucial.

The dominance of the desired photochromic reactions over possible side reactions, which is basis for repeated photochromic cycles and low photochemical fatigue, requires large rate constants, *i. e.* efficient ultrafast mechanisms for intramolecular conversion such as the molecular dynamics at conical intersections. The next section gives a brief introduction to photochromism, and in the following sections important photochemical and photophysical concepts are described.

## 2.1 Photochromism

Photochromism is the light induced reversible change in the absorption spectrum of molecules. A variety of compounds such as stilbenes, spiropyranes, diarylethenes, azobenzenes and fulgides display photochromism. The typical processes involved are the *cis-trans* isomerization, the electrocyclic ring closure or opening and the keto-enol tautomerism.

It has been found experimentally that all three types of photochromic processes have in common to happen on ultrafast time scales. The photochromism of 2-hydroxybenzotriazoles, for example, is based on keto-enol tautomerism [46, 47, 48]. Upon photoexcitation, these molecules undergo a complete photochromic cycle that is finished within less than a picosecond (see Fig. 2.1). The underlying ultrafast proton or hydrogen transfer that occurs in the excited



state (ESIPT<sup>1</sup>, [49]) is one of the most elementary processes in chemistry and is interesting in its own right. Likewise, the archetypical electrocyclic ring opening of 1,3-cyclo-hexadiene to 1,3,5-hexatriene (Fig. 2.2) occurs on a time scale of less than 100 fs [50, 51, 52].

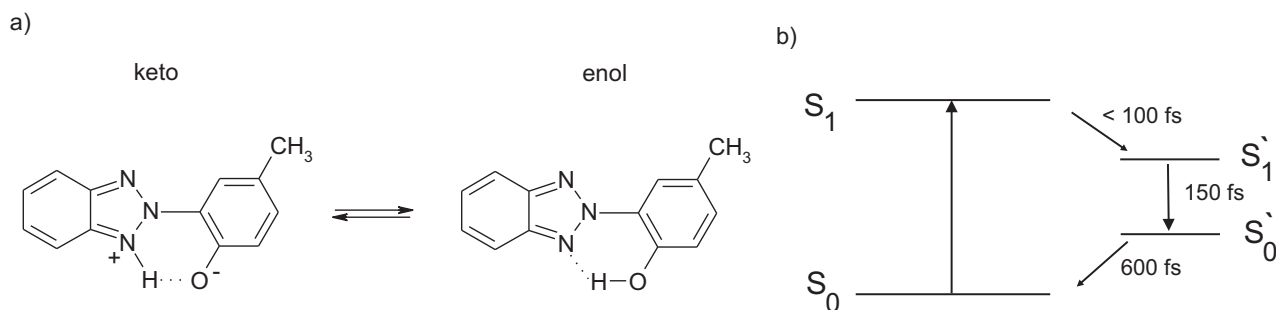


Figure 2.1: a) *keto-enol tautomerism of 2-hydroxybenzotriazoles*; b) *schematic diagram of the tautomerization mechanism*.

For azobenzenes and Aberchrome 540, which have been investigated in this work, the occurrence of sub-picosecond time scales of the molecular dynamics has been established previously as well (for a detailed account, see Chapter 4). Photochromism therefore emerges as a phenomenon that is intimately connected to ultrafast fundamental photochemical processes. It is interesting not only from the view-point of applicability but for fundamental theoretical reasons also, since the systems are easily accessible to optical methods precisely because of their photochromism.

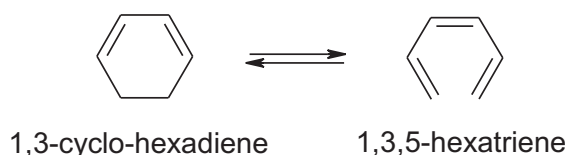


Figure 2.2: *Electrocyclic ring opening and closing reaction of 1,3,5-hexatriene*.

## 2.2 Basic principles of photochemistry

Photoinduced chemical reactions involve electronically excited states. This means that the pathways and principles governing their outcome can be quite different from those known from the classical thermal reactions. In the remainder of this chapter the most important concepts will be introduced briefly.

<sup>1</sup>Excited State Intramolecular Proton Transfer

### 2.2.1 Photophysical processes

When electromagnetic radiation of energy  $E = h\nu$  interacts with a molecule, a photon can be absorbed exciting the molecule from its ground state  $S_0$  to excited states  $S_{n>0}$ . The following relaxation to the ground state can be radiationless or accompanied by the emission of a photon with the same or even smaller frequency (Stokes shifts). In the radiationless case the excess energy can be redistributed intramolecular or transferred to a different molecule by an intermolecular collision. These processes are usually illustrated by means of the so-called Jablonski diagram. Figure 2.3 shows a simplified energy levels scheme in the Jablonski diagram and describes the possibilities of an excited molecule to emit energy.

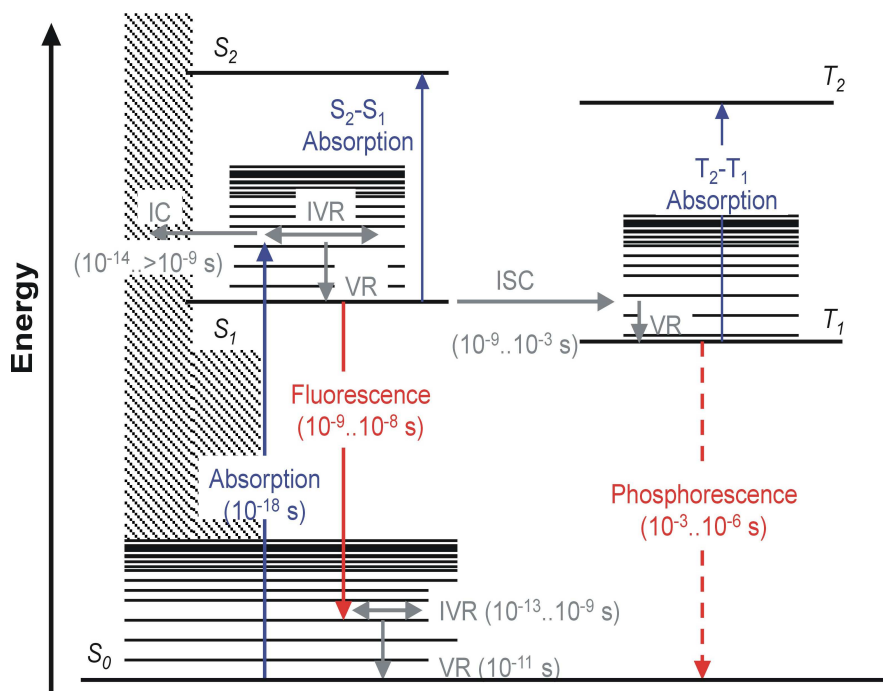


Figure 2.3: Schematical representation of the Jablonski diagram.

Radiation emitted during a relaxation can be of two types. It can occur from the first excited state  $S_1$  (fluorescence) or from an excited triplet electronic state  $T_1$  (phosphorescence). The typical lifetime of fluorescence is almost  $10^{-9}$  -  $10^{-8}$  s, while for phosphorescence it is in the order of  $10^{-6}$  s up to hours (since the transition is spin forbidden). The radiationless transitions can take place *via* three different schemes:

Internal conversion represents the radiationless transition from a highly excited state to a highly vibrationally excited level of an other lower electronic state of the same multiplicity. It

is also possible that the transition takes place to one of a lower electronic state, which usually undergoes deactivation to its lower vibrational level.

When collisions between molecules occur, an energy transfer to the environment takes place. Since the molecule loses vibrational energy, this process is called vibrational relaxation.

Intersystem crossing describes the spin forbidden transition of a system between two electronic states with different spin multiplicities. These transitions are facilitated *via* spin-orbit coupling.

### 2.2.2 Born-Oppenheimer and electronic adiabatic approximation

To describe the electronic states of a molecule, the Schrödinger equation  $\hat{H}\psi = \epsilon\psi$  has to be solved. The Hamilton operator  $\hat{H}$  can be written as

$$\hat{H} = \hat{T} + \hat{V} = \hat{T}_e(r) + \hat{T}_N(R) + \hat{V}(r, R),$$

where  $\hat{T}_e$  and  $\hat{T}_N$  are the kinetic energy operators for the electrons and nuclei as functions of the electronic ( $r$ ) and nucleic coordinates ( $R$ ), respectively, and  $\hat{V}$  is the potential energy operator including electron repulsion, nuclear repulsion and electron-nuclear attraction.

In the Born-Oppenheimer approximation the slow motion of the nuclei is separated from the fast motion of the electrons. The fast electrons can be assumed to follow the slow nuclei adiabatically. Thus, for every nuclear configuration  $R$ , there is an electronic wavefunction that depends on the nuclear coordinates  $R$  only parametrically. The solution of the Schrödinger equation therefore results in an energy-landscape with a potential eigenvalue for every set of nucleic coordinates  $R$ . The so called potential energy surface (PES) is a  $3N - 6$  dimensional hypersurface for each electronic state.

However, if nucleic and electric properties couple strongly, the Born-Oppenheimer approximation (BOA) is no longer sufficient because it completely neglects the relevant coupling matrix. With regard to this work, especially the failure of the BOA to describe a potential degeneracy of two different electronic states is of importance and will be described next.

### 2.2.3 Franck-Condon principle

The Franck-Condon principle is based on the separation of the electronic and nucleic motion during a photoinduced electronic transition. The promotion of the electron into a higher electronic state upon excitation takes place on a time scale of  $\Delta t \approx 10^{-18}$  s. Since even fast intramolecular vibrations have a period of  $\Delta t \approx 10^{-15}$  s, the nuclei in the molecule may be considered as fixed during the excitation. When the potential energy is plotted as a function

of the  $3N - 6$  nucleic degrees of freedom, the excitation is therefore represented by a vertical transition to the excited state.

The concept divides a photochemically induced electronic transition into two parts. First the electron jump takes place around a rigid molecular frame and only afterwards the molecular geometry reacts on the new distribution of electron densities and relaxes by nucleic motion. The strength of the transition is determined by the overlap integral between vibrational state wavefunctions of the ground and excited electronic states at fixed nucleic coordinates. This concept is crucial for studies of molecular dynamics because the position above the ground state equilibrium geometry, the so called Franck-Condon region, defines the starting point of the ensuing photoinduced chemical dynamics.

## 2.2.4 Nonadiabatic transition through conical intersection

In the case of a diatomic molecule the PES of two electronic states (for example of the ground state and the first excited state) will intersect if the states have different (spatial or spin) symmetry. Otherwise, the perturbative mixing will lead to a repulsion and the curves will not cross. In the case of polyatomic molecules an intersection of two PES can be obtained, even if the relevant states have the same symmetry or spin multiplicity.

Avoided crossings and intersections can be rationalized by considering the perturbative coupling of the two states  $|\phi_1\rangle$  and  $|\phi_2\rangle$ . The energies  $E_1$  and  $E_2$  of the two states will change due to the mixing of the states according to

$$E_{1,2} = \frac{\mathbf{W}_{11} + \mathbf{W}_{22}}{2} \pm \sqrt{\left(\frac{\mathbf{W}_{11} - \mathbf{W}_{22}}{2}\right)^2 + \mathbf{W}_{12}^2}, \quad (2.1)$$

where  $W_{ij} = \langle \phi_i | \hat{W} | \phi_j \rangle$  are the matrix elements of the coupling matrix  $\mathbf{W}$  and  $\hat{W}$  is the coupling operator.

The degenerate case ( $E_1 = E_2$ ) occurs only if the square root vanishes, *i.e.* if

$$\mathbf{W}_{11} = \mathbf{W}_{22} \quad \text{and} \quad \mathbf{W}_{12} = 0. \quad (2.2)$$

While these conditions are fulfilled if the crossing states are of different spin or symmetry ( $\det \mathbf{W} = 0$ ), it is very unlikely for two states of the same spin and symmetry with only one degree of freedom. This leads to the well known principle of the avoided crossing (see Fig. 2.4 a)) for diatomic molecules.

In a polyatomic molecule, however, the PES has  $3N - 6$  dimensions. The additional degrees of freedom make it quite possible to have both of the above conditions fulfilled. The resulting

topology of the involved PESs resembles the form of a bicone with the point of degeneracy at the center (see Fig. 2.4 b)), hence the name "conical intersection" (CI). Due to the steep slope of the potential these conical intersections are very effective pathways for radiationless electronic transitions on a time scale of nuclear motion (*i. e.* femtoseconds). Since the nuclear motion goes along with a continuous change of the electronic configuration it is obvious that the BOA can not be applied to describe the nature of these transitions.

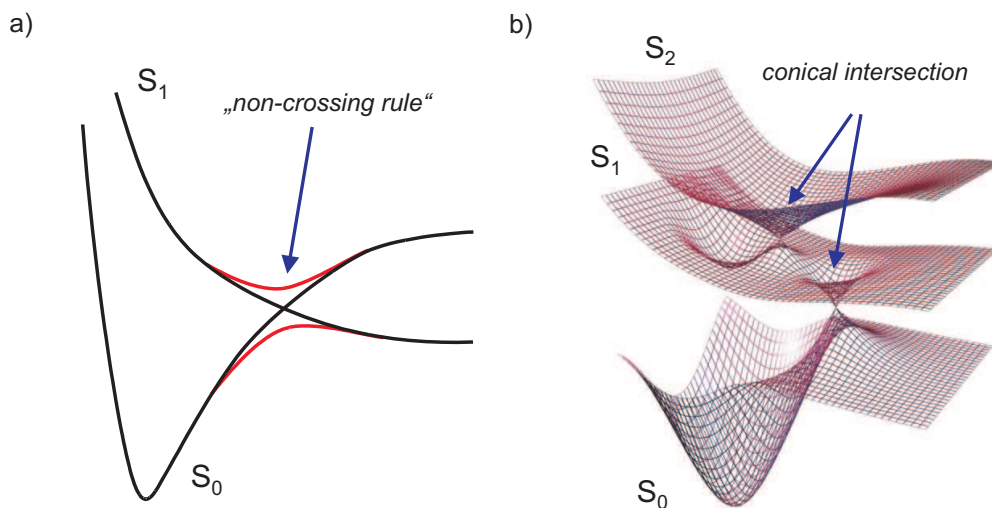


Figure 2.4: a) *Avoided crossing for diatomic molecules, b) conical intersection for potential surfaces with different symmetry.*

The importance of CIs has been established for many ultrafast reactions in recent years [53, 54, 55, 56], among them the reactions studied in this work *i.e.* *cis-trans* isomerization and electrocyclic ring closure.

# 3 Experimental section

## 3.1 Principles of ultrafast spectroscopy

The present section gives an overview of important aspects of ultrafast spectroscopy and is divided into five subsections. The first subsection deals with ultrashort (*i.e.* sub-picosecond) pulse generation, with special emphasis on the Clark-MXR CPA-2001 laser system used in the present work. The second subsection explains the specific spectral and temporal characteristics of ultrashort pulses and how they can be determined. Subsections three and four introduce reliable methods for spectral conversion of fs-pulses and describes how temporally shortened pulses are created. The methods described are Second Harmonic Generation (SHG), Non-collinear Optical Parametric Amplification (NOPA) and supercontinuum generation (SG). In the final subsection of this section different so-called pump-probe techniques are described that are used to conduct ultrafast spectroscopic experiments. The transient absorption technique is covered in detail as it is the one used in the present work.

### 3.1.1 The fs-Ti:Sa laser

The generation of ultrashort pulses relies on a process called mode-locking. Many longitudinal laser modes have to interfere constructively inside the laser cavity and a definite phase relation between all modes has to be maintained. Titanium ( $\text{Ti}^{3+}$ ) doped sapphire ( $\text{Al}_2\text{O}_3$ ) (from now on called Ti:Sa) is the most popular solid state material used in ultrashort pulse generation. Its absorption and fluorescence spectra are shown in Fig. 3.1. Ti:Sa has several favorable properties. First, it has a very broad gain bandwidth of approximately 700 - 1100 nm, with a peak at  $\lambda \approx 800$  nm, and this supports many longitudinal modes. Second, the optical Kerr-effect [4, 57, 58, 59] in Ti:Sa,

$$n = n_0 + \Delta n_{Kerr}(I) = n_0 + n_2 I(t), \quad (3.1)$$

leads to the formation of the so-called Kerr lens inside the laser medium and self-mode-locking [57, 60] can occur. The second effect of the Kerr-lens is the self-phase modulation (SPM) of the pulse, that leads to a spectral broadening of the pulse, which is required for the generation

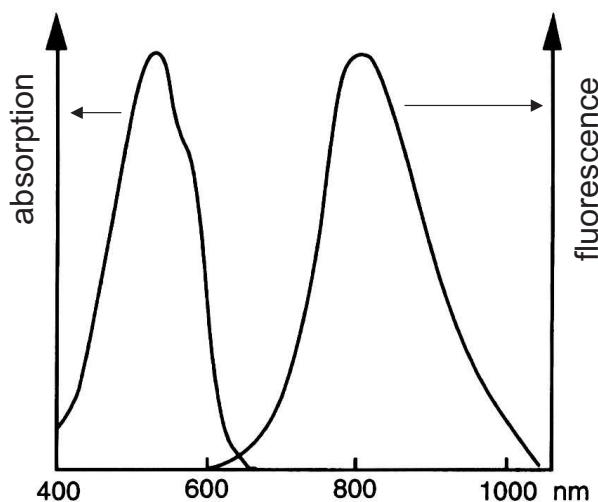


Figure 3.1: *Absorption and fluorescence spectra of Ti:Sa.*

of sub-ps-pulses.<sup>1</sup>

Typically, Ti:Sa is pumped by means of another laser with a wavelength of about  $\lambda = 500 - 550$  nm close to its absorption peak, for example an Ar ion laser or frequency doubled Nd:YLF, Nd:YVO or Nd:YAG lasers. Simple Ti:Sa based oscillators deliver pulses of approximative 100 fs duration with a repetition rate of  $\approx 50$  MHz and nJ pulse energies centered at  $\lambda \approx 800$  nm. These pulses then have to be amplified to be suitable for most spectroscopic experiments. The amplification is achieved by using the Chirped Pulse Amplification (CPA) scheme [61] inside a regenerative amplifier (RGA), which is shown schematically in Fig. 3.2. The weak input

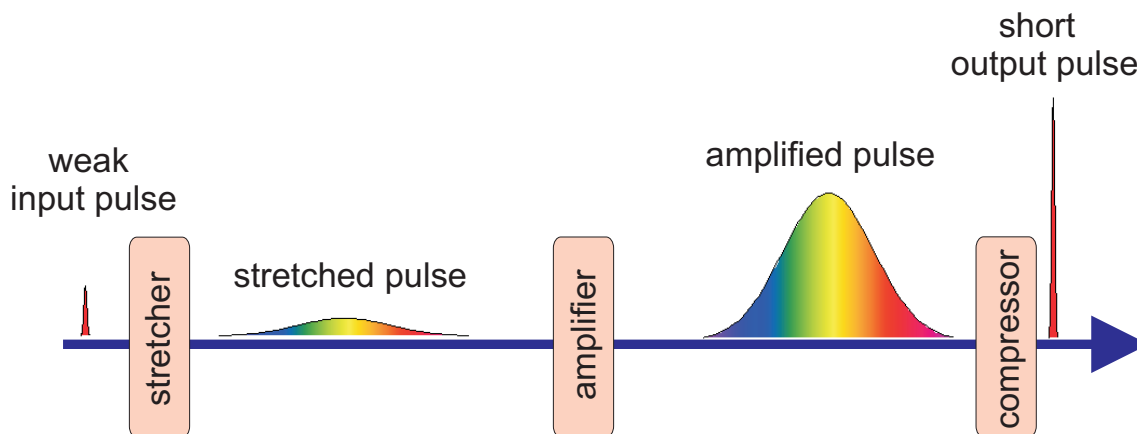


Figure 3.2: *Schematic principle of the chirped pulse amplification.*

pulse (also called seed pulse) is first stretched temporally and then injected into the amplifying

<sup>1</sup>This follows from the Fourier relation between the temporal and spectral widths of laser pulses.

medium (Ti:Sa). After a few round trips inside the RGA cavity, the gain is saturated, and the amplified pulse is coupled out. Finally, the amplified pulse is recompressed. The typical characteristics of the Clark-MXR CPA-2001 laser system used in this work are a pulse duration (full width at half maximum of the autocorrelation function, FWHM) of 210 fs, an output wavelength of  $\lambda \approx 775$  nm, a repetition rate of 1 kHz, and an output power of 800 mW.

### 3.1.2 Characterization of Ultrashort Pulses

Ultrashort pulses have to be characterized regarding both their spectral and temporal properties. For the spectral characteristic a simple CCD spectrometer is sufficient, since ultrashort pulses are spectrally broad. A typical spectrum of the laser fundamental recorded with a CCD spectrometer (APE-Berlin, type PulseScope) is shown in Fig. 3.3. As can be seen, the pulse spectrum is fairly Gaussian in shape, indicating almost perfect compression. The electric field

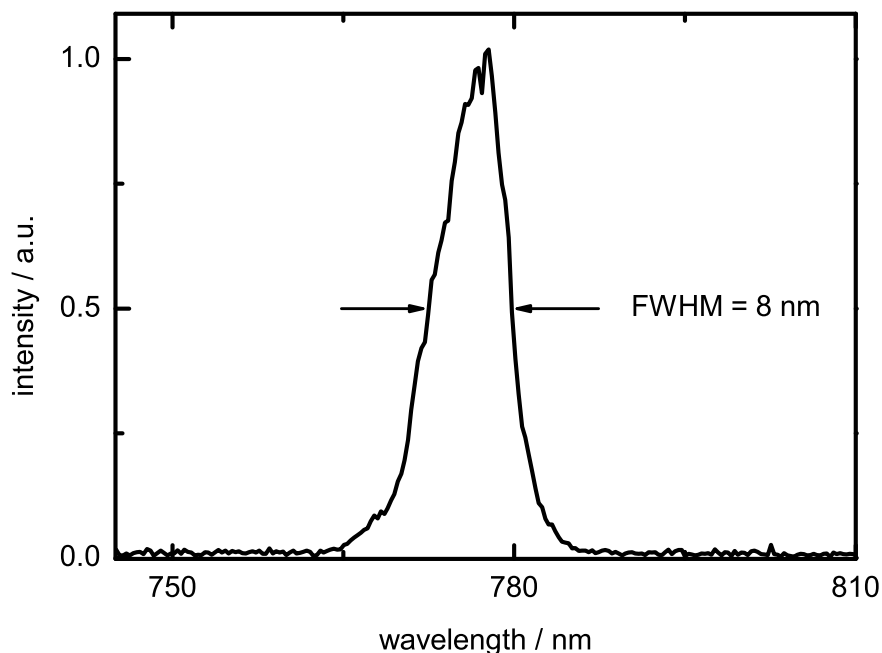


Figure 3.3: *Measured spectrum of the fundamental laser pulse. The center wavelength is  $\lambda \approx 775$  nm, the pulse width is 8 nm (FWHM).*

of ultrashort pulses is given by

$$E(t) \propto \frac{1}{2} \text{Re} \left\{ \sqrt{I(t)} \exp [i\omega_0(t) - \Phi(t)] + c.c. \right\}, \quad (3.2)$$



where  $\omega_0$  is the carrier frequency,  $\sqrt{I(t)}$  the amplitude, and  $\Phi(t)$  the phase term (c.c. denotes the complex conjugate). For a full characterization of an ultrashort pulse, both amplitude and phase must be known. This represents a problem, since even the fastest electronic devices have a response time that is much longer than the pulse duration. A number of techniques have been introduced to overcome this problem. In one way or another, they all rely on non-linear optical interaction of two or more pulse replicas with themselves. The required temporal resolution is provided by varying the relative spatial distance that the pulse replicas travel before interaction. For example, a relative delay of 10 fs corresponds to a distance of 3.3  $\mu\text{m}$ .

The simplest method of pulse characterization is autocorrelation [5]. For the autocorrelation measurement a pulse is split into two identical parts that are subsequently overlapped in a  $\beta$ -barium-borate (BBO) crystal for second harmonic generation. The optical path of one pulse is continually changed (scanned) to create a variable spatial delay. For this a Michelson interferometer setup is commonly used, as sketched in Fig. 3.4. Both beams are sent to two retro-reflectors mounted onto a small driver translation stage. When the stage is moved, one of the retro-reflectors introduces a temporal shift between the beams before they are overlapped in a non-linear BBO crystal (the optical paths are represented by solid and dashed lines in Fig. 3.4). If the path difference  $d$  is determined accurately, the time difference or temporal delay  $\tau$ , between the beams can be calculated [62] by multiplying the speed of the light  $c$  with the path difference  $\tau = 2cd$ .

The autocorrelation can be measured in the collinear or non-collinear geometry. In the non-collinear (or background free) geometry, that is shown in Fig. 3.4, the pulses are overlapped non-collinearly in the crystal. The autocorrelation function is given by the intensity of the generated second harmonic and can be calculated as follows:

$$I(\tau) = \int_{-\infty}^{+\infty} |(E(t)E(t - \tau))|^2 dt, \quad (3.3)$$

where  $\tau$  represents the time delay between the pulses.  $I(\tau)$  is commonly also called the intensity autocorrelation. A typical non-collinear autocorrelation for the fundamental pulse is presented in Fig. 3.5. The intensity of the autocorrelation is of Gaussian shape with a FWHM of 210 fs. The disadvantage of intensity autocorrelation is that information about the pulse phase is lost. Consider the Taylor expansion of the temporal phase  $\Phi(t)$  around  $t_0 = 0$  :

$$\Phi(t) = \Phi_0 + \Phi_1 \frac{t}{1!} + \Phi_2 \frac{t^2}{2!} + \dots \quad (3.4)$$

The first two terms in Eq. (3.4) are not important for the temporal shape:  $\Phi_0$  is a simple phase shift,  $\Phi_1$  simply shifts the pulse spectrally (without altering its temporal shape). However,

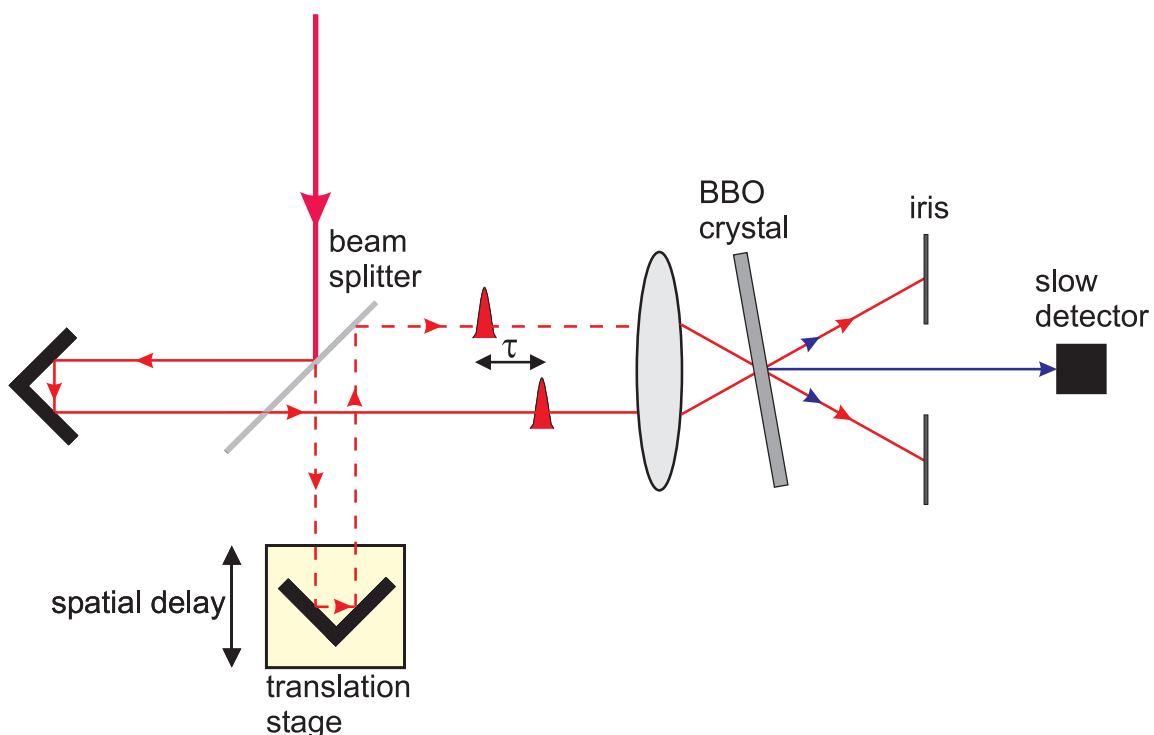


Figure 3.4: Schematic diagram of the non-collinear autocorrelator. Two identical beams with the frequency  $\omega$  are overlapped in a non-linear crystal. The frequency doubled signal (SHG) is recorded as a function of the relative delay. The iris blocks the input beams and the SHG (indicated as blue arrows) generated by each input pulse alone.

the quadratic temporal phase  $\Phi_2$ , affects the spectral and temporal properties of the pulse, since the instantaneous frequency

$$\omega_{inst}(t) \cong \omega_0 - \frac{d\Phi}{dt} \quad (3.5)$$

becomes time dependent, *i.e.* varies across the pulse. For negative values of  $\Phi_2$ , this so-called chirp is positive, and *vice versa*. Using non-collinear autocorrelation, the chirp of a pulse will remain unnoticed, since its only effect is a broadening of the autocorrelation function (which consequently gives the wrong values for the pulse duration). To obtain a meaningful value for the pulse duration with non-collinear autocorrelation, a certain pulse shape has to be assumed. Usually a Gaussian shape is taken and the full width at half maximum (FWHM) is quoted to characterize the pulse duration (see Fig. 3.5). Because of the time reversal symmetry of SHG intensity autocorrelations, asymmetric pulse shapes will remain undetected as well.

The phase information can be obtained by using collinear autocorrelation instead. In this case the two identical laser beams travel the same path and the second harmonic signal resulting from the interaction of the two beams in the BBO crystal, as well as the second harmonic

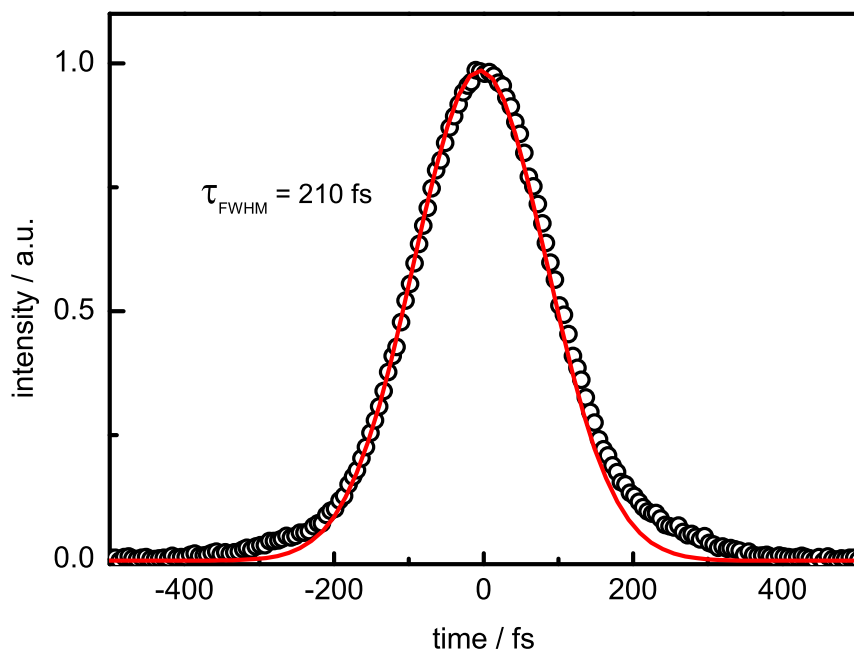


Figure 3.5: *Non-collinear autocorrelation function of the fundamental pulse (circles) together with a Gaussian fit (red line). The FWHM of the autocorrelation function is 210 fs.*

signal from each of the individual beams is detected. The recorded signal is given by

$$I_M(\tau) = \int_{-\infty}^{+\infty} |E(t) + E(t - \tau)|^2 dt. \quad (3.6)$$

$I_M(\tau)$  is also called the interferometric autocorrelation. Figure 3.6 shows a typical autocorrelation trace measured for the fundamental pulses of the Clark-MXR CPA-2001 laser system. The oscillations visible in Fig. 3.6 are at frequencies that correspond to the laser fundamental and the second harmonic. The problem of the interferometric autocorrelation is that even though in theory the phase information is available, in practice the autocorrelation cannot easily be determined with sufficient accuracy. Therefore, for the remainder of this work, non-collinear autocorrelation has been preferred with a spectral characterization of the pulses when necessary.

Simultaneous detection of amplitude and phase is possible using the frequency resolved optical gating [63] (FROG) technique. In the simplest variant, FROG is essentially a SHG autocorrelation that is measured not only as a function of the temporal delay, but also as a

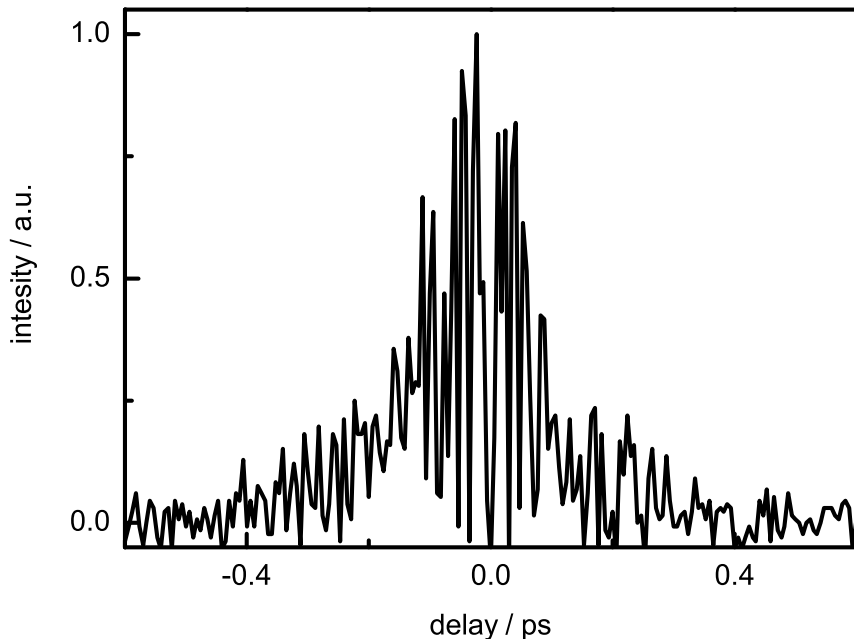


Figure 3.6: *Interferometric autocorrelation function of the fundamental pulse. The fringes in the autocorrelation trace wash out as the spectral phase becomes more complex.*

function of the frequency, by spectral dispersion of the resulting second harmonic intensity. The resulting signal is called FROG spectrogram or trace and contains information about the phase and amplitude. The detected signal can be expressed by the equation

$$I_{FROG}(\omega, \tau) = \left| \int_{-\infty}^{+\infty} E(t)g(t - \tau)e^{-i\omega t} dt \right|^2, \quad (3.7)$$

where  $g(t - \tau) = |E(t - \tau)|$  is the variable delay gate function (in this case: SHG). A typical SHG-FROG is shown in Fig. 3.7, with pseudo-color intensity coding. The different frequencies at different delay times are clearly visible. Depending on the gate function used, different variants of FROG can be realized apart from SHG-FROG that was described above. In polarization-gated (PG)-FROG, for example, one of the pulse replicas is sent through a pair of crossed polarizers and the other is polarization rotated by 45 degrees. The two pulses are then overlapped in a medium with a very fast third order susceptibility  $\chi^3$  such as fused silica. The gate function is  $|E(t - \tau)|^2$  and yields very intuitive traces that allow immediate assessment of the most important pulse properties simply by inspection.

Another method is the so-called spectral phase interferometry for direct electric field recon-

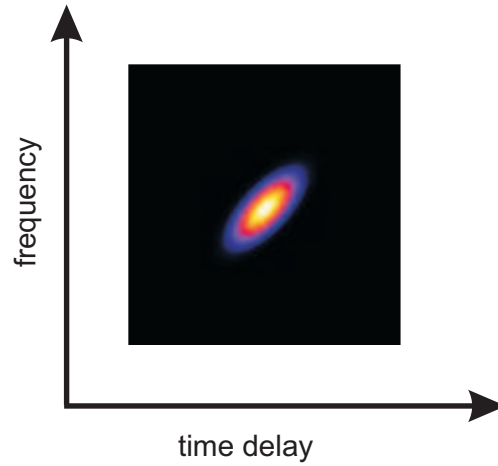


Figure 3.7: *FROG spectrogram (instantaneous frequency versus delay) for a negatively chirped pulse.*

struction (SPIDER) [64, 65, 66]. SPIDER is a self-referencing interferometric technique. The principle is sketched in Fig. 3.8. As in the case of autocorrelation and FROG, the pulse to be analysed is first split into two and the two replicas are delayed in time with respect to each other. To be able to measure the time-dependent spectral phase of a single pulse, a spectral shear is applied between two time-delayed pulse replicas. Typically, the shear is introduced by up-conversion of the two replicas with a stretched and chirped third pulse. Since the two replicas are up-converted by different parts of the chirped pulse, a spectral interference pattern results that allows to reconstruct the original pulses' properties.

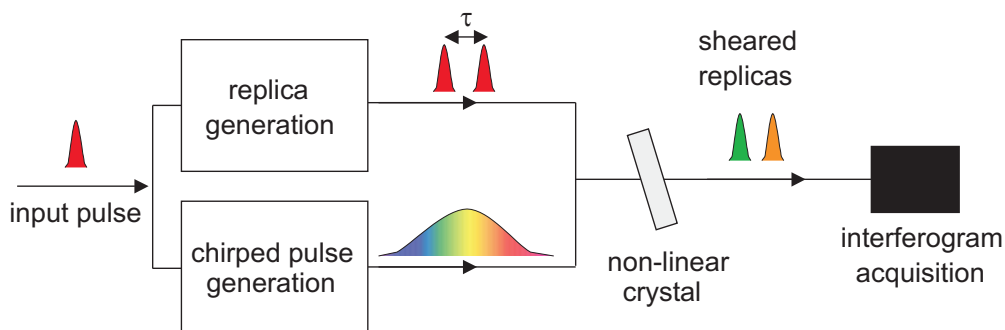


Figure 3.8: *Schematic representation of the SPIDER set-up and principle.*

### 3.1.3 Methods for Wavelength Conversion

Independent of what type of spectroscopy is performed, in order to investigate the molecular dynamics, it is required to convert the output of a laser ( $\lambda = 775$  nm in our case) to other wavelengths. Since the tuning of the laser fundamental is tedious and only a small wavelength range is accessible, techniques for external wavelength conversion are important. These all rely on non-linear optical effects in suitable materials and involve the non-linear polarization. In general, the polarization  $P$  of an optical medium is caused by the electric field  $E$  of the light traveling through it,

$$P = \epsilon_0 \chi E, \quad (3.8)$$

where  $\chi$  is the electrical susceptibility of the medium. At the very high light intensities frequently encountered with ultrashort pulses, the linear relation does not hold any more and the polarization  $P$  has to be expressed *via*

$$\begin{aligned} P &= \epsilon_0 \{ \chi^{(1)} E + \chi^{(2)} E^2 + \dots \} \\ &= \sum_n \epsilon_0 \chi^{(n)} E^n, \end{aligned} \quad (3.9)$$

where  $\chi^{(n)}$  is the  $n^{\text{th}}$  order susceptibility. In solids the first order susceptibility is  $\chi^{(1)} \approx 1$  m/V and is related to common phenomena such as absorption, refraction and reflection. The higher order susceptibilities are much smaller ( $\chi^{(2)}$  is of the order of  $10^{-12}$  m/V,  $\chi^{(3)}$  is of the order of  $10^{-19}$  m/V) [57]. This is why non-linear optical behavior is only observed at very high light intensities, which are nevertheless common with ultrashort pulses. As will be shown below,  $\chi^{(2)}$  is responsible for important phenomena such as second harmonic generation (SHG), sum and difference frequency generation (SFG, DFG) and optical parametric amplification (OPA).

#### 3.1.3.1 Three wave mixing

The term three wave mixing [67] relates to processes that involve the second order susceptibility  $\chi^{(2)}$  and the second order polarization  $P^{(2)}$ . The general situation with the incoming waves  $E_1(\omega_1)$ ,  $E_2(\omega_2)$ , and the wave that is emitted by the induced oscillating polarization,  $E_3(\omega_3)$ , is sketched in Fig. 3.9.

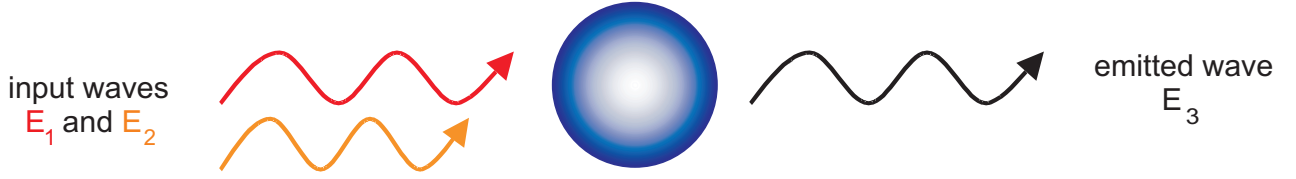


Figure 3.9: Schematic view of the three wave mixing process.

The induced  $2^{nd}$  order polarization is given by

$$\begin{aligned}
 P^{(2)} &= \epsilon_0 \chi^{(2)} (E_1 + E_2)^2 \\
 &= \epsilon_0 \chi^{(2)} [E_1 \cos(\omega_1 t) + E_2 \cos(\omega_2 t)]^2 \\
 &= \epsilon_0 \chi^{(2)} [E_1^2 \cos^2(\omega_1 t) + E_2^2 \cos^2(\omega_2 t) + 2E_1 E_2 \cos(\omega_1 t) \cos(\omega_2 t)] \\
 &= \frac{1}{2} \epsilon_0 \chi^{(2)} [E_1^2 \cos(2\omega_1 t) + E_2^2 \cos(2\omega_2 t) \\
 &\quad + 2E_1 E_2 \cos[(\omega_1 + \omega_2)t] + 2E_1 E_2 \cos[(\omega_1 - \omega_2)t] + (E_1^2 + E_2^2)].
 \end{aligned} \tag{3.10}$$

In Eq. (3.10), the induced polarization does not only contain components at the original frequencies  $\omega_1$  and  $\omega_2$ , but also the following additional frequencies:

$$\begin{aligned}
 P_{2\omega_1} &= \epsilon_0 \chi^{(2)} E_1^2 \cos(2\omega_1 t) \\
 P_{2\omega_2} &= \epsilon_0 \chi^{(2)} E_2^2 \cos(2\omega_2 t) \\
 P_{\omega_1 + \omega_2} &= 2\epsilon_0 \chi^{(2)} E_1 E_2 \cos[(\omega_1 + \omega_2)t] \\
 P_{\omega_1 - \omega_2} &= 2\epsilon_0 \chi^{(2)} E_1 E_2 \cos[(\omega_1 - \omega_2)t]
 \end{aligned} \tag{3.11}$$

This corresponds to light emitted at the new frequencies:

- $\omega = 2\omega_1$  and  $\omega = 2\omega_2$ : frequency doubling or second harmonic generation (SHG),
- $\omega = \omega_1 + \omega_2$ : sum frequency generation (SFG),
- $\omega = \omega_1 - \omega_2$ : difference frequency generation (DFG),
- $\omega = 0$ : optical rectification (DC).

Three wave mixing has great importance for frequency conversion of fixed frequency fundamental pulses. The generation of additional frequencies can also be understood in terms of a non-linear response of the medium to the external stimulus, caused by the large displacement of the electrons in their anharmonic potentials when the external electrical field is very large. This is illustrated in Fig. 3.10. Due to the non-linear response, the electrical field oscillating

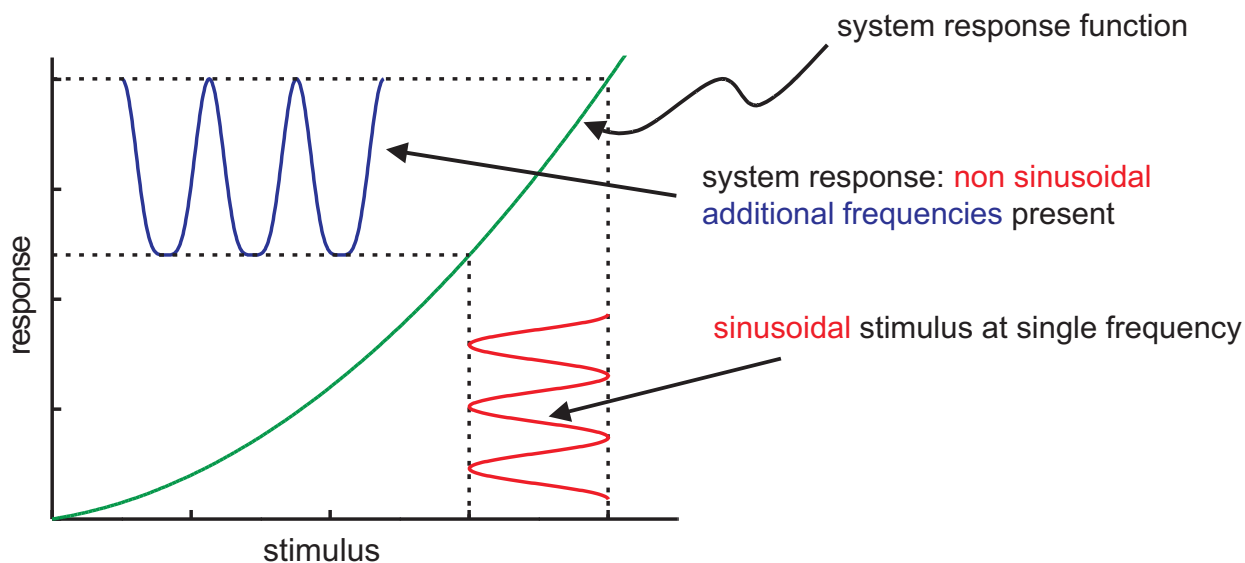


Figure 3.10: *Illustration of the effect of an external electrical field interacting with a non-linear medium.*

at the fundamental frequency  $\omega_0$  creates a polarization that can only be described using additional Fourier components at  $\omega = \omega_0$  (DC),  $\omega = 2\omega_0$  (SHG), *etc.* (see Eq. (3.10)). With respect to three-wave mixing, it is important to note that for media which have inversion symmetry,  $\chi^2$  is necessarily equal to zero.

### 3.1.3.2 Phase matching

Even if  $\chi^2$  is non-zero, efficient wavelength conversion (for example: SHG) *via* three wave mixing will in general not take place, because destructive interference between the fundamental wave and the second harmonic occurs, unless phase and group velocities of both wavelengths are matched [68]. The phase matching condition can be expressed as

$$\vec{k}_3 = \vec{k}_1 + \vec{k}_2, \quad (3.12)$$

where  $\vec{k}_3$  is the wave vector of the emitted wave and  $\vec{k}_1$  and  $\vec{k}_2$  are the wave vectors of the input waves. In the collinear case this leads to the condition  $n(2\omega) = n(\omega)$ , *i. e.* requires anomalous dispersion. In optically isotropic materials this occurs only in regions of absorption. In birefringent optical anisotropic media, however, the angular dependence of the refractive index of linearly polarized light can be exploited.

In uniaxial crystals, rays with a polarization vector in the principal plane, *i. e.* the plane that includes the crystal axis and the propagation direction, (ordinary or o-rays) and rays with their polarization vector perpendicular to the principal plane (extraordinary or e-rays)



have different refractive indices  $n_o(\omega)$  and  $n_e(\omega)$ . This is shown in Fig. 3.11. The important

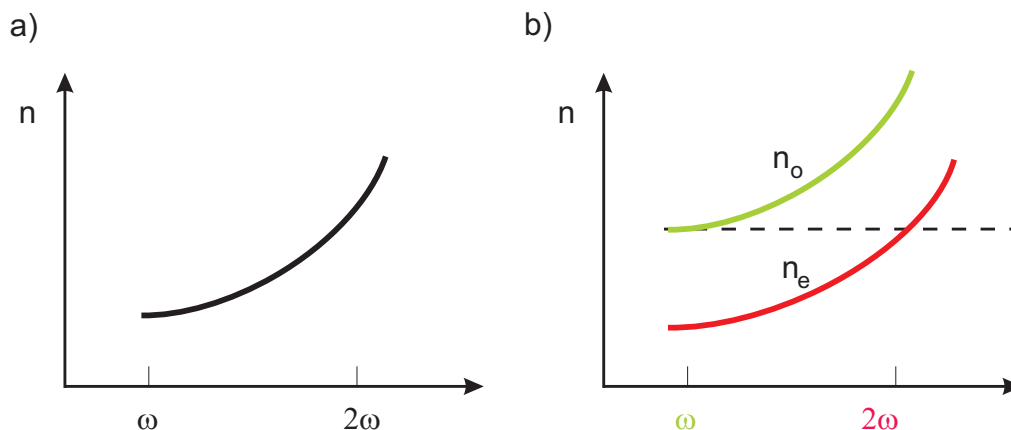


Figure 3.11: *In regular materials, due to the dispersion effect the refractive indices are different at different frequencies (a). However, in birefringent materials conditions can be achieved under which  $n_o(\omega) = n_e(2\omega)$ . This is indicated with the dashed line (b).*

point is that  $n_e(\omega)$  depends on the angle  $\theta$  between the propagation direction and the optical axis,

$$n_e(\theta) = n_o \left( \frac{1 + \tan^2 \theta}{1 + (n_o/n_e)^2 \tan^2 \theta} \right)^{1/2}. \quad (3.13)$$

By tuning this angle, also called the phase matching angle, it is possible to achieve  $n_e(2\omega) = n_o(\omega)$  for SHG. This situation is illustrated for collinear phase matching in Fig. 3.12. Phase matching is realized precisely where the  $n_e(2\omega)$  ellipse and the  $n_o(\omega)$  circle intersect.

To classify the phase matching conditions, it is common practice to denote the polarization of the three waves using the small letters “o” and “e”, with the two incoming beams first in order of increasing wavelengths and then the emitted beam. The above example would therefore be classified as “ooe”- phase matching. Equal polarizations of the incoming beams are classified as type I, unequal polarizations as type II phase matching.

The range and versatility of phase matching can be increased if non-collinear beam geometries are used. A case of non-collinear SHG is sketched in Fig. 3.13. Phase matching occurs again at the point of intersection. For a detailed description of the various facets of three wave mixing, such as walk-off bandwidth, conversion efficiency, temperature dependence, *etc.*, the reader is referred to Nikogosyan’s [69] book. Only the non-collinear parametric amplifier (NOPA) is described, because of its importance for generating tunable laser pulses.

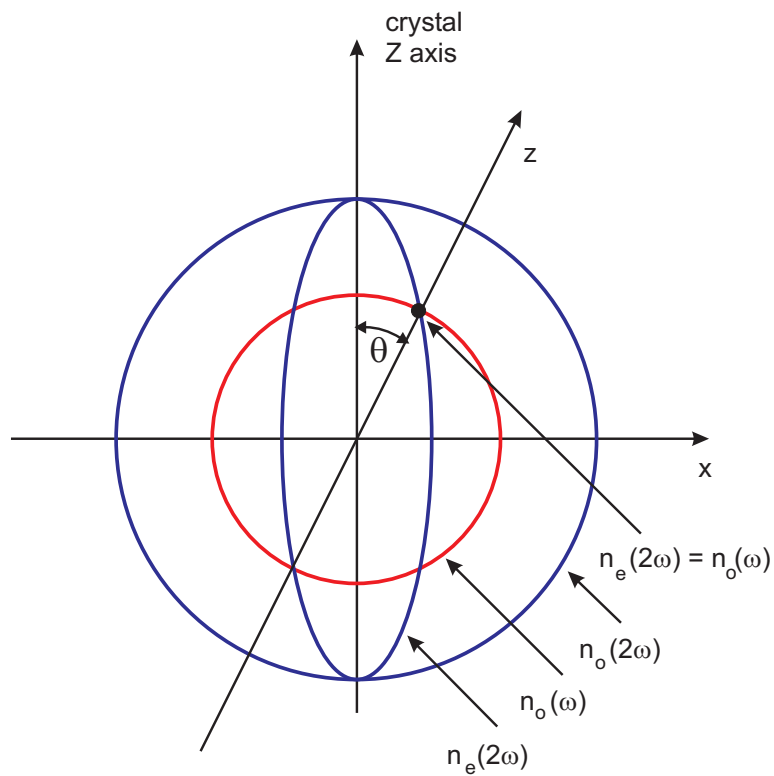


Figure 3.12: *The refractive index ellipses of a negative uniaxial crystal. The angle under which the phase matching for the SHG takes place is indicated.*

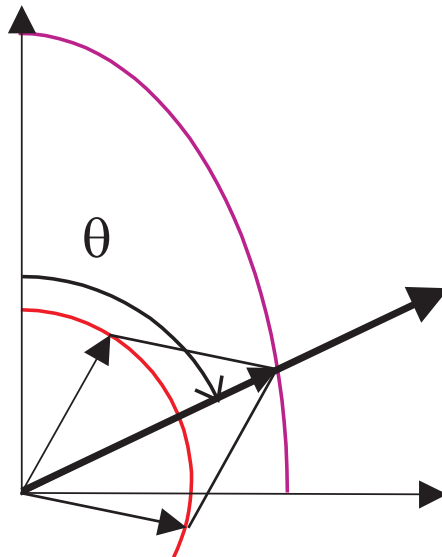


Figure 3.13: *Non-collinear phase matching.*

### 3.1.3.3 Non-collinear optical parametric amplifier (NOPA)

Optical parametric amplification (OPA) is a three-wave-mixing process [70, 71, 72, 73] closely related to difference frequency generation (DFG, see Sec. 3.1.3.1). In OPA, a short high intensity pump beam of frequency  $\omega_P$  amplifies a much weaker seed beam at  $\omega_S$  (the amplified seed is then called signal beam). The third beam from the DFG is called idler beam, at the frequency  $\omega_I$ . Energy conservation and the phase matching conditions apply as usual:

$$\begin{aligned}\omega_P &= \omega_S + \omega_I \\ \vec{k}_P &= \vec{k}_S + \vec{k}_I\end{aligned}\tag{3.14}$$

For broadband phase matching and highly efficient amplification of the seed pulses, the group velocities of the pulses must also be matched. This can be achieved in a non-collinear geometry, as sketched in Fig. 3.14, where  $\alpha$  is the non-collinear angle between signal and pump and  $\beta$  the angle between signal and idler. The group velocity matching (GVM) condition is given by

$$\vec{v}_S = \vec{v}_I \cdot \cos \beta,\tag{3.15}$$

where  $\vec{v}_S$  and  $\vec{v}_I$  are the group velocities of signal and idler. This means that GVM can be achieved if the signal group velocity equals the projection of the idler group velocity along the signal direction, as depicted in Fig. 3.15 a). In a collinear geometry (Fig. 3.15 b)) signal and

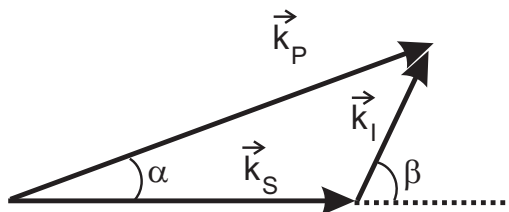


Figure 3.14: *Schematic view of the non-collinear geometry phase matching.*

idler get separated quickly, leading to pulse broadening and decreased bandwidth. This is not the case in the non-collinear geometry.

Fortunately, there are non-linear optical media that allow for simultaneous phase and group velocity matching, such as  $\beta$ -barium-borate (BBO) [69, 74]. Non-collinear optical parametric amplification (NOPA) was first realized by Gale [75, 76] and later extended by seeding the NOPA with a supercontinuum (SC) seed [70]. In this case, the amplifier bandwidth is governed by the relative amount of the chirp of the SC compared to the pulse length of the pump pulse. Ultrabroadband NOPAs can either be realized by reducing the SC chirp [77, 78] or by temporally broadening the pump pulse [79, 80]. The tunable NOPA works with deliberately

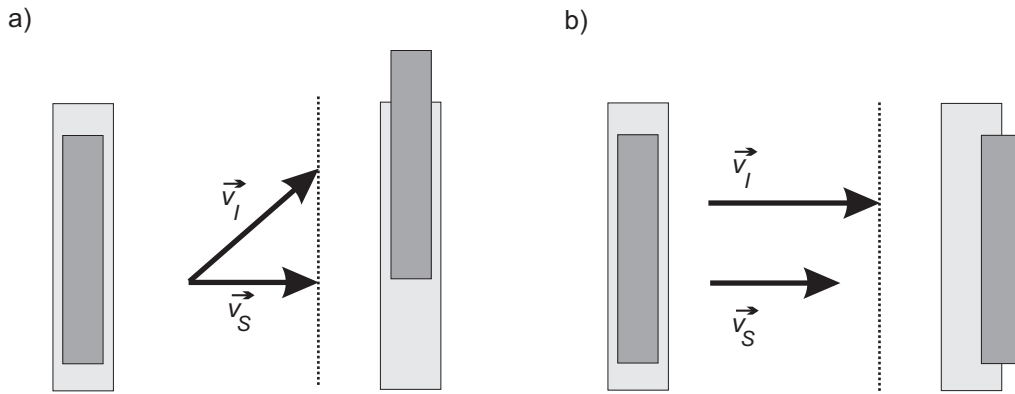


Figure 3.15: Group velocities of signal and idler a) for non-collinear geometry and b) for collinear geometry.

chirped SC sources, such that the temporal overlap between pump and SC seed occurs only for a limited wavelength range. Tuning can be achieved by simply delaying both pulses with respect to each other. Figure 3.16 shows the schematic setup of such a SC-seed tunable NOPA.

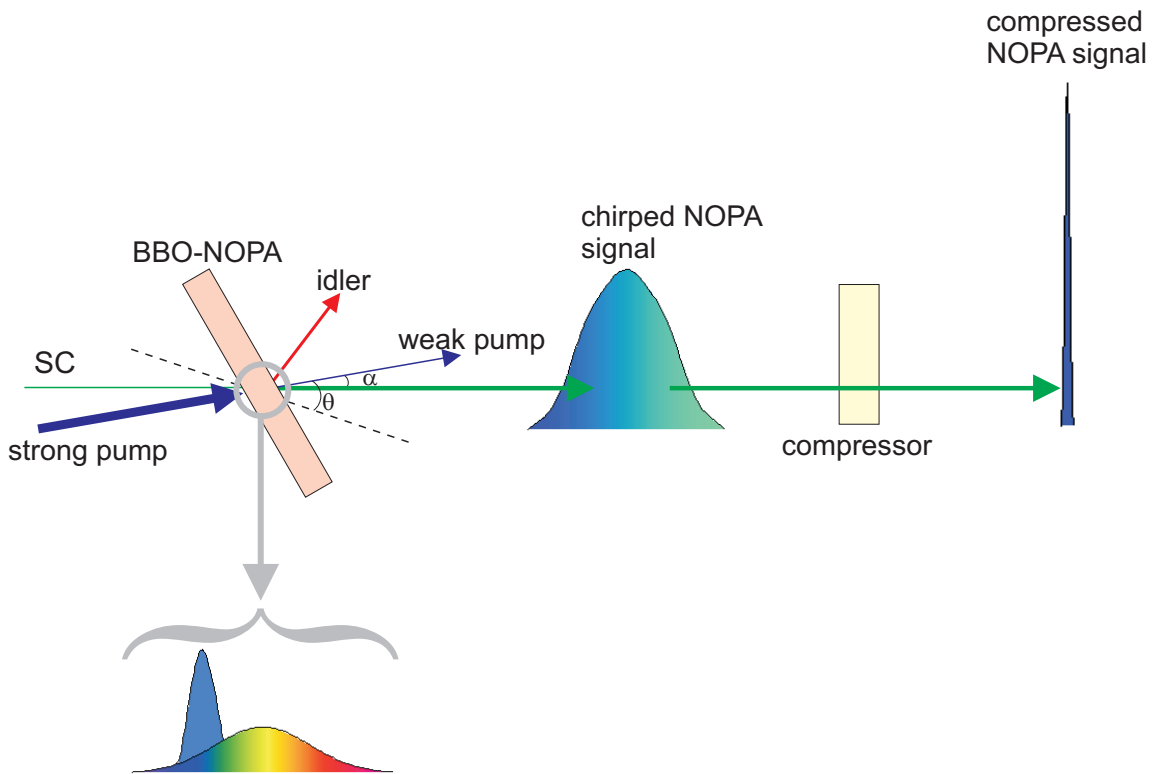


Figure 3.16: Schematic view of the NOPA concept.

The amplified pulses of a tunable NOPA have a pulse length that is comparable to the pump pulse length, and a chirp equal to the SC seed chirp. Since they are not transform limited,

*i.e.* their pulse length is longer than allowed by the Fourier transform of the spectrum, the NOPA pulses can be compressed using optical elements with negative group velocity dispersion (GVD), such as a prism compressor [81]. The negative GVD of the compressor compensates the chirp and thereby shortens the pulse.

### 3.1.4 Supercontinuum laser pulses

#### 3.1.4.1 General

Supercontinuum generation (SCG) [27] is the production of ultrashort broadband pulses ranging from the UV to the near IR (hence the term “white light pulses”), which is caused by the spectral broadening of intensive ultrashort laser pulses propagating through a transparent non-linear medium. SCG in liquids and solids was first observed by Alfano and Shapiro [82], who obtained a picosecond continuum that covered the entire visible range and extended into the NIR. The first fs-supercontinuum was obtained by Fork *et al.* in 1983 [83], and fs-SCG in gases was demonstrated shortly thereafter by Corkum [84]. In the past years SCG inside microstructured fibers has been established as another practical technique (see cited references in [27]).

#### 3.1.4.2 Mechanism of supercontinuum generation

Even though supercontinua are created routinely for use in broadband absorption experiments, optical parametric amplifiers or for optical pulse compression [27], they are still not fully understood. It is believed that the most important contribution is strong self-phase modulation (SPM) accompanied by self-steepening of the temporal envelope of the pulse [85], but four wave mixing and stimulated Raman scattering also play a role. In bulk media, self-focusing (SF, the spatial analogon to SPM) seems to be important as well, since the SCG power threshold corresponds to the critical power for SF [86, 87]. The very high intensities in the focus can lead to the formation of free electrons, either by multiphoton excitation (MPE) or by avalanche ionization, as was first suggested by Bloembergen [88]. In this model, the electrons contribute negatively to the index of refraction and thereby enhance SPM and prevent catastrophic self-focusing at the same time. Also believed to be involved in SCG are pulse splitting, cross-phase modulation, stimulated Raman emission and others (for a survey, see [82] and the special issue devoted to supercontinuum generation [89]). Both SPM and SF are consequences of the intensity dependent refractive index  $n(I)$ , *i.e.* the optical Kerr effect, that occurs in all transparent media:

$$n(I) = n_0 + n_2 I. \quad (3.16)$$

### 3.1.4.3 Self-focusing

Self-focusing occurs because of the spatial (ideally: radial) intensity profile of the laser beam and is illustrated in Fig. 3.17 for the case of a Gaussian profile. The intensity profile leads to

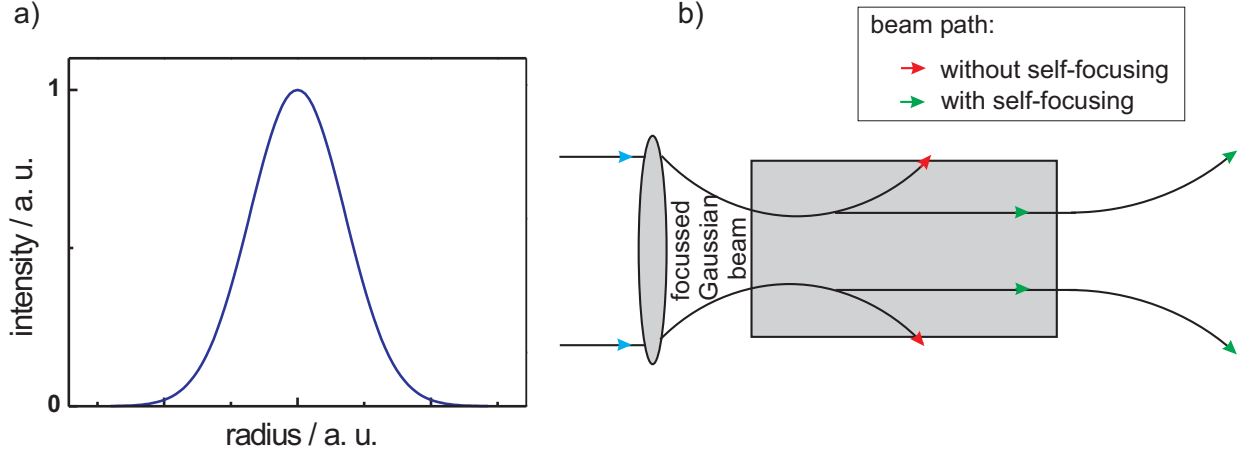


Figure 3.17: a) Intensity profile of a Gaussian laser beam. b) Illustration of the path of a laser beam that enters a transparent medium. Red arrows indicate the weak power beam path, whereas a high power beam will follow the path indicated by the green arrows.

a refractive index profile (the so called Kerr-lens) that focuses the beam. For SF to occur, the Kerr-induced focusing must exceed the diffractive effects, which for cw Gaussian beams [86] happens above the critical power  $P_{crit}$  of

$$P_{crit} = \frac{3.77\lambda^2}{8\pi n_0 n_2}, \quad (3.17)$$

where  $\lambda$  is the laser wavelength. The self-focusing distance  $z_f(P)$  is power-dependent,

$$z_f(P) = \frac{0.367ka_0^2}{[(\sqrt{P/P_{crit}} - 0.852)^2 - 0.0219]^{1/2}}, \quad (3.18)$$

where  $P$  is the beam power,  $k = 2\pi/\lambda_o$  is the wave number, and  $a_0 = D/2$  is the input beam radius at the  $1/e$  level of the intensity. In experiments, usually an external lens of focal length  $f$  is placed before the medium to achieve a reduced effective length (see Fig. 3.17 b)) via

$$\frac{1}{z_f^{eff}} = \frac{1}{z_f} + \frac{1}{f}. \quad (3.19)$$

The complete collapse of the focus does not occur due to the competing mechanisms (see above). For femtosecond pulses, it is believed that also the dispersion of the group velocity

(GVD) plays an important role. This is illustrated in Fig. 3.18. The difference in the group

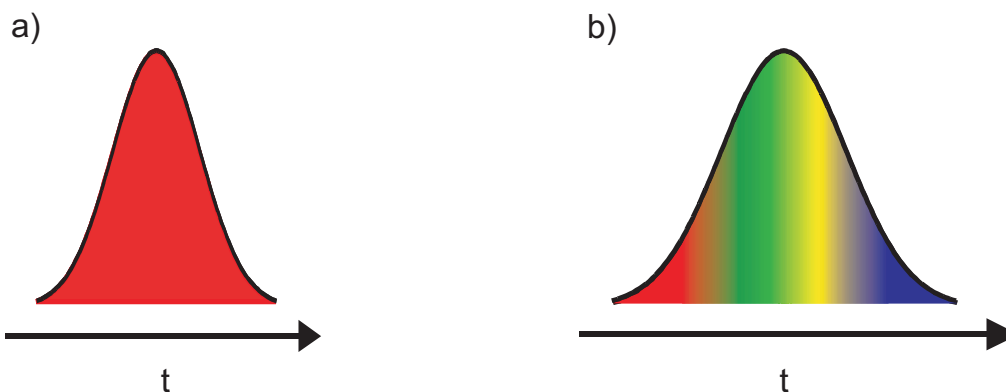


Figure 3.18: *a) Pulse with constant frequency. b) Pulse after passing through an optical medium with GVD.*

velocities at different wavelengths (“red” and “blue” in Fig. 3.18 b)) leads to a rearrangement of frequencies in the pulse and a temporal broadening that prevents the complete collapse.

#### 3.1.4.4 Self-phase modulation

Self-phase modulation (SPM) is the temporal equivalent of self-focusing. A laser pulse with a temporal intensity distribution  $I(z, \tau)$  propagating inside a Kerr medium accumulates a phase modulation that is proportional to the gradient of the intensity distribution,

$$\begin{aligned}\omega(z, \tau) &= \omega_0 - \frac{d\Phi}{dt} \\ &= \omega_0 - z \frac{\omega_0 n_2}{c} \frac{\partial I(z, \tau)}{\partial \tau},\end{aligned}\tag{3.20}$$

where  $\Phi$  is the temporal phase and  $\omega_0$  is the carrier frequency. The situation is illustrated in Fig. 3.19. In analogy to Raman lines, frequencies lower (higher) than  $\omega_0$  are called Stokes-shifted (anti-Stokes-shifted). As evident from Eq. (3.20), the maximum frequency shifts are governed by the steepest increase and decrease of the intensity along the pulse. As a consequence of SPM, the anti-Stokes frequencies of the SC lag temporally behind the Stokes frequencies.

The frequency-broadening effect of SPM is enhanced by the so-called self-steepening of the pulse [90], which leads to much larger gradients or even the formation of a shock front with corresponding larger intensity gradients. The asymmetric broadening of the pulse that is much broader on the anti-Stokes side in many cases, can be explained by the non-SPM effects [91].

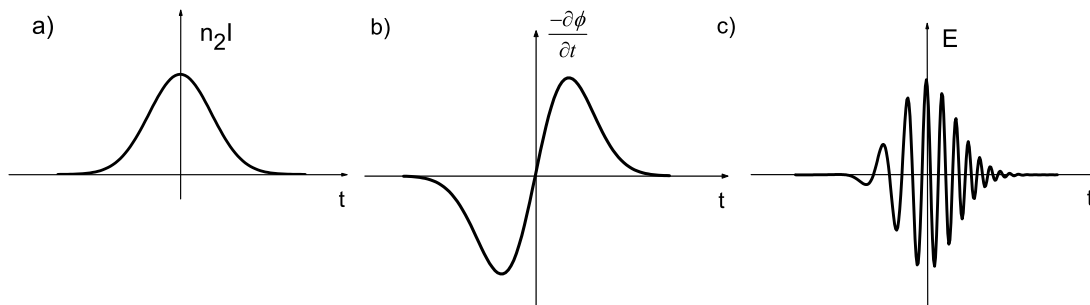


Figure 3.19: Mechanism for SPM of a Gaussian laser pulse: a) time-dependent non-linear refractive index, b) time rate of frequency shift, c) time-dependent electrical field.

### 3.1.4.5 Band gap dependence and conical emission

The spectral width of the SC depends strongly on the medium in which it is generated. Brodeur *et al.* [92] found that a band gap threshold exists for continuum generation, above which the spectral width increases with increasing band gap. The results indicate that in condensed bulk media free electron formation by multiphoton ionization is important in limiting of self-focusing and has a profound effect on SCG. They could explain the surprisingly low beam divergence of supercontinua that were generated just above the power threshold.

Another characteristic of the SC is the angular distribution of frequencies or conical emission which is responsible for the blue rim observed for visible light supercontinua. Several explanations have been involved, but so far no unifying picture has emerged. Most popular are four-wave mixing [82] and the interpretation in terms of Cerenkov-radiation [93].

### 3.1.5 Pump-probe detection scheme

Electronic devices cannot measure transient signals on the femtosecond time scale. Therefore, ultrafast spectroscopy experiments are conducted using the pump-probe detection scheme (or equivalent variants). The principle is shown in Fig. 3.20. First, an ultrafast pump pulse excites the system under investigation coherently. This sets the temporal starting point  $t_0$  of the experiment. The state of the system at time  $t$  is then monitored by a delayed second probe pulse (that is usually much weaker), where the delay is introduced *via* a variable change in the optical path length of the probe pulse.

The temporal resolution of the experiment is limited by the duration of the pulses and does



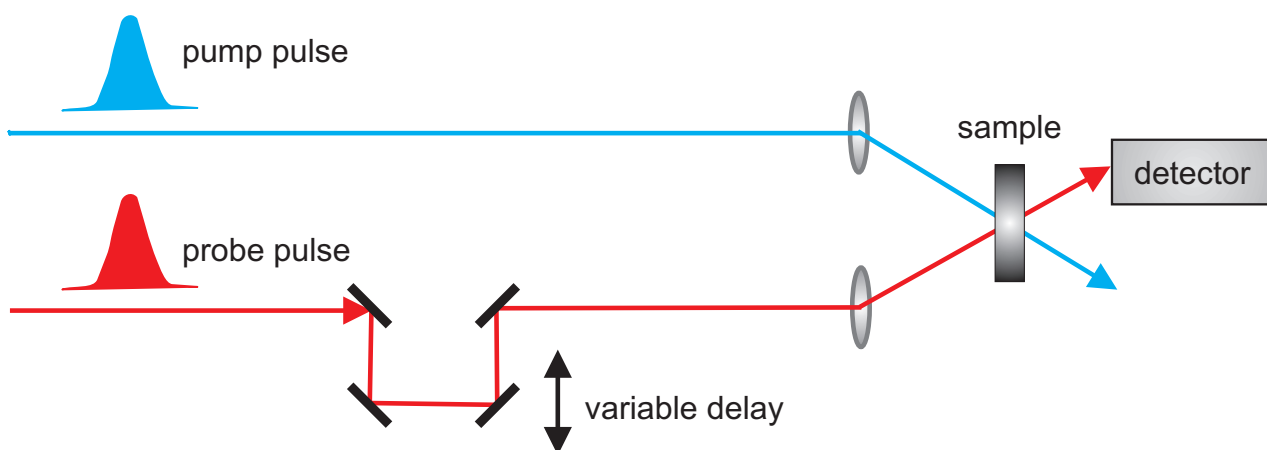


Figure 3.20: *Schematic view of the pump-probe principle.*

not depend on the electronic response time of the detector. It is described by the instrument response function, which is usually approximated by the intensity cross-correlation function CCF of the pump and probe pulses

$$CCF(t) = \int I_{pump}(t)I_{probe}(t - \tau)d\tau. \quad (3.21)$$

The complete temporal evolution can be obtained by varying the probe's delay over the desired range and by recording the system response to the probe pulse at each time step.

Many different schemes have been realized experimentally, but time-resolved mass-spectrometry [94, 95], time-gated fluorescence detection by up-conversion [24, 96] and transient absorption [4, 97] (TA) are the most popular. The latter is used in this work.

In a typical TA experiment, a broadband SC probe pulse is focused into the excited sample volume and the change in optical density is recorded by spectrally resolved detection of the transmitted probe light in a spectrometer. The changes in optical density are related to population changes in the ground and excited states *via* Beer's law. Figure 3.21 shows possible contributions to the TA signal. The pump pulse excites the molecules from the ground state  $S_0$  to a higher electronic state  $S_1$ . The depopulation of the ground state due to the excitation with the probe pulse gives rise to a change in optical density called ground state bleaching (Fig. 3.21 a)). Transitions of the excited molecules to higher states induced by the probe pulse are the so-called excited state absorption (Fig. 3.21 b)), and the shifted absorption of molecules that have relaxed to the vibrationally hot levels of the ground state is called hot ground state absorption (Fig. 3.21 c)). Further contributions that lead to a change in optical density are fluorescence and stimulated emission (Fig. 3.21 d)). TA is thus able to provide very comprehensive information about the ultrafast dynamics of the selected systems provided

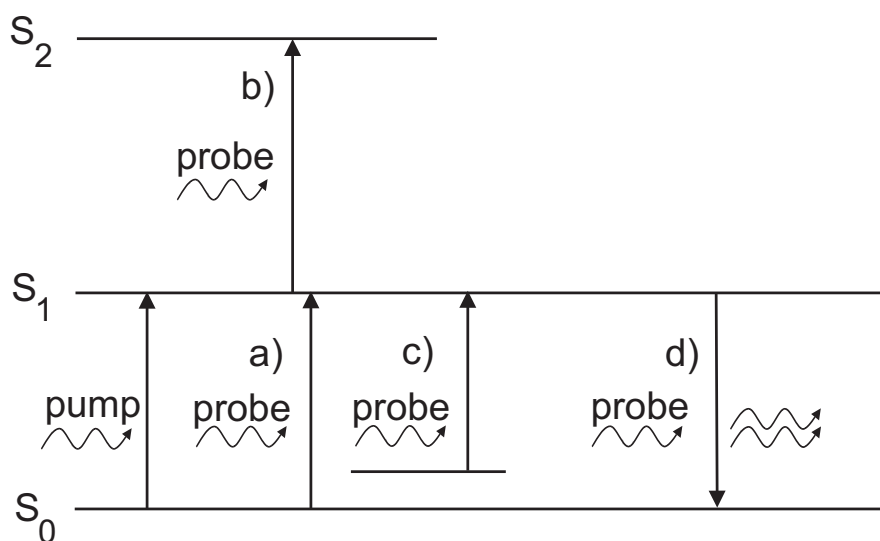


Figure 3.21: *Schematic sketch of processes that can contribute to the TA signal: a) ground state bleaching; b) excited state absorption; c) hot ground state absorption; d) stimulated emission.*

that the single contributions are disentangled from the experimental data. Details of the TA experiment and data acquisition procedures of this work will be given in Sec. 3.2.

## 3.2 Experimental setup

The first goal of this work was to set up a new experiment for the broadband detection of absorbance changes occurring during photo-induced ultrafast molecular processes. As described in the previous subsection, probing transient absorption allows to gain information about the dynamics in the excited state as well as the cooling dynamics in the ground state. However, the associated absorbance changes are quite often very small, sometimes less than one part per thousand ( $10^{-3}$ ). Achieving a sufficient sensitivity and reproducibility poses a major challenge and can only be obtained by using a probe-reference setup and appropriate data acquisition routines. The second issue concerns the spectral range of the broadband detection, which depends critically on the precise conditions of the supercontinuum generation and requires experimental care. Finally, the temporal resolution of the apparatus must not be compromised, since much of the interesting dynamics occurs within the first picosecond after photoexcitation. This section describes the experimental setup and the procedures and data handling that were chosen to achieve these goals.

The different parts of the experimental setup are shown in the schematic sketch of Fig. 3.22. In the following subsections, details on the Ti:Sa laser, the pump pulse generation, the probe pulse generation, the pump-probe setup, and the detection of the data are given.

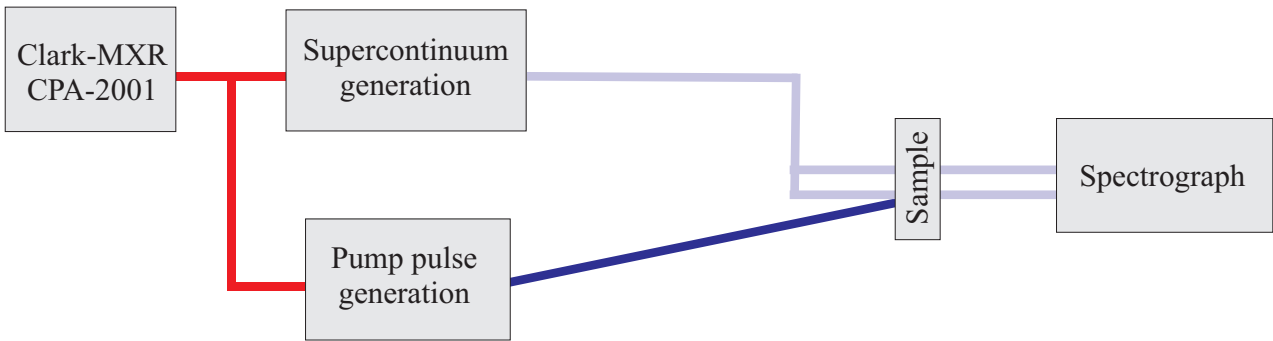


Figure 3.22: Schematic setup of the transient absorption experiment.

### 3.2.1 Description of the Ti:Sa laser

The CPA-2001 is a regeneratively amplified system with fs-seed pulses from an  $\text{Er}^{3+}$ -doped fiber laser (SErF). The complete laser system is built on two levels:

- bottom level:
  - diode laser
  - SErF (Erbium doped fiber) fiber oscillator
  - pulse stretcher
- top level:
  - frequency-doubled Nd:YAG pump laser
  - regenerative amplifier
  - pulse compressor

The SErF oscillator is pumped by a diode laser at a wavelength of  $\lambda = 980$  nm with a power of 166 mW. It has a ring configuration that contains optics for polarization control, output coupling and wavelength control. A schematic view of the SErF oscillator is shown in Fig. 3.23. The continuous wave pump light is coupled into the oscillator *via* a Y-branch. Only a part of the fiber is  $\text{Er}^{3+}$  doped and serves as active laser medium, the rest of the fiber is undoped and acts as an additional Kerr medium. The polarization optics and insulator provide so-called polarization rotation mode-locking [98] (for a more detailed account, see also [99]). The output pulses of the fiber oscillator are at a wavelength of  $\lambda \approx 1550$  nm with a repetition rate of 35 MHz and 100 fs pulse duration. For use as seed pulses, the output of the fiber oscillator is frequency doubled to  $\lambda \approx 775$  nm with a periodically-poled  $\text{LiNbO}_3$  crystal, with an energy of 100 pJ.

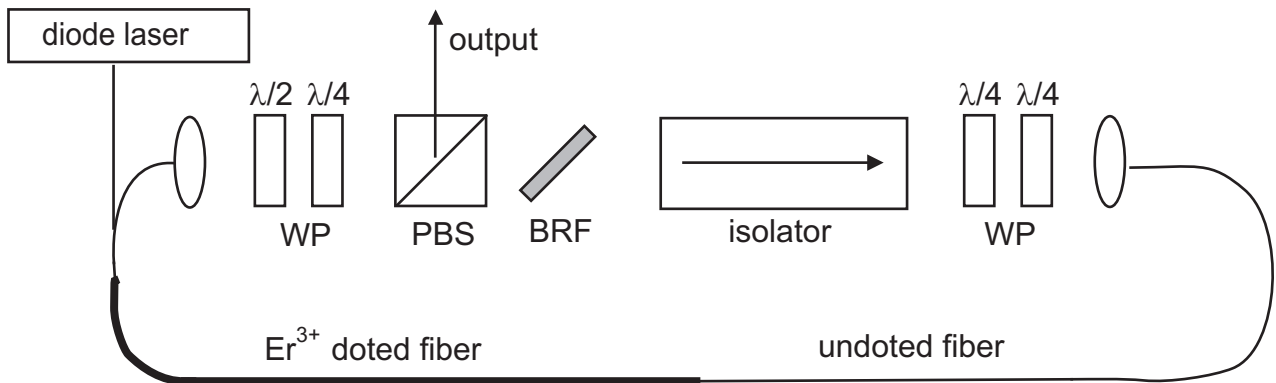


Figure 3.23: Schematic view of the SErF oscillator: WP = waveplates, PBS = polarization beam splitter, BRF = birefringent filter.

The amplification of the weak 775 nm seed pulse is performed *via* CPA. First the 100 fs-seed pulse is stretched to 20 ps by means of a grating pair stretcher [100, 101] and then enters the RGA cavity situated on the top level (a photo of the top level is given in Fig. 3.24).

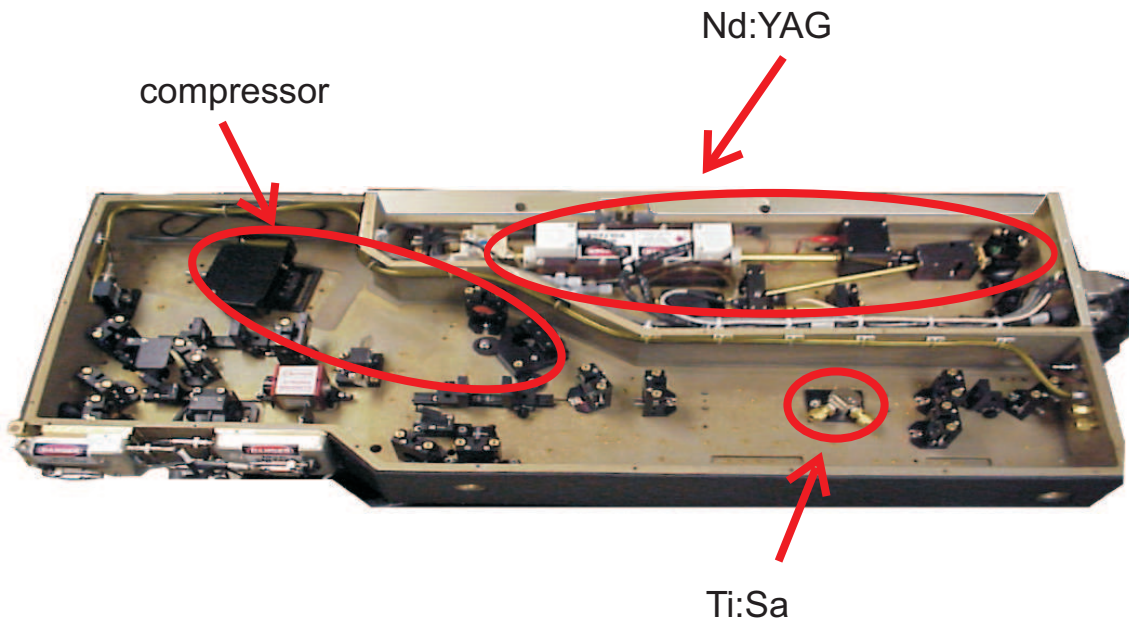


Figure 3.24: Photograph of the top level of the CPA-2001 laser system.

The Ti:Sa RGA laser medium is pumped by the output of a Q-switched frequency doubled Nd:YAG laser which in turn is pumped by a flash lamp. The Q-switch is triggered at about 1 kHz by a master signal that is derived from the output of a SErF oscillator monitor photodiode to ensure correct timing. The injection of the seed pulse into the Ti:Sa crystal and the ejection of the amplified seed beam afterwards is controlled by a Pockels cell, which acts as an extremely fast electro-optical light switch. The injection is always correlated with

the population inversion induced by the Nd:YAG laser. The Pockels cell is also triggered with respect to the master trigger by means of the driver unit DT-505, which includes two important delays. The first delay is used to inject the pulse into the amplification cavity. The second delay starts ejections of the amplified pulse after a number of round trips in the cavity. The intensity increase of the seed pulse can be seen in Fig. 3.25 (the so-called “regen-trace”). The pulse energy reaches saturation after four round-trips, and the pulse is coupled out afterwards. Before exiting the laser system the horizontally polarized amplified seed pulses

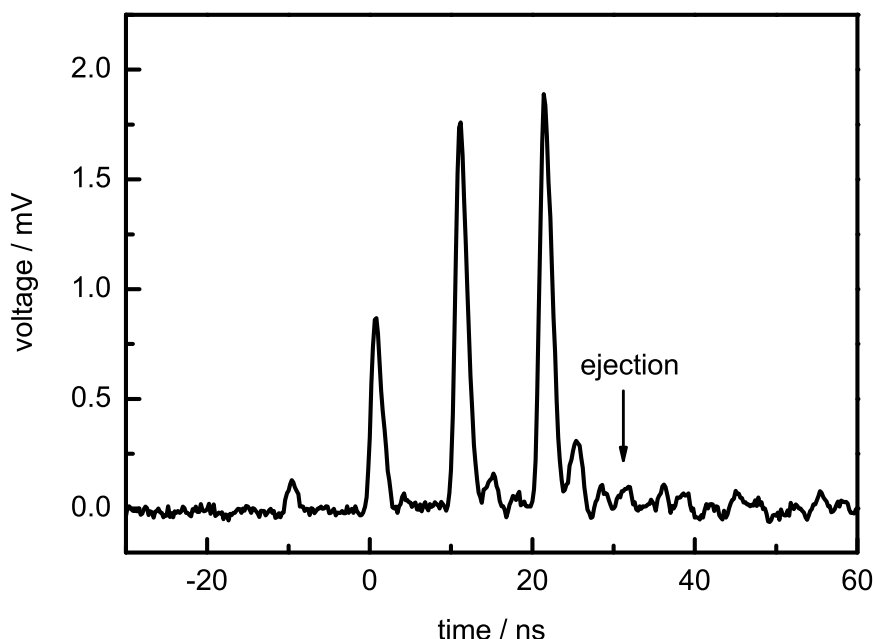


Figure 3.25: *The so-called regen-trace from the regenerative amplifier. The four peaks represent the gradual amplification of the seed pulse in the cavity. Only after saturation, that corresponds to the fourth peak, the pulse is coupled out from the cavity.*

must be compressed. More details of the RGA process can be found in [99].

The characteristic parameters of the fundamental laser pulses generated with the Clark-MXR CPA-2001 laser system are summarized in Table 3.2.1.

Table 3.1: Operating parameters of the Clark-MXR CPA-2001 laser system.

Pulse energy	0.8 mJ
Pulse duration (FWHM)	210 fs
Wavelength	775 nm
Transverse mode	TEM <sub>00</sub>
Repetition rate	approximative 1 kHz
Polarization	linear, horizontal
Energy stability	< 1% rms

### 3.2.2 Pump pulse generation

For use as pump pulses, the fundamental pulses of the Clark-MXR CPA-2001 laser system described in Sec. 3.2.1 ( $\lambda = 775$  nm, FWHM = 210 fs, pulse energy 200  $\mu$ J) are wavelength-converted using either SHG or a NOPA. The SHG is performed using type I phase matching in a BBO crystal with a thickness of 0.5 mm cut at  $\theta = 29.8^\circ$ . The resulting pump pulse is centered at 387 nm. Tunable pump pulses are generated with the NOPA setup shown in Fig. 3.26 [70]. By reflection at the surface of a quartz wedge a small part ( $\approx 1 - 2$   $\mu$ J) is split off the fundamental beam. For SCG it is focused with a lens ( $f = 50$  mm) into a sapphire plate with a thickness of 2.3 mm. The energy of the incident light can be controlled by a variable aperture mounted in the beam path. For optimum stability and spectral shape of the SC, the focus position can be adjusted by moving the sapphire plate with a translation stage. The SC is collimated with an achromatic lens ( $f = 30$  mm), which is also mounted on a translation stage for a variation of the effective focal length of the lens system. The beam diameter of the remaining 98 % of the fundamental beam is reduced with a telescope system consisting of two lenses ( $f = 250$  mm and  $f = -200$  mm). The beam is then frequency-doubled in BBO (see above) to provide pump pulses (387 nm, 60  $\mu$ J) for the NOPA. The pump beam is focused into the NOPA crystal (BBO, cut angle  $\theta = 32^\circ$ ,  $d = 0.5$  mm) with a spherical mirror ( $f = 350$  mm). The SC acts as the NOPA seed pulse and can be delayed with respect to the pump pulse by means of a translation stage. The pump and seed beams intersect at an angle of  $3.7^\circ$  inside the NOPA crystal for simultaneous phase and group velocity matching. The resulting NOPA pulses have energies between 6 and 20  $\mu$ J and can be tuned within the white light range of 450 - 700 nm by varying the pump delay relative to the seed. The pulses are compressed with a prism compressor to typical pulse durations of 40 - 80 fs. For use as excitation source, the energy of the NOPA pulses is typically reduced to 0.2 - 0.5  $\mu$ J by a variable aperture.

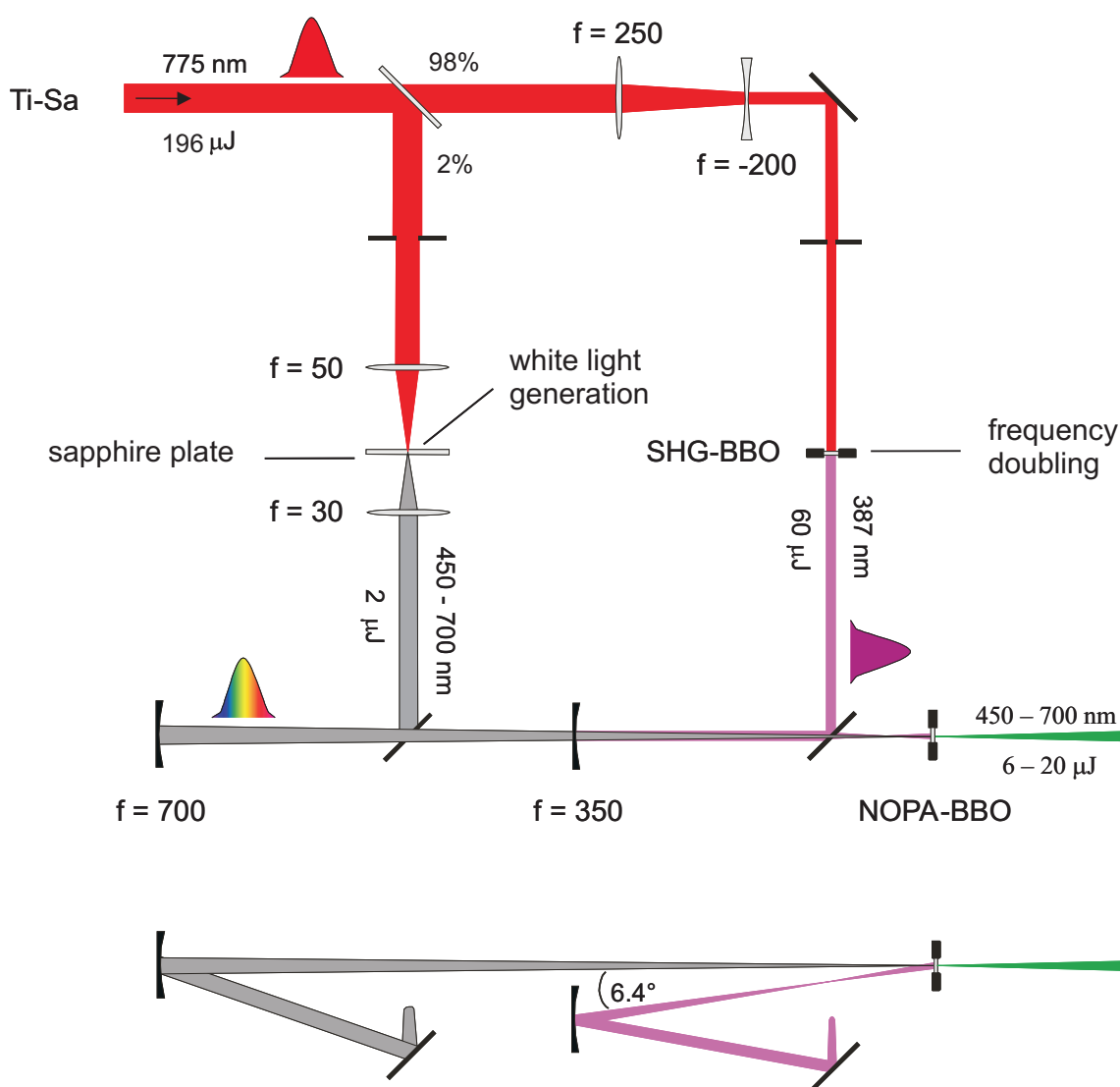


Figure 3.26: Schematical view of the non-collinear optical parametric amplification.

### 3.2.3 Probe pulse generation

Supercontinuum generated for broadband detection is carried out in the setup sketched in Fig. 3.27. The white light is generated in sapphire or  $\text{CaF}_2$ . As before, the SC pump beam with an energy of  $\approx 1 \mu\text{J}$  is generated by reflection off a quartz wedge surface. For SCG in  $\text{CaF}_2$ , higher intensities between 2 - 3  $\mu\text{J}$  are required. This amount of energy is obtained by changing the angle of incidence onto the wedge from  $45^\circ$  (as for sapphire) to approximately  $23^\circ$ . Fine tuning of the SC pump beam intensity can be achieved by a variable aperture. Because of the lower damage threshold of  $\text{CaF}_2$ , subsequent pulses have to hit different spots on the plate to prevent material degradation. Therefore, the  $\text{CaF}_2$  is mounted in a home-built rotation stage. A photograph is shown in Fig. 3.28. Smooth motion with low wobble is achieved by using a

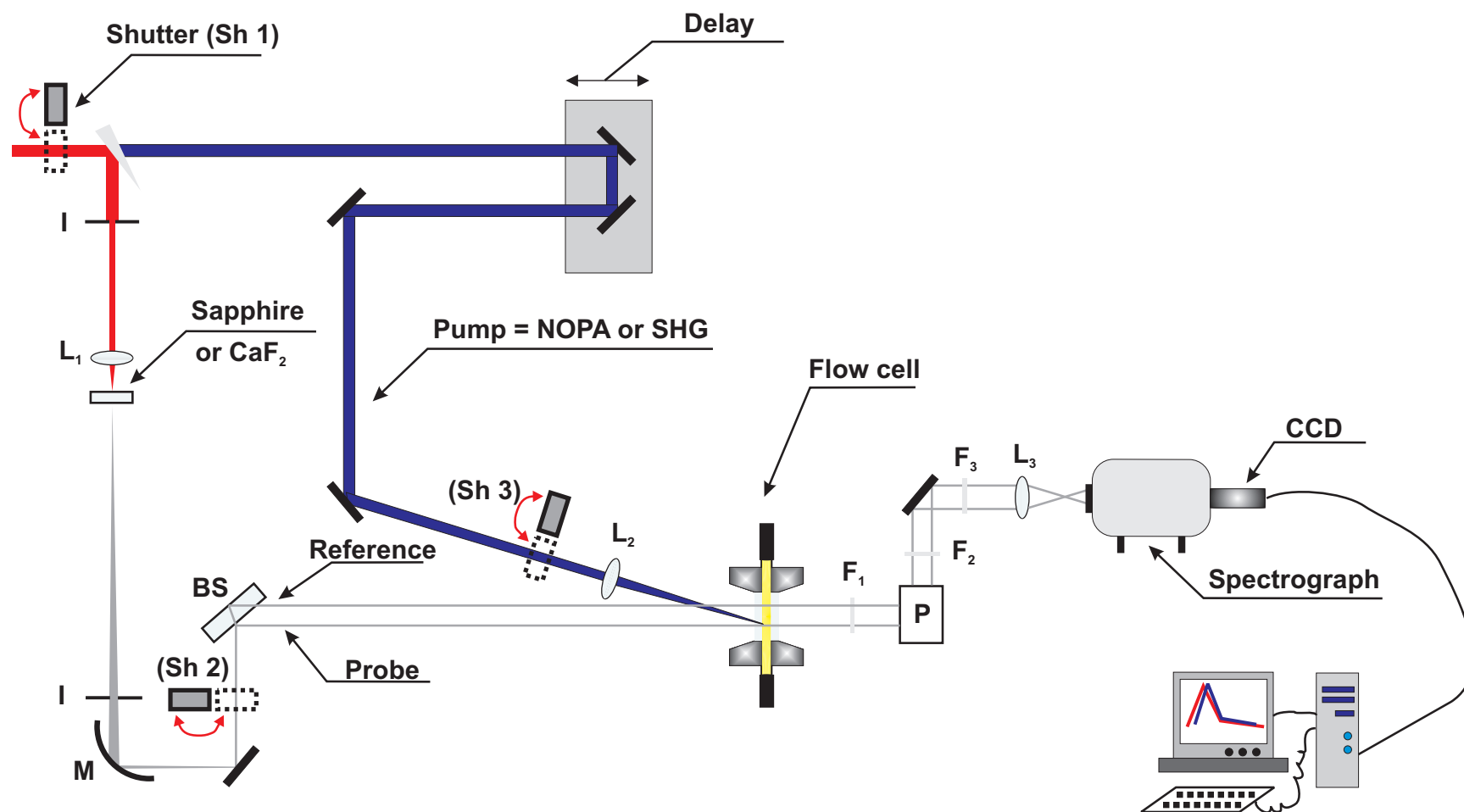


Figure 3.27: Setup of the transient absorption experiment.  $I$  = variable diaphragm,  $M$  = off-axis parabolic mirror,  $BS$  = 5 mm fused silica plate,  $L_1$ :  $f = 50$  mm for sapphire,  $f = 100$  mm for CaF<sub>2</sub>,  $L_2$ :  $f = 200$  mm,  $L_3$ :  $f = 100$  mm,  $F_1$ ,  $F_2$  and  $F_3$  = filters,  $Sh 1$ ,  $Sh 2$  and  $Sh 3$  = shutters.



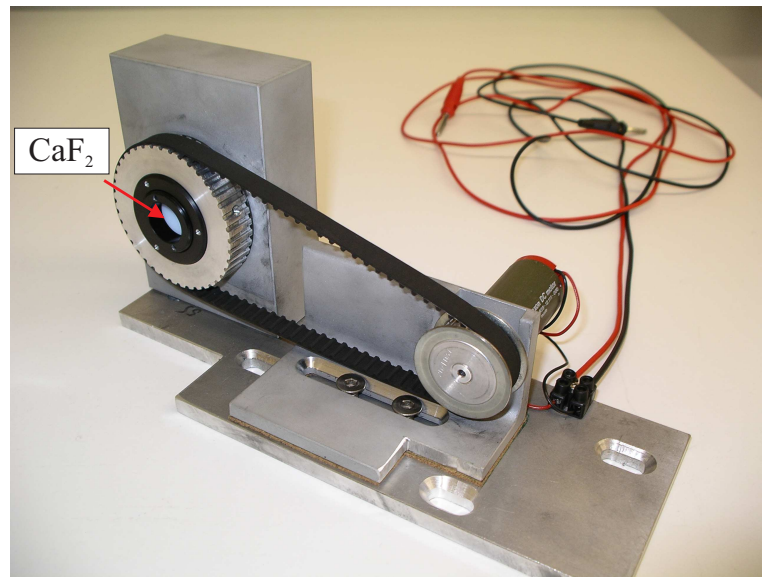


Figure 3.28: *Device for rotation of the calcium fluoride plate.*

double ball bearing. Typically, rotation frequencies higher than 50 Hz were used.

The position of the focus inside the optical material has a large influence on the resulting chirp, the spectral width and the pulse-to-pulse stability of the SC. Optimum SCG occurs for a focus position roughly half way inside. The position is adjusted by moving the focusing lens ( $f = 50$  mm for sapphire,  $f = 100$  mm for  $\text{CaF}_2$ ) which is mounted on a translation stage. The focus position can be checked by visual inspection, which is also used to verify that no multifilament SCG is present. Observation of a projection of the SC onto a screen provides a practical criterion for its quality (see Fig. 3.29). The projection should be spectrally

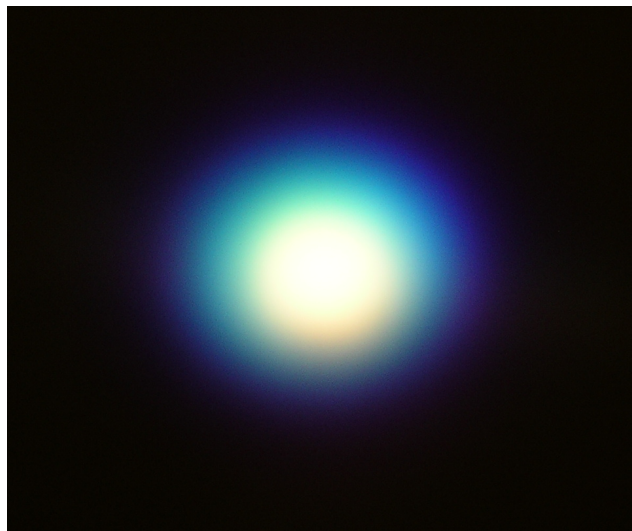


Figure 3.29: *Photograph of a white light spot generated in sapphire.*

homogenous with a slight blue or purple rim for SC in sapphire and  $\text{CaF}_2$ , respectively.

As shown in Fig. 3.30 a), the fluctuations of the resulting SC translate into base line

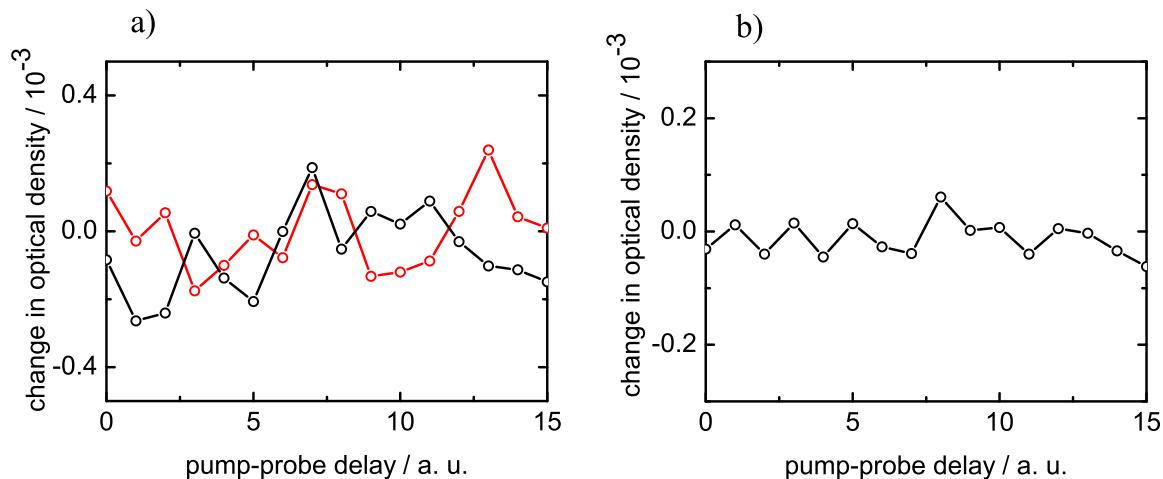


Figure 3.30: *a) Typical stability of white light generated in sapphire (black line) and calcium fluoride (red line) when 7500 laser shots are averaged. b) Stability of white light generated in sapphire when 4800 laser shots are averaged, under perfectly optimized conditions.*

fluctuations of the absorbance changes of about  $10^{-4}$  when the typical data acquisition times are used (or even lower as presented in Fig. 3.30 b)).

Figure 3.31 shows the typical spectra of the SC probe light generated in sapphire and  $\text{CaF}_2$ . The spectra are clipped at 700 nm by a cut-off filter (Edmund Optics) in the beam path to prevent damage of the CCD-detector and data overflow. For optimum spatial characteristics of the SC, the central part of the beam is cut out using a variable aperture. The collimation of the SC is performed using either an achromatic lens ( $f = 30$  mm) or an off-axis parabolic mirror (Melles Griot,  $f = 59.7$  mm), which are placed on a translation stage for adjustment of the effective focal length. Although adjustment of the achromatic lens proved much easier, the additional optical material in the beam path ( $\approx 11$  mm quartz glass) leads to a large increase of the SC chirp and was not used in later experiments.

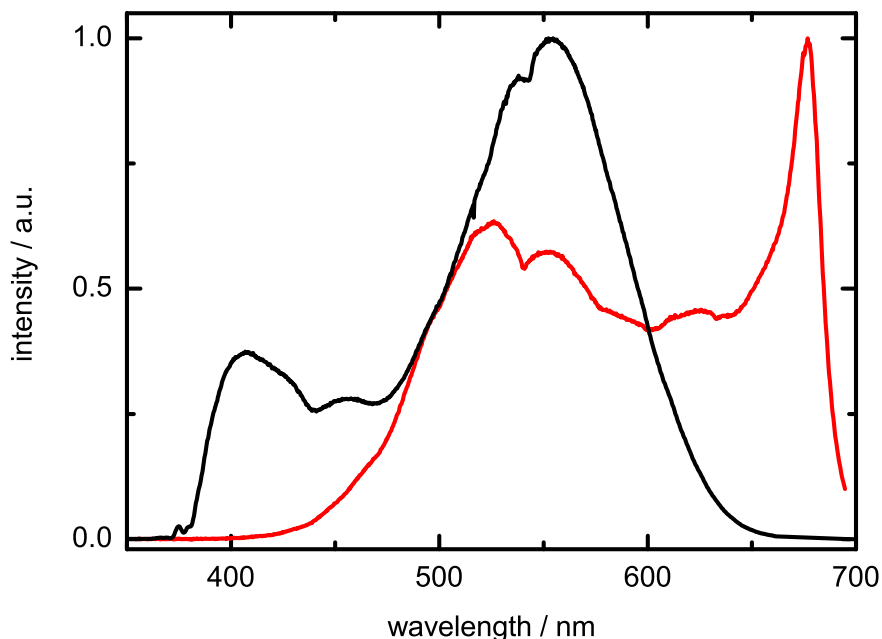


Figure 3.31: Normalized white light spectra generated in sapphire (red line) and calcium fluoride (black line). For the  $\text{CaF}_2$  supercontinuum an additional BG 18 filter reduces the intensity above 600 nm.

### 3.2.4 fs-pump-probe-setup

The transient absorption experiments were performed with a setup sketched schematically in Fig. 3.27.

To achieve a sufficient sensitivity for the detection of the absorbance changes, it is necessary to minimize the effects of the shot-to-shot fluctuations of the SC. This is done by generating a probe and a reference beam from the reflections of the SC at the front and back surface of a 5 mm plane-parallel fused silica plate (Laseroptik), respectively. The probe-reference beams and the pump beam impinge on the sample at a non-collinear angle of approximately  $5^\circ$ . The pump beam is focused with a  $f = 200$  mm lens to a diameter of  $\approx 200$   $\mu\text{m}$  inside the sample. There it is overlapped with the probe beam which has a smaller diameter (typically 100 - 160  $\mu\text{m}$ ). The reference beam passes through a different sample volume and must not overlap with the pump beam in the cell. The pump pulse is delayed with respect to the probe pulse with an optical delay line consisting of a retro-reflector (Melles Griot) and a computer-controlled translation stage (Physik Instrumente, M-126.CG) with a resolution of 0.1  $\mu\text{m}$  (equalling 0.33 fs). The maximum possible delay variation is 166 ps.

The sample cell is essentially a channel in a teflon disk enclosed between two sapphire windows. A photograph of the home-made cell is displayed in Fig. 3.32 a), Fig. 3.32 b) shows a cross section of the design. The sapphire windows have a thickness of 0.2 mm and

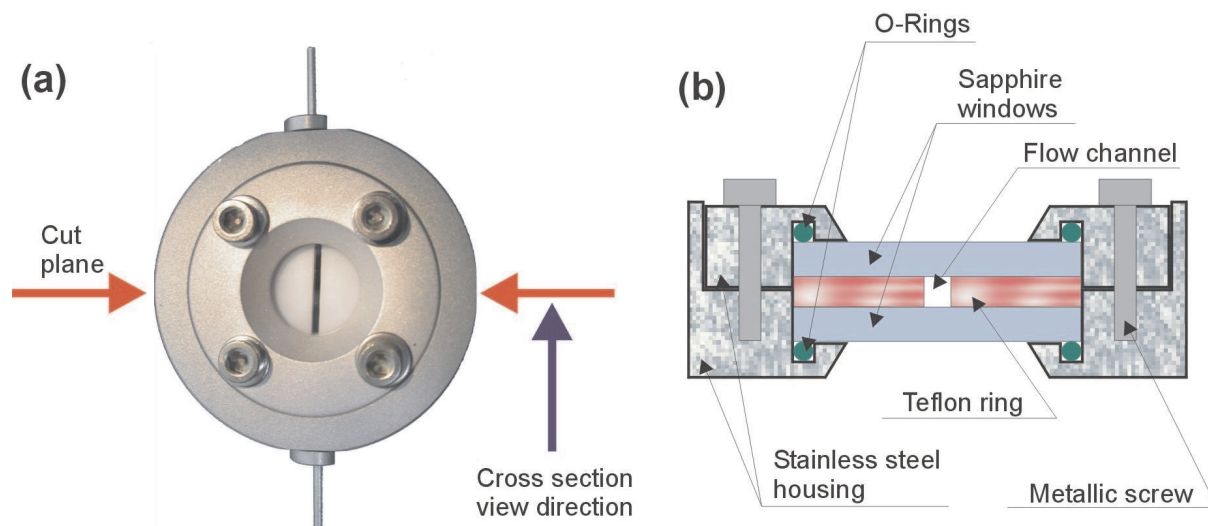


Figure 3.32: a) Photograph of the sample cell. b) Cross section of the sample cell.

the optical path length of the cell is 1 mm. The miniaturized design allows for a complete exchange of the sample solution in the probe volume between two subsequent laser shots, *i.e.* within 1 ms. The solution is pumped through the cell by a peristaltic pump (Ismatec, Reglo Analog MS-2/6) with a typical flow rate of 10 - 12 ml/min.

After the sample, the probe and reference beam pass a periscope for rotation of their propagation plane from horizontal to vertical and are focused with an achromatic lens ( $f = 100$  mm) onto the entrance slit of an imaging spectrograph (L.O.T.-Oriol GmbH, MS261i). At the exit slit of the spectrograph, the spectra are imaged onto a  $1024 \times 127$  pixel array of a CCD camera (L.O.T.-Oriol GmbH, B401-UV) which provides simultaneous detection of both spectra. The data acquisition is described in the next section.

### 3.3 Data acquisition

The readout of the CCD-array as well as the translation stage, the various shutters *etc.* are controlled by a LabView program on a PC [102]. To obtain the probe and reference spectra, vertical binning is performed for the respective tracks. Figure 3.33 illustrates the procedure. Binning is along the direction indicated by the arrows. Both spectra are then read as a line of 1 D data. Since the binning process takes roughly 4 ms, the probe and reference

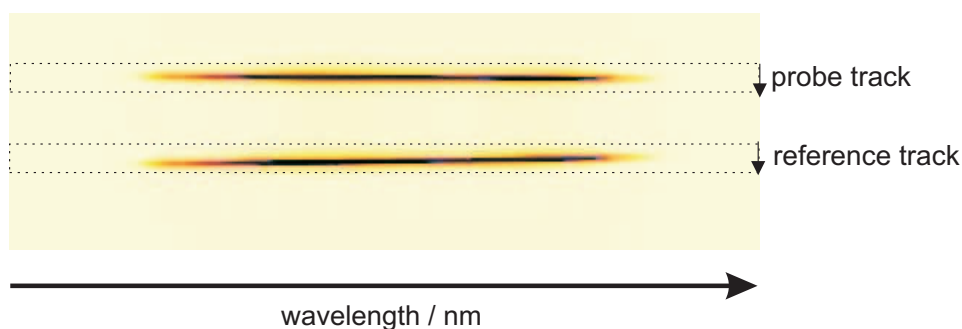


Figure 3.33: Image of the dispersed probe and reference tracks on the CCD detector.

beams have to be blocked during readout. This is done with a mechanical shutter (Electro-Optical Products Corp.) (Sh 1 in Fig. 3.27). Each of the recorded spectra is accumulated on the CCD for typically between 100 and 300 laser shots (*i.e.* 0.1 - 0.3 s) before readout. Calibration of the spectrometer is performed with the light of a mercury pen-ray lamp (L.O.T. Oriol GmbH). Figure 3.34 shows the pen-ray spectrum which allows wavelength calibration over the wavelength range from 300 - 600 nm. Alternatively, calibration can be performed by

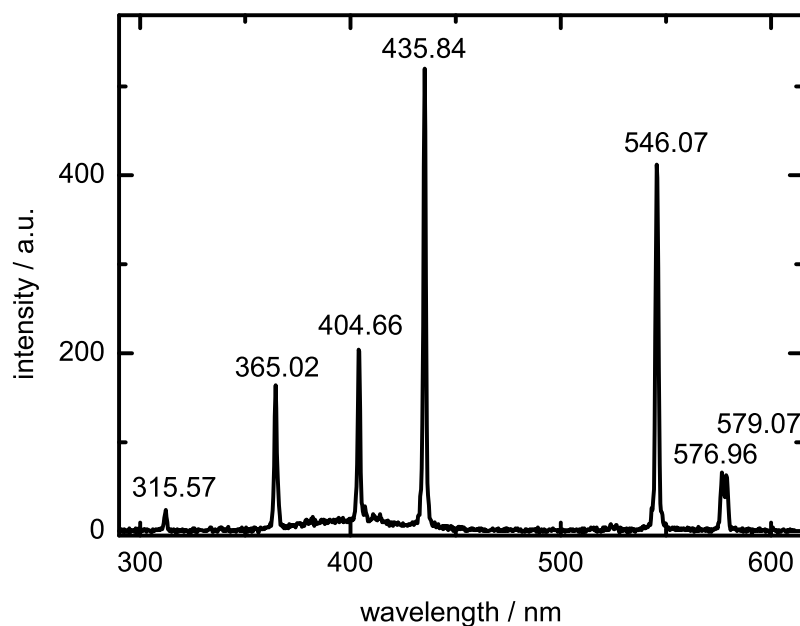


Figure 3.34: Spectral lines of the pen-ray lamp used for wavelength calibration.

putting different interference filters into the SC beam path. Figure 3.35 shows that the relation between pixel position and wavelength is almost perfectly linear in the entire wavelength range

(interference filters centered at  $\lambda = 486, 503.8$  and  $645$  nm were used).

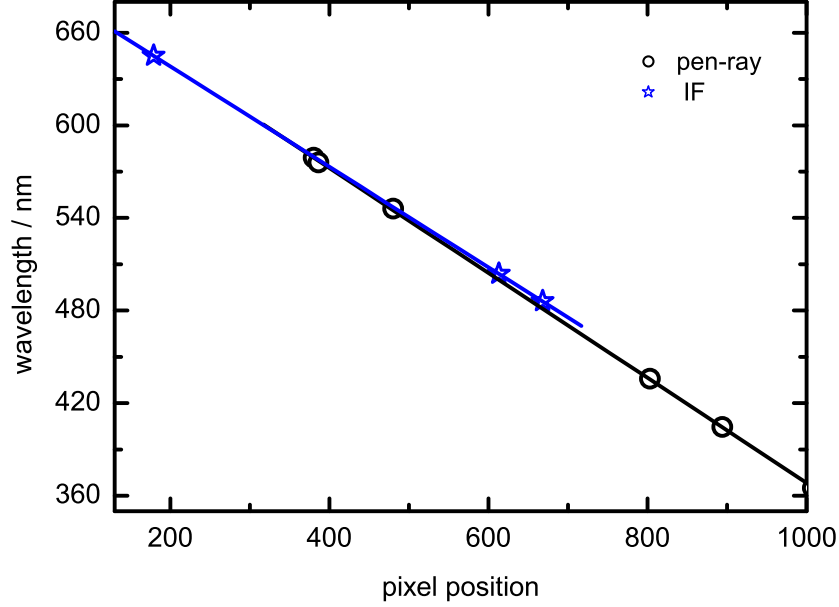


Figure 3.35: *Wavelength calibration using the pen-ray lamp and interference filters.*

The ratio of the probe and reference spectra recorded at the delay time  $t$ ,  $I^{pr}(\lambda, t)$  and  $I^{ref}(\lambda, t)$ , is proportional to the transient transmittance  $T(\lambda, \tau)$ ,

$$\frac{I^{pr}(\lambda, t)}{I^{ref}(\lambda, t)} = c \cdot T(\lambda, t), \quad (3.22)$$

where the factor  $c$  takes care of experimental parameters such as the beam splitter characteristics, position-dependent detector sensitivity and so on. To accommodate for possible drifts in the SC over time, for each delay the transient transmittance with blocked pump beam,  $T_0(\lambda, t)^2$ , is also recorded. The relative transmission

$$T_r(\lambda, t) = \frac{T(\lambda, t)}{T_0(\lambda, t)} \quad (3.23)$$

---

<sup>2</sup> $T_0(\lambda, t)$  is not explicitly delay-dependent since the pump is blocked. However, if there is a spectral drift of the SC during a full experiment, it becomes implicitly dependent on  $t$ .

is related to the change in optical density (or the transient absorbance) *via*

$$A(\lambda, t) = -\log T_r(\lambda, t) = -\log \left( \frac{T(\lambda, t)}{T_0(\lambda, t)} \right). \quad (3.24)$$

When the intensities of the ambient background, fluorescence light and scattered light from the pump beam are also taken into account, the transient absorbance has to be calculated from

$$A(\lambda, t) = -\log \left( \frac{I_0^{ref}(\lambda, t) - I_b^{ref}(\lambda, t)}{I_0^{pr}(\lambda, t) - I_b^{pr}(\lambda, t)} \cdot \frac{I_f^{pr}(\lambda, t) - I_f^{ref}(\lambda, t)}{I_f^{ref}(\lambda, t) - I_f^{pr}(\lambda, t)} \right), \quad (3.25)$$

where  $I_b^{pr}(\lambda, t)$  and  $I_b^{ref}(\lambda, t)$  are the background probe and reference spectra (no pump, no probe and reference beam) and  $I_f^{pr}(\lambda, t)$  and  $I_f^{ref}(\lambda, t)$  are the spectra recorded with blocked probe and reference beams. To increase the sensitivity of the experiment, usually 5000 - 10000 laser shots at each delay are accumulated in the computer memory for the calculation of  $A(\lambda, t)$ .

### 3.3.1 Data fitting procedure

The transient absorption data values at the wavelength  $\lambda_i$  ( $i = 1, \dots, N_\lambda$ ) and at the delay time  $t_j$  ( $j = 1, \dots, N_t$ ) make up a two dimensional data matrix  $A_{ij} = A(\lambda_i, t_j)$ . The aim of the data analysis is to disentangle the contributions that arise from the different species and processes and to determine the species associated spectra and their kinetics. In the absence of prior knowledge, *e.g.* about a particular kinetic model, the common practice is to describe the transient absorption profiles at a single wavelength with a sufficient number of exponential decays,

$$A_\lambda(t) = \sum_i a_i \exp[-(t - t_{0i})/\tau_i], \quad (3.26)$$

where the  $\tau_i$  are the decay times, the  $a_i$  are the amplitudes and the  $t_{0i}$  are the wavelength-dependent time zero offsets due to the SC chirp.

Equation (3.26) does not take into account the limited temporal resolution of the experiment, which is described by the so-called instrument response function (IRF). Mathematically, this is described by a convolution of the “ideal” time profile with the IRF. If the IRF is a Gaussian, this gives

$$A_\lambda(t) = \frac{1}{2} \sum_i a_i \exp \left( \frac{1}{2} \frac{\sigma_{IRF}^2}{\tau_i^2} - \frac{t - t_{0i}}{\tau_i} \right) \left( 1 - \operatorname{erf} \left\{ \left[ \frac{\sigma_{IRF}^2}{\tau_i} - (t - t_{0i}) \right] \frac{1}{\sqrt{2}\sigma_{IRF}} \right\} \right). \quad (3.27)$$

Although the IRF width parameter  $\sigma_{IRF}$  can in principle be treated as a free fitting parameter,

this can give erroneous results if the fastest decay time and  $\sigma_{IRF}$  have similar values. It is therefore important to have at least an estimate for the correct value, which can be obtained from the cross-correlation of the pump and probe pulses. The detailed procedure is described in the next chapter. The next issue with Eq. (3.27) is that data without coherent contributions from the solvent and background are assumed. This can be achieved if these contributions are determined in a separate experiment and then subtracted from the measured optical density changes.



## 4 Results and Discussion

The chapter is organized as follows: In Sec. 4.1, results on XPM, time-zero correction, SRA and ISRS are presented and are used to assess the experimental setup used in this work. On the basis of these results an optimized experimental procedure is developed. Section 4.2 contains results on the ultrafast isomerization of azobenzene, which has been subject of considerable scientific interest for many years. Azobenzene is ideally suited as a test system, since literature data exist for comparison, and the TA of azobenzene is very demanding as regards the temporal resolution and sensitivity of the apparatus. In Sec. 4.3 preliminary results on the photoisomerization of *Z*-Aberchrome 540 are presented which indicate that the dynamics occur on a sub-picosecond time-scale.

### 4.1 Characterization of the fs-pump-probe transient absorption spectrometer

Several aspects have been neglected in the description of the data treatment and the fitting procedures given in the previous section. First, the supercontinuum is chirped due to the self-phase modulation in the SCG step and the group velocity dispersion which arises in the SCG material, all optical components, the sample cell windows and the sample itself. Therefore, different SC wavelengths enter the sample at different times and a so called time-zero correction procedure has to be applied. Second, there are additional contributions to the signal that are generated by the interaction of the pump and probe pulses during the temporal overlap of both pulses. These are known as “TA artifacts“ or coherent contributions. They typically have a duration comparable to the pump-probe cross-correlation and can lead to an unwanted decrease in temporal resolution. The most significant coherent contributions are from cross-phase modulation (XPM), stimulated Raman amplification (SRA) and two-photon absorption (TPA). Third, long lasting oscillatory contributions to the signal may arise from low-frequency vibration of the solvent excited by the pump pulse, the so called impulsive stimulated Raman scattering (ISRS). All of these contributions must be determined first so that they can be subtracted. As will be shown below, indispensable information that characterizes the setup,

*e.g.* with respect to the SC chirp, can be gained in this way.

The general theoretical background for non-linear spectroscopy laid down by Mukamel [97] has been used by Ernsting and co-workers in several papers [103, 104] to develop a general formalism of pump-probe transient absorption spectroscopy. Such a detailed theoretical description is however, beyond the scope of this thesis. Instead, a phenomenological approach, similar in spirit to Refs. [105, 106, 107, 108], will be taken, using only the results of the above references [103, 104].

## 4.1.1 Cross-Phase Modulation and time-zero correction

### 4.1.1.1 Background

For the remainder of this chapter the pump pulse is assumed to be a non-chirped Gaussian with an electrical field,

$$E_p(t) = a_p \exp\left(-\frac{t^2}{2\tau_p^2} + i\omega_p t\right), \quad (4.1)$$

of amplitude  $a_p$ , temporal width  $\tau_p$ , and at a center frequency of  $\omega_p$ . For the probe, a linearly chirped SC pulse of Gaussian shape is assumed:

$$E_{pr}(t) = a_{pr} \exp\left[-\frac{t^2}{2\tau_{pr}^2} + i(\Omega_{pr}t + \beta t^2)\right]. \quad (4.2)$$

The broadband supercontinuum is characterized by its center frequency  $\Omega_{pr}$ , its temporal width  $\tau_{pr}$  and the chirp rate  $\beta$ . The chirp rate determines the size of the linear chirp and has the dimension of  $\text{fs}^{-2}$ . Small values of  $\beta$  correspond to a large chirp and larger values of  $\beta$  to a smaller chirp. Although the natural variable for the experiment is wavelength, the common description of the phenomena is in frequency space, for which

$$E_{pr}(\omega_{pr}) = \tau_{pr} \sqrt{2\pi/\alpha} \exp\left[-\tau_{pr}^2(\omega_{pr} - \Omega_{pr})^2/2\alpha\right], \quad (4.3)$$

where  $\alpha = 1 - 2i\beta\tau_{pr}^2$  and  $\omega_{pr}$  is the probe pulse frequency. As a consequence of the chirp, the probe pulse has an instantaneous frequency which is time dependent. This means that in the sample, different frequency components of the SC pulse interact with the pump pulse at different delay times. This is described by the time-zero function:

$$t_0(\omega_{pr}) = (\omega_{pr} - \Omega_{pr})/2\beta. \quad (4.4)$$

Knowledge of the time zero-function allows one to time-correct the experimental data to a common zero-delay for all wavelengths.

The total delay  $t_d(\omega)$  is just the sum of the experimental delay  $t_d$  and the time-zero function  $t_0(\omega)$ ,

$$t_d(\omega_{pr}) = t_d + t_0(\omega_{pr}). \quad (4.5)$$

The coherent interaction between probe and pump pulses at zero delay leads to the so-called cross-phase modulation (XPM) that contributes to the TA signal. The physical origin of the XPM is the modification of the refractive index by the pump pulse *via* the optical Kerr effect (see Eq. (3.16)), which is experienced by the SC probe during the temporal overlap with the pump pulse and originates in the cell windows and in the solvent. Figure 4.1 shows the XPM calculated for different probe wavelengths *via* [103]

$$\begin{aligned} \Delta D(\omega_{pr}, t_d) \approx & D_o^e \exp \left[ -\frac{[t_d + t_0(\omega_{pr})]^2}{\tau_p^2} \right] \\ & \times \sin \left[ \frac{1}{2\beta\tau_p^2} - \frac{[t_d + t_0(\omega_{pr})]^2}{\beta\tau_p^4} - \frac{t_0(\omega_{pr})[t_d + t_0(\omega_{pr})]}{\beta\tau_{pr}^2\tau_p^2} \right], \end{aligned} \quad (4.6)$$

using a pump pulse centered at  $\omega_p = 3.943 \text{ fs}^{-1}$ , a temporal width of the pump pulse  $\tau_p = 50 \text{ fs}$ , and a probe pulse centered at  $\Omega_{pr} = 3.754 \text{ fs}^{-1}$  with a temporal width  $\tau_{pr} = 250 \text{ fs}$  and a chirp rate  $\beta = 3.9 \times 10^{-4} \text{ fs}^{-2}$ . The blue line represents the cross-correlation function

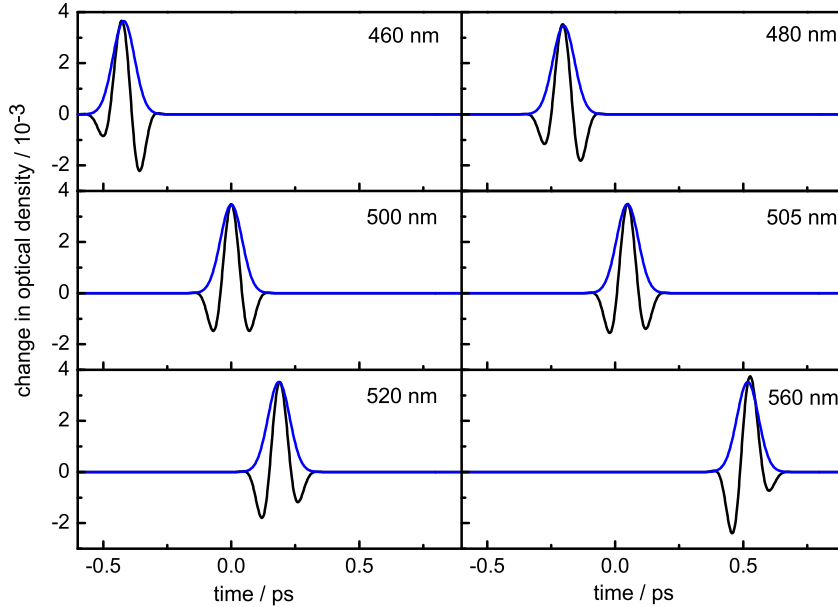


Figure 4.1: *Simulated XPM signals for a linearly chirped probe pulse. The following parameters are used:  $\omega_p = 3.943 \text{ fs}^{-1}$ ,  $\tau_p = 50 \text{ fs}$ ,  $\Omega_{pr} = 3.754 \text{ fs}^{-1}$ ,  $\tau_{pr} = 250 \text{ fs}$ ,  $\beta = 3.9 \times 10^{-4} \text{ fs}^{-2}$ .*

between pump and probe pulses. Several points are worth noting: First, the time-zero function (Eq. (4.4)) causes the maximum of the XPM  $t_0$  shift in time with wavelength. Second, the maxima of the XPM and the cross-correlation function almost coincide, and the XPM and the cross-correlation are of comparable width. In the case of a fast chirp rate,  $2\beta\tau_{pr}^2 \gg 1$ , the cross correlation width  $\tau_{cc}$  is equal to the pump pulse duration. Third, the XPM is “w” shaped for a positive chirp (this is reversed for a negative chirp), and the temporal integral at each wavelength is equal to zero, since no absorption takes place. For the simulation, the amplitude of the XPM, which increases with increasing chirp and decreasing wavelength,  $D_0^e$  of Eq. (4.6) was set constant. The final point regards the pump intensity dependence of the XPM. Since the Kerr effect depends on intensity, it is obvious that the XPM amplitude is also proportional to the pump intensity.

#### 4.1.1.2 Results

Cross-phase modulation (XPM) measurements were performed to characterize the experimental setup in its initial and chirp-optimized form for supercontinua generated in 2.3 mm sapphire and 2 mm CaF<sub>2</sub> plates. The typical pump diameter inside the cell was about 200  $\mu\text{m}$  in all cases, the diameter of the SC probe and reference beams was in the range between 100 - 160  $\mu\text{m}$ . Compressed NOPA pump pulses ( $\approx 75$  fs FWHM) and transform-limited SHG pump pulses were used. Experiments were performed for generating XPM in the sapphire cell windows ( $d = 0.2$  mm) alone and for XPM from the complete cell with different solvents. The detailed results presented below highlight the specific dependencies of the XPM and the SC chirp on the experimental conditions, which were used as guides for the optimization of the experiment.

(i) As a first case, the supercontinuum probe pulse generated in CaF<sub>2</sub> was studied. The SC was generated in a rotating CaF<sub>2</sub> plate (2 mm thickness) from 775 nm pulses with 2.5  $\mu\text{J}$  pulse energy. To collimate the SC an achromatic lens ( $f = 30$  mm, central thickness = 10.9 mm) was used. The pump pulse was a compressed NOPA pulse (FWHM = 75 fs) with a pulse energy of 0.15  $\mu\text{J}$  and centered at 478 nm. For detection, the SC spectrum (see Fig. 4.4 a)) was clipped on both sides using BG18 and OG515 (Schott) filters. The delay was varied in 86 steps of 15 fs. The pump and probe pulses overlap for generation of the XPM in a sapphire window of 0.2 mm thickness. Figure 4.2 shows a contour plot of the transient changes in optical density  $A(\lambda, t)$ . The color coding for the optical density changes is from  $-4 \times 10^{-3}$  (dark blue) to  $5 \times 10^{-3}$  (red). The only contribution to  $A(\lambda, t)$  is from XPM. The XPM contribution has positive and negative amplitudes (red and blue, respectively) and can clearly be distinguished from the background (green). The wavelength dependence of the time-zero delay can clearly be seen:

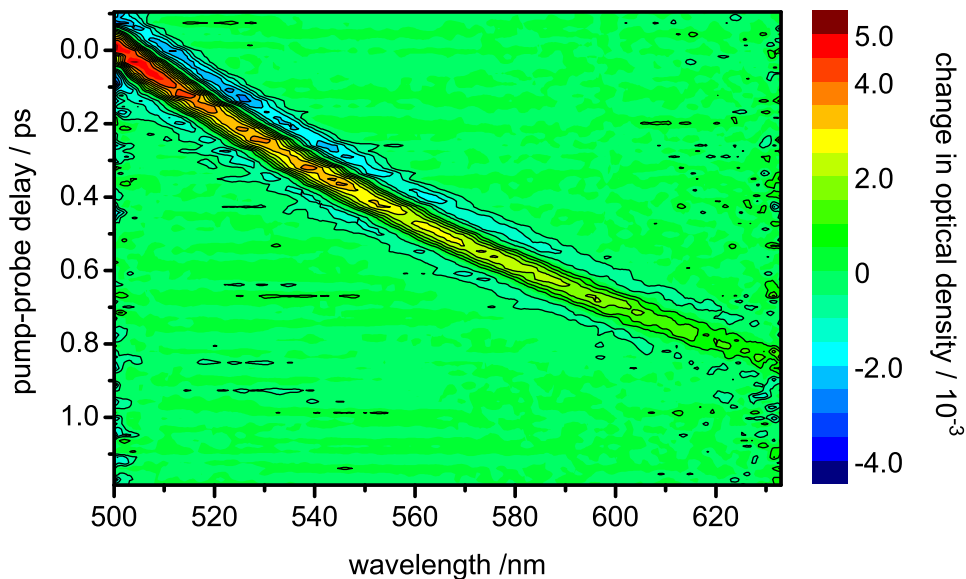


Figure 4.2: Contour plot representation of the XPM signal generated in a 0.2 mm sapphire window. The probe pulse is CaF<sub>2</sub>-SC, the pump pulse is a compressed NOPA pulse centered at 478 nm ( $E_{478nm} = 0.15 \mu\text{J}$ ).

at short wavelengths the XPM occurs at  $\tau \approx 0$  ps (upper left corner), at larger wavelengths, it occurs at positive delays up to  $\tau \approx 0.8$  ps. The amplitude of the positive maximum of the XPM is largest at short wavelengths. The overall behavior of the XPM is very similar to the simulation of Fig. 4.1. The characteristic “w” shape of the signal, and the asymmetry at the long wavelengths are reproduced. The amplitude of the maximum decreases with increasing wavelength. The position of the maximum shifts in time, reflecting the chirp of the SC pulse, and nearly coincides with the maximum of the pump-probe cross-correlation. The widths of the XPM signal and the pump-probe cross-correlation are almost identical.

Figure 4.3 shows cuts of  $A(\lambda, t)$  at six fixed wavelengths. The red lines represent fits to the XPM by Eq. (4.6), the blue lines are the pump-probe cross-correlations. A linear chirp rate of  $\beta = 4.2 \times 10^{-4} \text{ fs}^{-2}$ , a probe pulse width of  $\tau_{pr} = 120$  fs, a probe center wavelength of 502 nm ( $\Omega_{pr} = 3.757 \text{ fs}^{-1}$ ), and a pump center wavelength of 478 nm ( $\omega_p = 3.943 \text{ fs}^{-1}$ ) were used. These parameters were all kept constant for all wavelengths. The fitting parameters were the time-zero, the pump pulse temporal width  $\tau_p$  and the XPM amplitude.

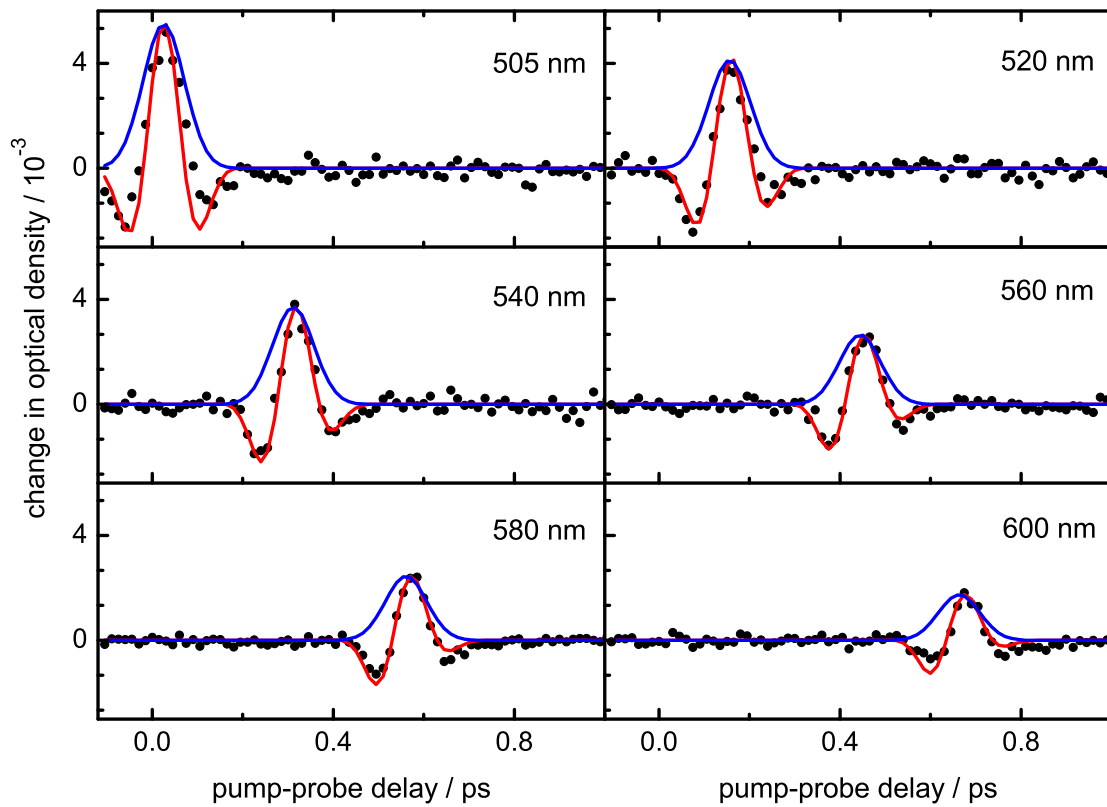


Figure 4.3: XPM signal generated in a 0.2 mm sapphire window. The  $\text{CaF}_2$ -SC was focused with an achromatic lens. The red curves represent the fit of the XPM signal for linearly chirped probe pulse. The blue curves represent the pump-probe cross-correlation. See also text.

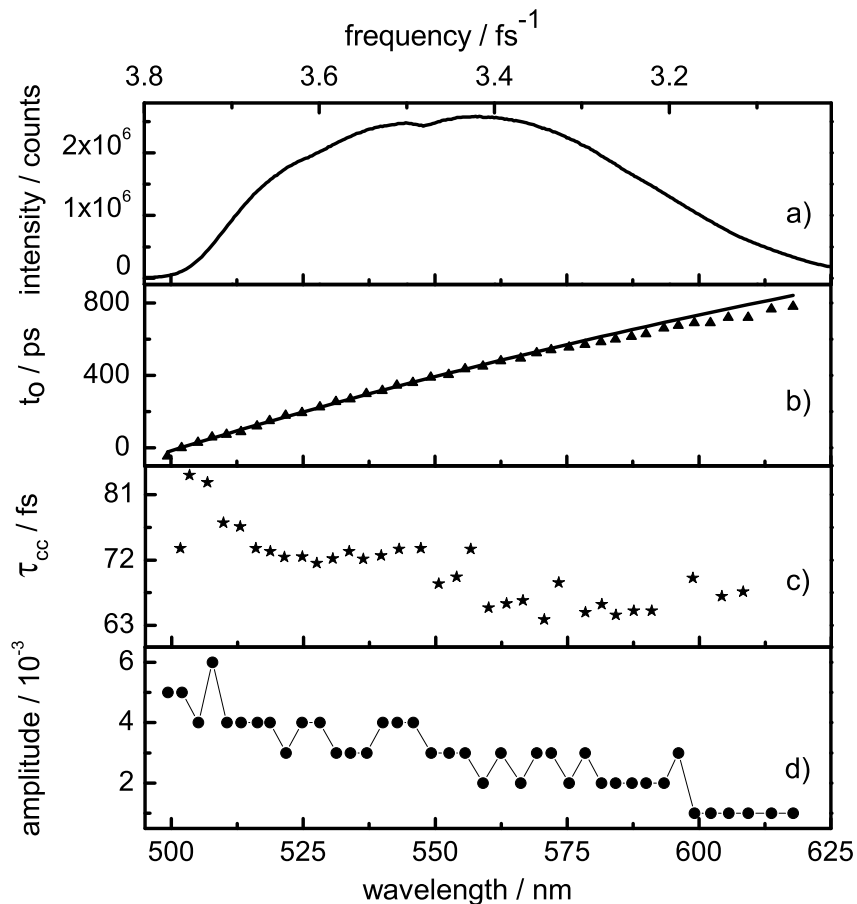


Figure 4.4: a) *Experimental CaF<sub>2</sub>-SC spectrum when using BG18 and OG515 filters*, b) *wavelength dependence of time-zero function  $t_0$* , c) *cross-correlation width  $\tau_{cc}$*  and d) *amplitude of the XPM signal generated in a 0.2 mm sapphire window.*

As can be seen from Fig. 4.3 the XPM can be described well with the chosen set of constant parameters for all six wavelengths. The results of the fits are summarized in Fig. 4.4. Part a) shows the spectrum of the CaF<sub>2</sub>-SC. The wavelength dependence of the time-zero function  $t_0$  is shown in part b). The values of  $t_0$  are represented by triangles and were obtained directly from  $A(\lambda, t)$  by taking the position of the maximum of the XPM feature at the desired wavelength. The solid black line represents a description of the time-zero function according to Eq. (4.4), with  $\beta = 4.2 \times 10^{-4} \text{ fs}^{-2}$ . A comparison of the time-zero values shows a good agreement (a maximum deviation of  $\approx 8 \text{ fs}$  is found). This is expected on the basis of Eq. (4.6), which predicts a maximum of the XPM at  $t_d = t_0$ . Since Eq. 4.6 is valid for linearly chirped pulses it follows that the chirp of the SC is almost linear. Part c) of Fig. 4.4 shows the cross-correlation

width  $\tau_{cc}$ , which was set to the value of  $\tau_p$  from the fits assuming the fast chirp rate condition. The cross-correlation width only changes very little (from  $\tau_{cc} \approx 83$  fs at  $\lambda_{probe} = 500$  nm to  $\tau_{cc} \approx 65$  fs at  $\lambda_{probe} = 620$  nm). The average value of 74 fs agrees well with the value obtained by autocorrelation of the compressed NOPA pump pulse (75 fs) (see Fig. 4.5). Part d) of Fig. 4.4 shows the amplitude of the XPM. The amplitude shows a decrease with increasing probe wavelength.

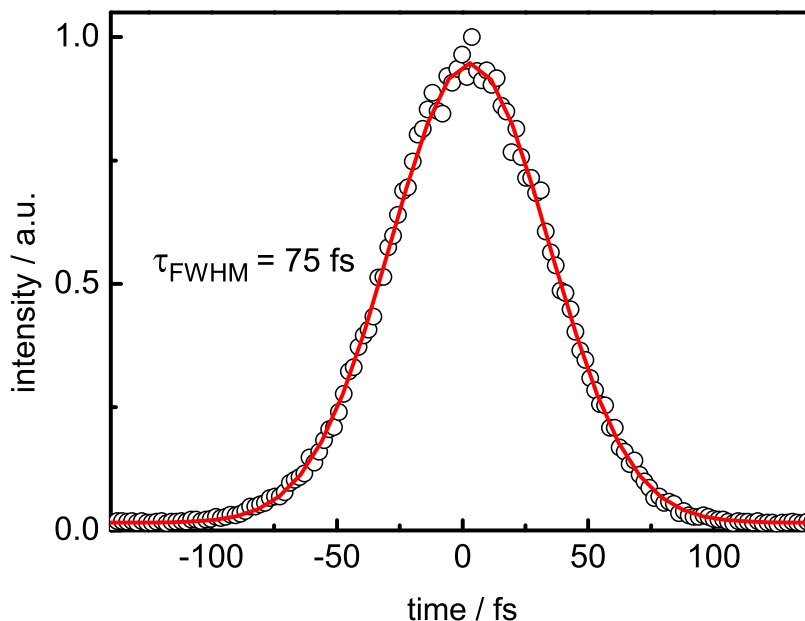


Figure 4.5: Autocorrelation function of the NOPA pulse  $\lambda_{pump} = 478$  nm (circles) together with a Gaussian fit (red line).

(ii) As second case, SCG in sapphire was studied. Almost  $1 \mu\text{J}$  of 775 nm pulses were focused with a lens ( $f = 50$  mm) into a 2.3 mm thick sapphire plate and a compressed NOPA pump pulse centered at 466 nm with a temporal width of 75 fs (FWHM) was used. The probe and pump beam were overlapped inside the sample cell filled with  $\text{CCl}_4$ . A smaller pump energy of  $0.45 \mu\text{J}$  was chosen to minimize any unwanted contribution of ISRS from the solvent. To minimize the amount of dispersive material in the SC optical path, its collimation was performed with an off-axis parabolic mirror (see Sec. 3.2.4). The SC was clipped with BG18 and OG515 filters. Figure 4.6 shows a contour plot of the change in optical density  $A(\lambda, t)$  of the experimental data, measured at 30 delays with steps of 10 fs. The range is from  $-1 \times 10^{-3}$  (blue) to  $+1 \times 10^{-3}$  (red). The XPM contribution can be seen in the delay range between -0.1



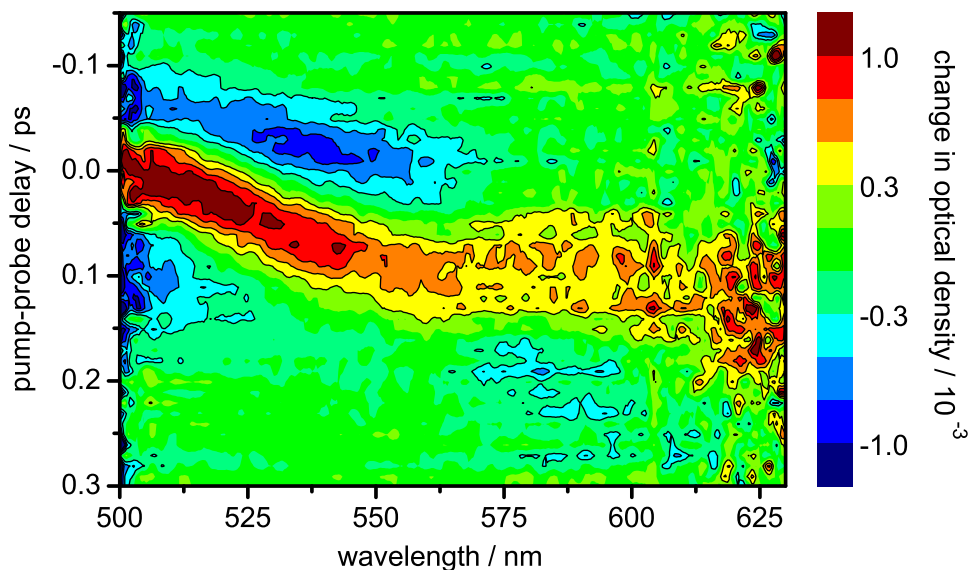


Figure 4.6: Contour plot representation of the XPM signal generated in pure  $\text{CCl}_4$ . The probe pulse is sapphire-SC, the pump pulse is a compressed NOPA pulse centered at 466 nm ( $E_p = 0.45 \mu\text{J}$ )

to 0.15 ps with the lowest delay values for the shorter wavelengths. The delay position of the XPM maximum changes by only 0.1 ps over the wavelength range of  $\lambda = 500 - 630$  nm. From  $\lambda = 575$  nm to  $\lambda = 630$  nm the time zero delay stays nearly constant. The amplitude of the XPM is much reduced in comparison to Fig. 4.2 and is smaller at long wavelengths at which the negative parts of the XPM signal are hardly recognizable from the background. As above, cuts at fixed wavelengths were fitted according to Eq. (4.6) using as fixed parameters: chirp rate  $\beta = 1.8 \times 10^{-3} \text{ fs}^{-2}$ , central probe wavelength  $\lambda_{probe} = 505$  nm ( $\Omega_{pr} = 3.7313 \text{ fs}^{-1}$ ) and probe duration  $\tau_{pr} = 120$  fs. Cuts and fits at six selected wavelengths are displayed in Fig. 4.7. The typical shape of the XPM can be seen at all wavelengths. The amplitude of the positive maxima is low, decreasing from  $+1.2 \times 10^{-3}$  at  $\lambda = 505$  nm to  $+0.6 \times 10^{-3}$  at  $\lambda = 560$  nm. The points are the time-zero delay for the probe wavelengths, the red lines represent fits to the XPM by Eq. (4.6), the blue lines are the pump-probe cross-correlations. The fits describe the XPM data fairly well for all six chosen wavelengths.

Figure 4.8 summarizes the results and shows the experimental spectrum of the sapphire SC (in part a)). Part b) shows the time-zero function (where the delay values were determined as above). Part c) of Fig. 4.8 shows the cross-correlation width  $\tau_{cc}$ , which was also set to the

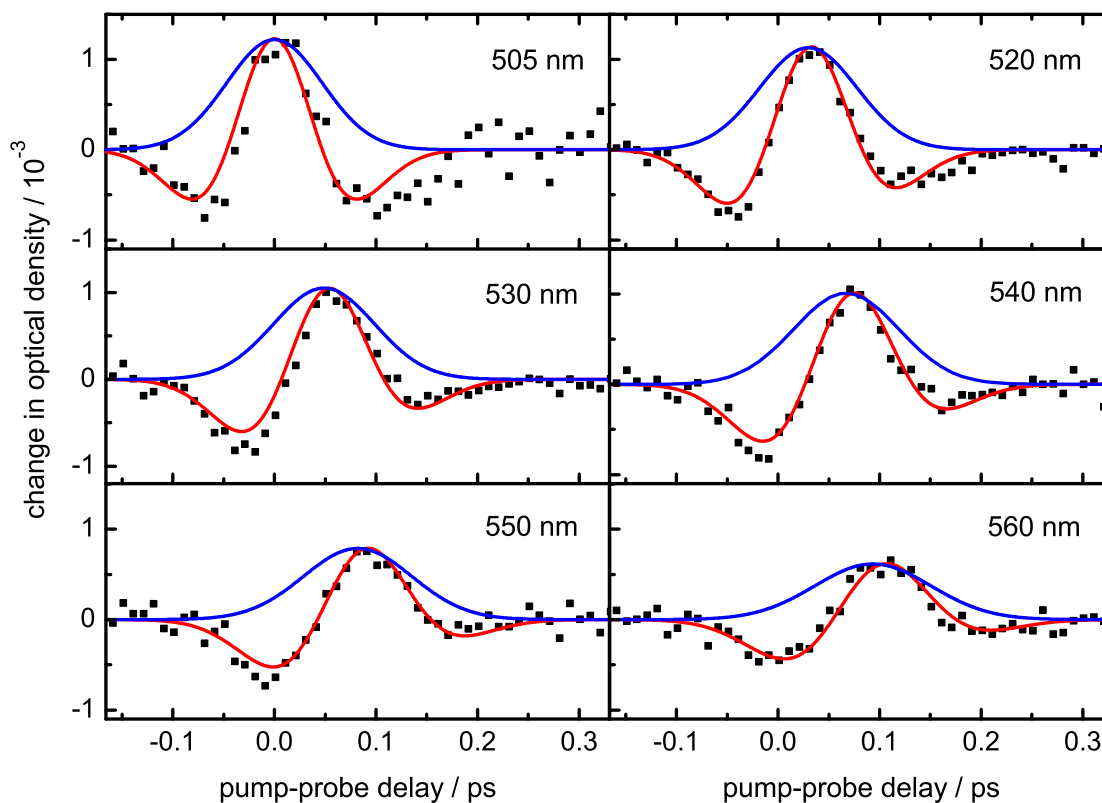


Figure 4.7: XPM signal generated in pure  $\text{CCl}_4$ . The sapphire-SC was focused with an off-axis parabolic mirror. The red curves represent the fit of the XPM signal for a linearly chirped probe pulse. The blue curves represent the pump-probe cross-correlation. For the fit parameters, see text.

value of  $\tau_p$  from the fits. The cross-correlation width only changes very little (from  $\tau_{cc} \approx 85$  fs at  $\lambda_{probe} = 500$  nm to  $\tau_{cc} \approx 65$  fs at  $\lambda_{probe} = 680$  nm). The amplitude of the XPM is displayed in part d).

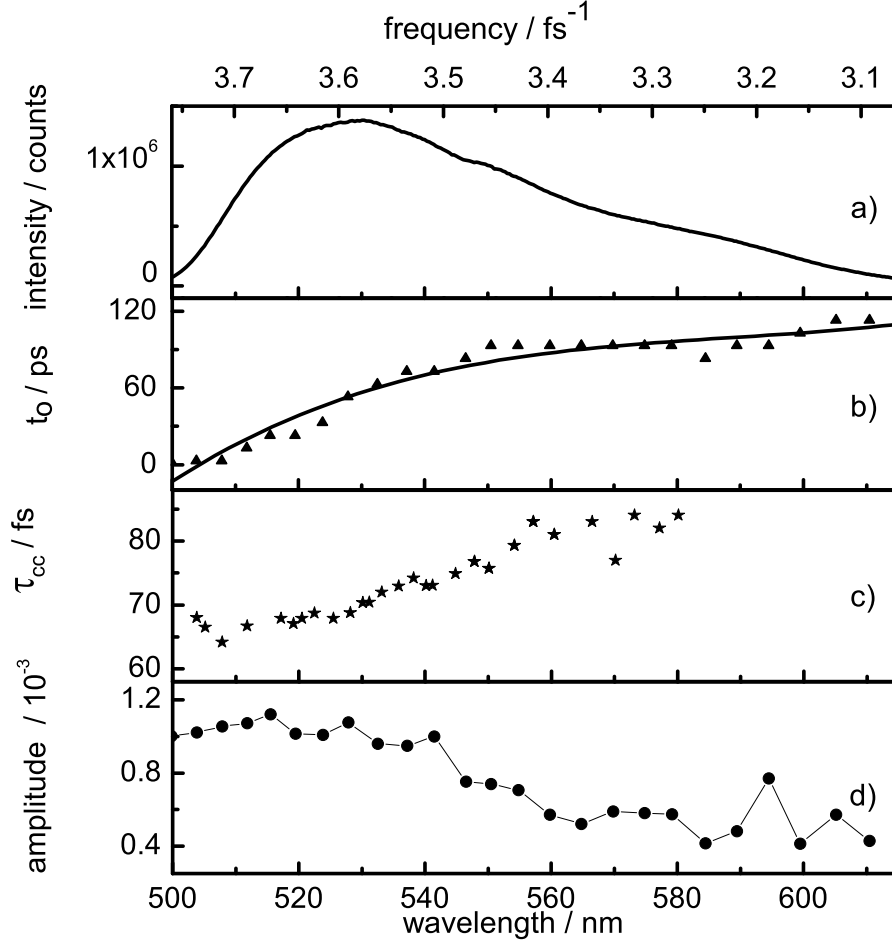


Figure 4.8: a) *Experimental sapphire-SC spectrum when using BG18 and OG515 filters*, b) *wavelength dependence of time-zero function  $t_0$* , c) *cross-correlation width  $\tau_{cc}$* , d) *amplitude of XPM signal generated in  $CCl_4$* .

In Fig. 4.9 a third order polynomial fit of the time-zero function is compared to a linear fit, since there are clear deviation from linearity. The points are the time zero delay for each wavelength, the red line is the linear fit and the blue line a third order polynomial. It can be seen that the non-linear contribution should be taken into account for a best time-zero correction.

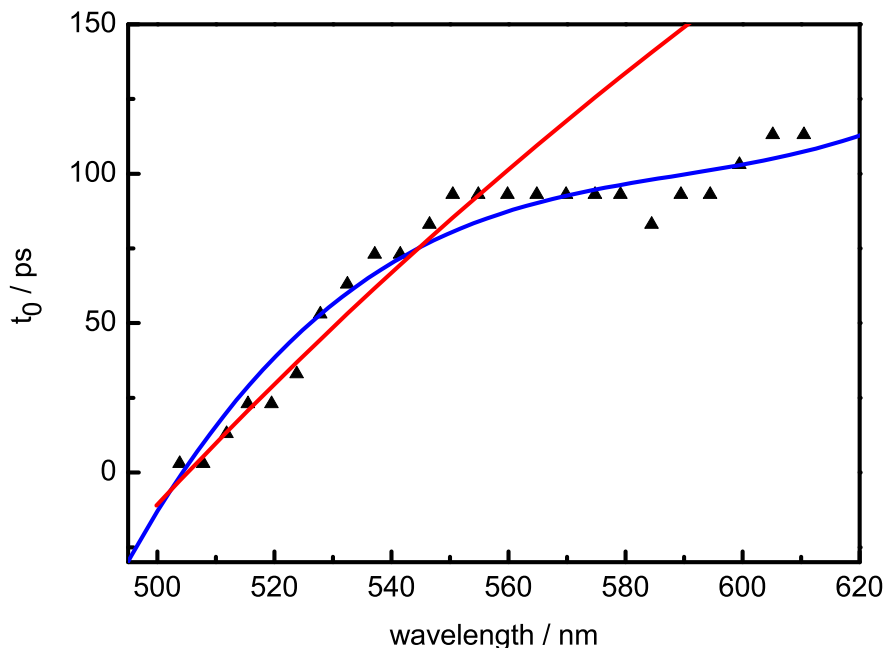


Figure 4.9: *Time-zero function obtained from XPM signal generated in  $\text{CCl}_4$ . The red line represents the linear fit and the blue line is the fit with a third order polynomial.*

(iii) The third set of data is representative for experiments that use excitation in the UV with SHG pump pulses at 387 nm, using the chirp optimized setup. The SHG pump pulses are temporally broader than the compressed NOPA pulses, but are unlikely to be chirped. The data were treated as described above. Figure 4.10 shows the experimental data, which were taken at delay steps of 15 fs. The SC was clipped to a usable wavelength range of 470 nm to 700 nm by use of a BG38 filter (Schott) and a cut off filter (Edmund Optics). The range is from  $-3.2 \times 10^{-3}$  (blue) to  $+3.2 \times 10^{-3}$  (red). The amplitude of the XPM is significant only at small wavelengths (by comparison, it is very hardly visible at longer wavelengths). The time zero delay changes by approximately 0.25 ps over the entire wavelength range, with the lowest delay values for the shorter wavelengths. The temporal width of the XPM feature is increased by comparison to Fig. 4.2 and 4.6. The fits at selected wavelengths displayed in Fig. 4.11 were performed with a fixed chirp rate of  $\beta = 1.8 \times 10^{-3} \text{ fs}^{-2}$ , a central probe wavelength of  $\lambda_{probe} = 495 \text{ nm}$  ( $\Omega_{pr} = 3.832 \text{ fs}^{-1}$ ) and a probe width  $\tau_{pr} = 120 \text{ fs}$ . As before, the amplitude of the XPM decreases for the longer wavelength. The typical XPM shape is again reproduced. The reversal of the asymmetry on both sides of the probe central wavelength and the symmetric shape at  $\lambda = 495 \text{ nm}$  can be seen. The increased pulse width of the pump

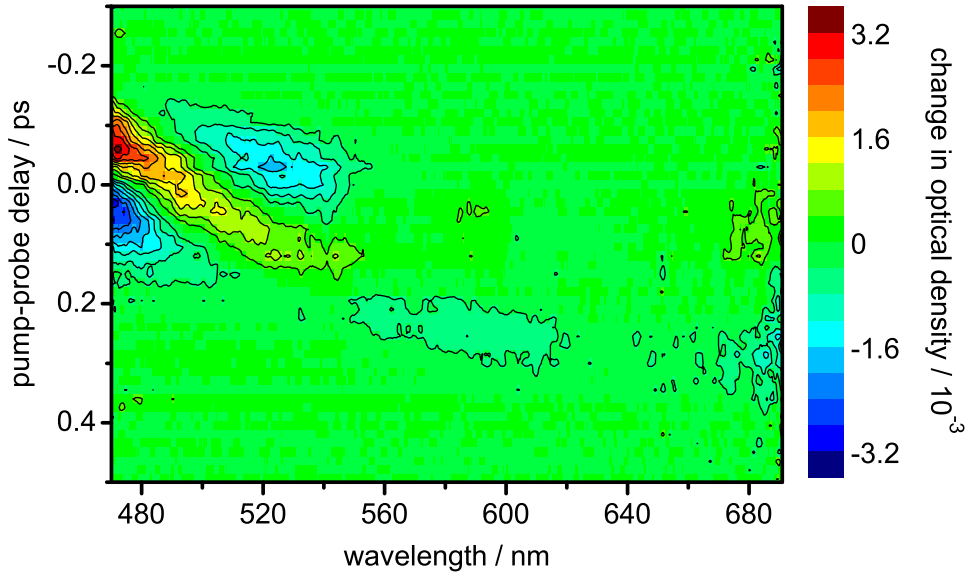


Figure 4.10: *Contour plot representation of the XPM signal generated in pure ethanol. The probe pulse is the sapphire-SC, the pump pulse is SHG centered at 387nm ( $E_{387nm} = 0.65 \mu\text{J}$ )*

pulse is immediately discernible in the broader XPM features. The quality of the fits is as good as above. The experimental SC spectrum, time-zero values, and XPM amplitudes are shown in Fig. 4.12. The time zero delay values displayed in part b) (triangles) were fitted with a third-order polynomial (black line) and no satisfactory linear fit could be achieved. The decrease of the XPM amplitude towards longer wavelengths can be seen in part c).

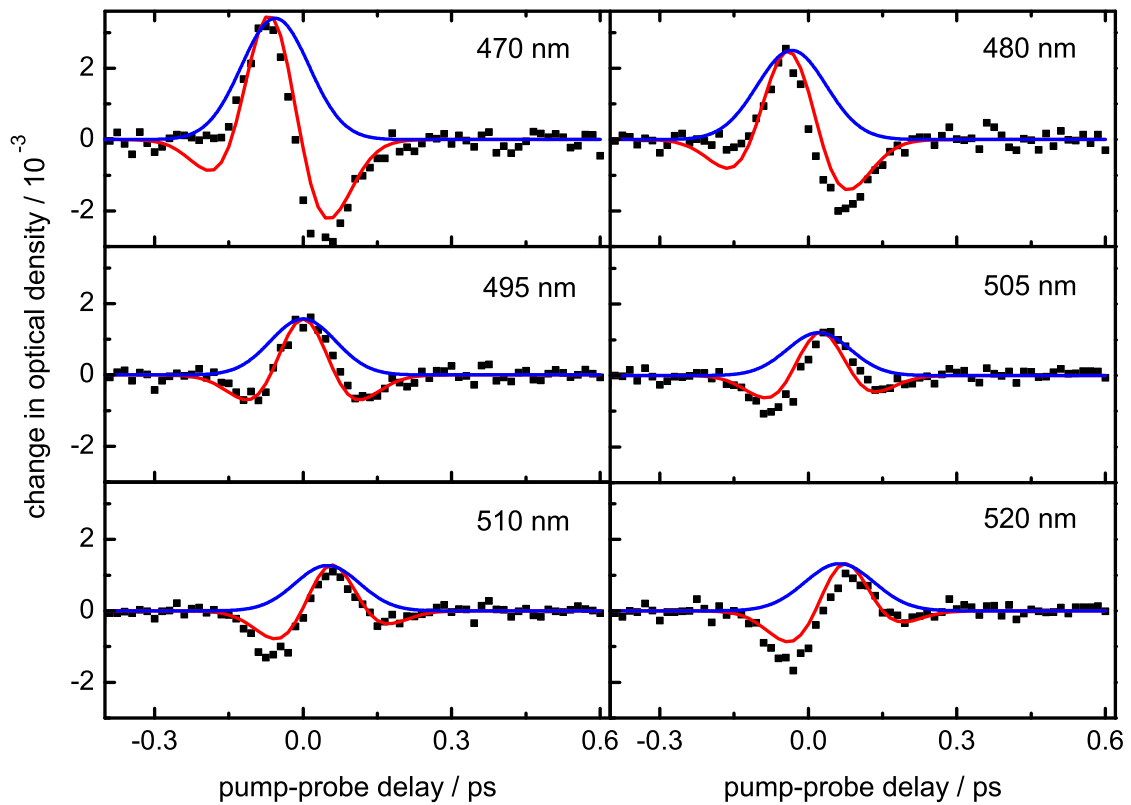


Figure 4.11: XPM signal generated in pure ethanol. The sapphire-SC was focused with an off-axis parabolic mirror. The red curves represent the fit of the XPM signal for a linearly chirped probe pulse. The blue curves represent the pump-probe cross-correlation. For the fit parameters, see text.

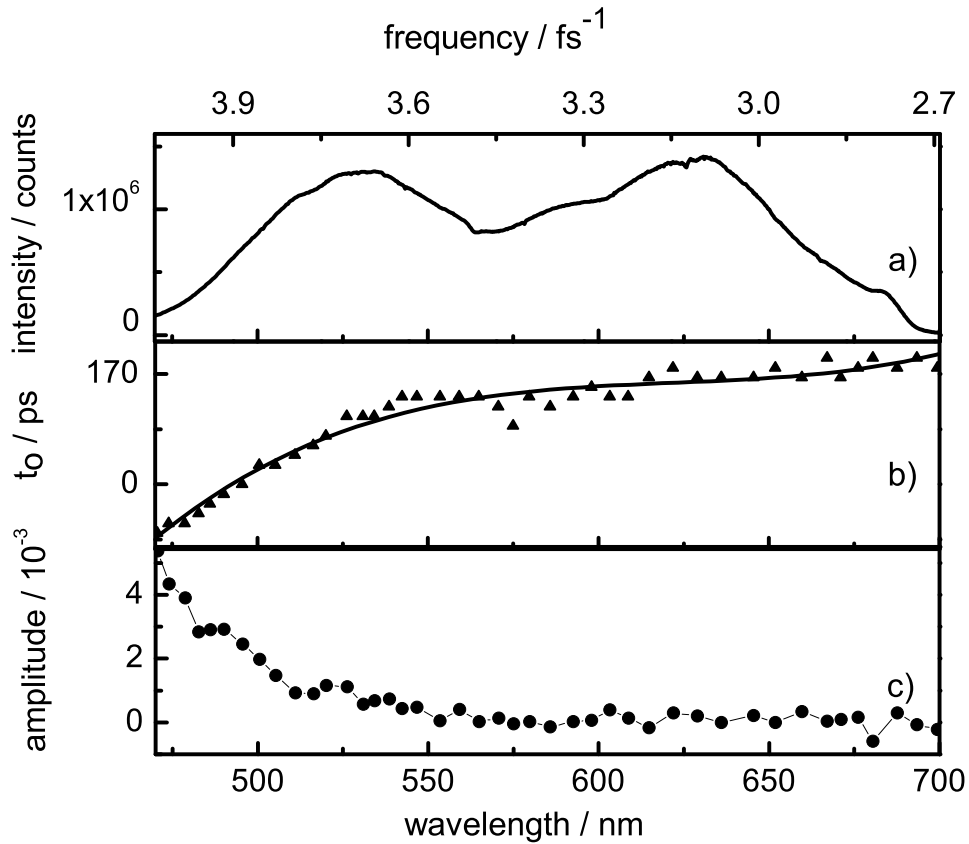


Figure 4.12: a) Experimental sapphire-SC spectrum when using BG38 and cut off 700 filters, b) wavelength dependence of time-zero function  $t_0$ , c) amplitude of XPM signal generated in a 0.2 mm sapphire window.

(iv) The final point regards the pump intensity dependence of the XPM amplitude. The pump energy was varied by means of different neutral filters placed in the optical path of the pulse. Figure 4.13 shows the XPM amplitude in pure hexane at four selected wavelengths for pump energies of 0.58, 0.85, 1 and 1.2  $\mu\text{J}$  (NOPA pump pulse at 466 nm, FWHM = 75 fs) with everything else kept constant (black squares). The intensities were determined with a LM-1 detector (Coherent). The lines in Fig. 4.13 indicate linear fits of the observed power dependence. The XPM amplitude increases linearly with the pump energy and decreases approximately by a factor of 5 going from a probe wavelength of 500 nm to 580 nm. Figure 4.14 summarizes the results on the supercontinuum chirp and the time-zero behavior for the experimental conditions. The data for the  $\text{CaF}_2$ -supercontinuum in the chirp-reduced setup were provided by A. Petter [109] and show the lowest chirp of all data.

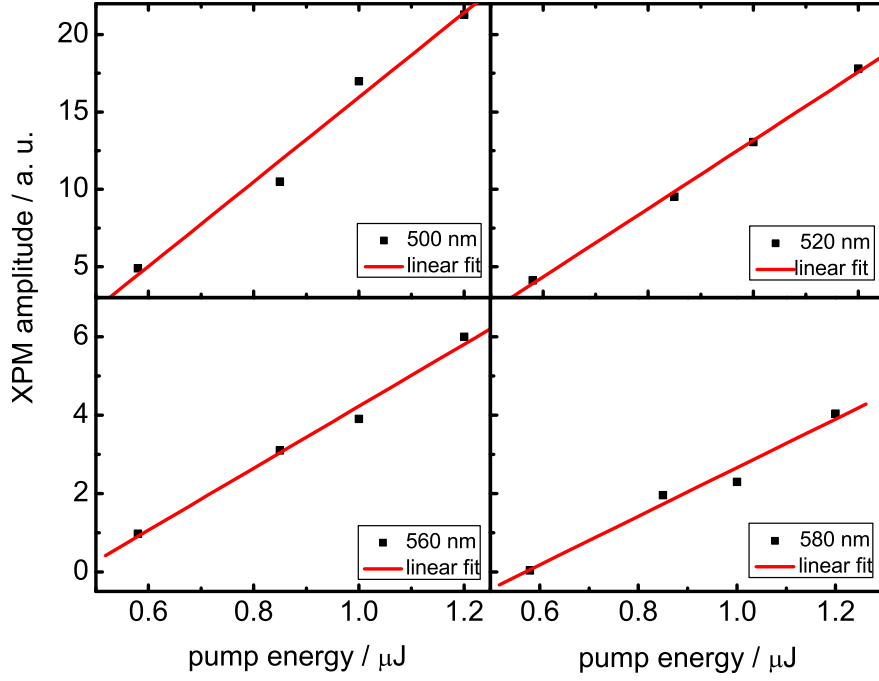


Figure 4.13: Dependence of the XPM signal generated in hexane on the pump energy ( $\lambda_{\text{pump}} = 466 \text{ nm}$ ) for different probe wavelengths. The pump energy was varied using different neutral filters (NG11, NG5 and NG4) from  $0.58 \mu\text{J}$  to  $1.2 \mu\text{J}$ .

In Table 4.1 the results obtained from the fits of Eq. 4.6 to the XPM are summarized.

Table 4.1: Fit results of XPM signal generated for different experimental conditions.

White light	focus condition	sample	$\Omega_2 / \text{fs}^{-1}$	$\tau_2 / \text{fs}$	$\beta / \text{fs}^{-2}$	$\lambda_{\text{pump}} / \text{nm}$	$\tau_1 / \text{fs}$
CaF <sub>2</sub>	lens	0.2 mm sapphire	3.75	120	$4.2 \times 10^{-4}$	478	62 - 82
sapphire	lens	pure hexane	3.75	120	$3.9 \times 10^{-4}$	478	65 - 85
sapphire	mirror	pure CCl <sub>4</sub>	3.73	120	$1.8 \times 10^{-3}$	466	65 - 85
sapphire	mirror	pure ethanol	3.83	120	$1.8 \times 10^{-3}$	387	82 - 99



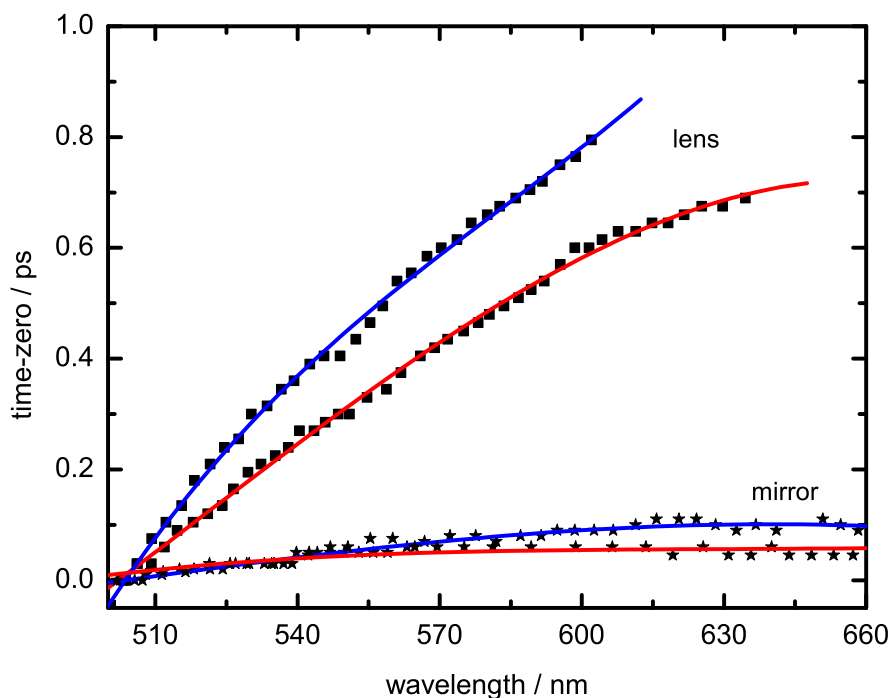


Figure 4.14: *Time-zero behavior for SC generated in sapphire (blue lines and symbols) and  $\text{CaF}_2$  (red lines and symbols) for different focusing: squares for use of an achromatic lens and stars for the off-axis parabolic mirror.*

## 4.1.2 Stimulated Raman Amplification

### 4.1.2.1 Background

The stimulated Raman effect occurs by the coherent interaction of the pump and probe beam in a medium with a vibrational resonance at the pump-probe difference frequency. On the Stokes side,  $\omega_{vib} = \omega_p - \omega_S$  must be fulfilled, where  $\omega_p$  is the pump frequency, and  $\omega_S$  is equal to the Stokes frequency (which is from the probe beam). The coherent excitation of the transition, which is “seeded” by the probe photon at  $\omega_S$ , leads to the emission of the photons at the Stokes frequency, *i. e.* to a negative contribution to the change in optical density at  $\omega_S$  (on the anti-Stokes side, a positive signal is generated). For strong Raman modes, the stimulated Raman amplification (SRA) signal can be much higher than the XPM signal and can provide the pump-probe cross-correlation at the Stokes frequencies. Since in the TA detection the signal is spectrally dispersed, phase information about the pump pulse can also be gained (compare with paragraph on FROG pulse characterization in Sec. 3.1.2).

## 4.1.2.2 Results

Since the process of SRA is not the main focus of this work, results are given only for one example case and are discussed qualitatively. Figure 4.15 shows the change in optical density in pure hexane for excitation with a NOPA pulse centered at 478 nm (part a) and b)) and at 466 nm (part c) and d)), using four different settings of the pulse compressor. The stimulated Raman signal can be seen as large negative contribution (blue colors) at a wavelength of about 540 - 550 nm. The XPM contribution is strongest at small wavelengths and has a much smaller amplitude (approximately by a factor of 5-6) compared to the SRA signal. The different shapes of the SRA contributions in the different part of Fig. 4.15 can be clearly seen.

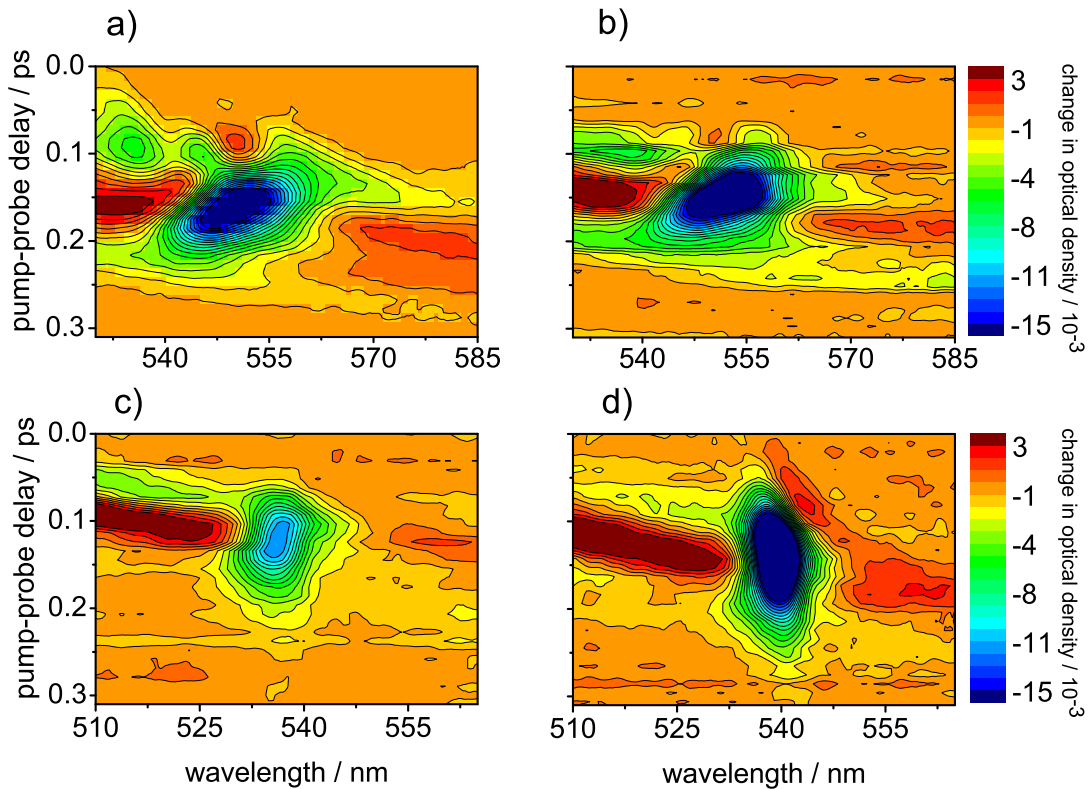


Figure 4.15: Comparison of different SRA profiles for a) and b) an inhomogeneous NOPA pulse, c) and d) a homogeneous NOPA pulse.

Intensity autocorrelation functions (ACFs) of the pump pulses were obtained with the APE autocorrelator. Figure 4.16 a)-d) shows the raw data (black squares) and the ACFs as red lines.

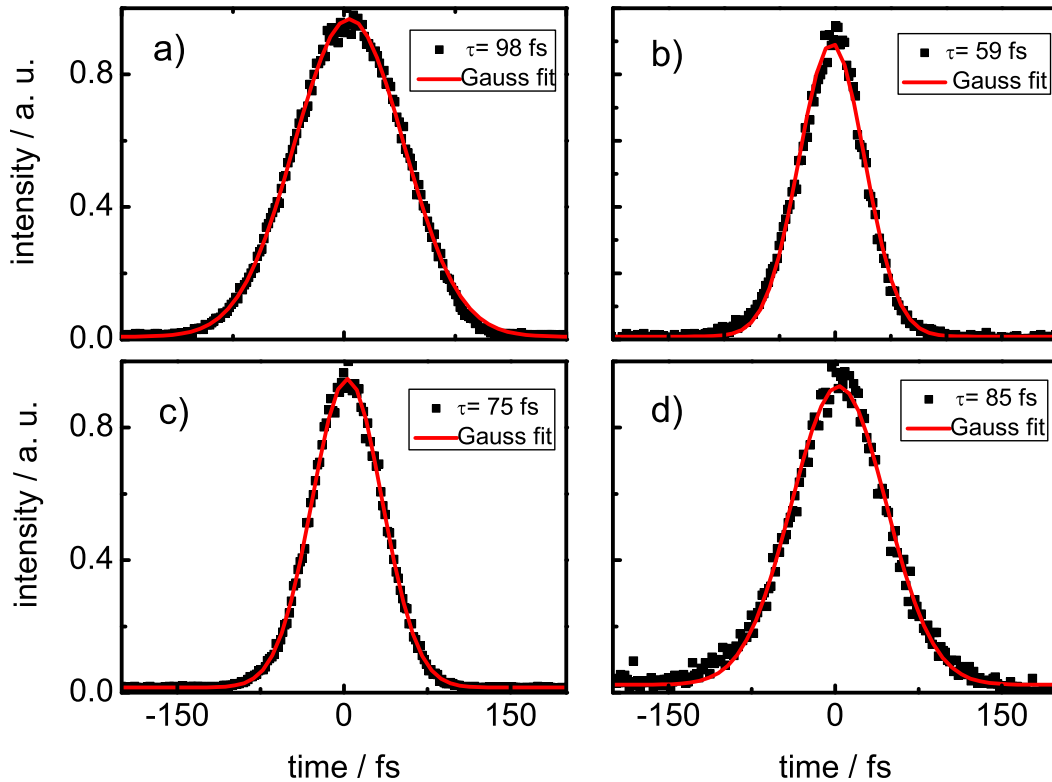


Figure 4.16: Autocorrelation function of the pump pulses (measured with the APE autocorrelator) used for generation of the SRA signals. The pulse widths (FWHM) are: a) 98fs, b) 59 fs, c) 75 fs, d) 85 fs.

The autocorrelation function (ACF) in all cases can be described well with a Gaussian, even though different pulse widths have to be used. On the basis of the ACFs, one would conclude that the best compressor setting was chosen in case b). For such a perfectly compressed pulse, a Gaussian shape is expected spectrally and temporally, and the same should be true for the shape of the SRA signal if the chirp of the SC light is neglected. As can be seen in Fig. 4.15, the best approximation to a Gaussian shape in time and spectrum is not found for the case b), but for case c), the other cases show clear deviations. The pulse width extracted from the SRA signal  $\tau_{FWHM} = 72$  fs coincides with the ACF width in case c) of Fig. 4.16. The results show that the parameters from the ACF of compressed NOPA pulses have to be

regarded as approximate. In particular, Gaussian-shaped ACFs can occur even for over- or undercompressed chirped pulses. As a consequence, for experiments with compressed NOPA pulses, the pump pulse characteristics and compressor settings were checked qualitatively by inspection of the generated SRA signal whenever possible.

Figure 4.17 compares the SRA signal in pure *n*-hexane and the spectrum of the pump pulse. The SRA spectrum was obtained by temporal integration of the TA signal around time-zero to remove the XPM contribution, the pump pulse spectrum was recorded with a CCD spectrometer (APE). The almost identical spectral shape is obvious, and the spectral

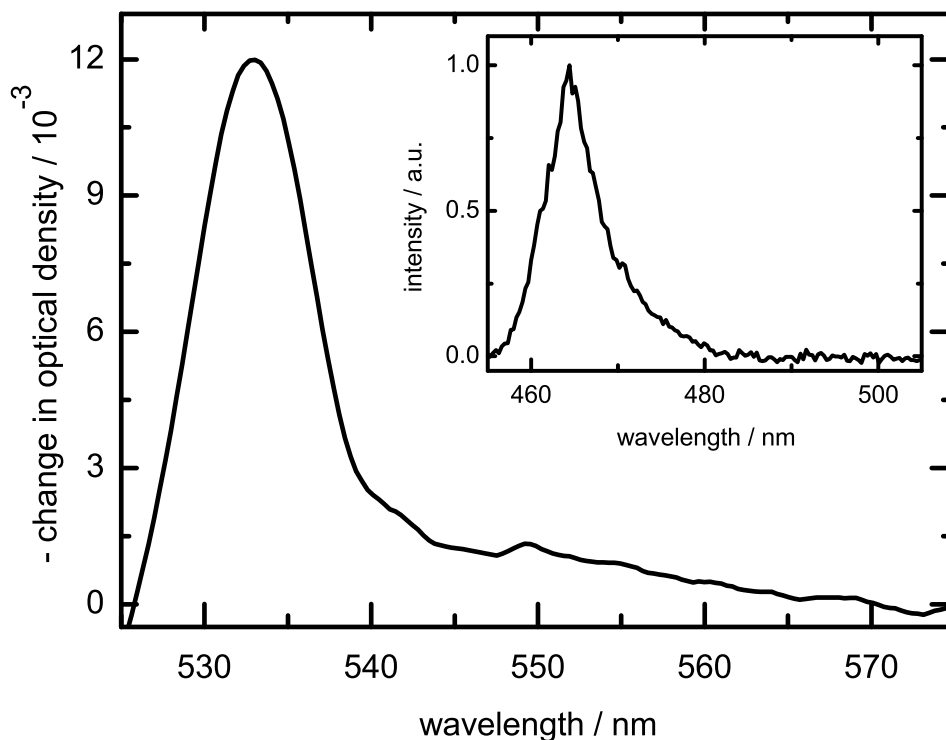


Figure 4.17: *The generated SRA signal in pure n-hexane and as inset the spectrum of the 466 nm pump pulse (measured with APE CCD spectrometer).*

shift from  $\approx 466$  nm to  $\approx 535$  nm corresponds to a Raman line at  $\approx 2770$   $\text{cm}^{-1}$  which can be attributed to the Raman-active C-H stretching mode found at  $2876$   $\text{cm}^{-1}$  in spontaneous Raman spectra of hexane. The slight shift of the frequency can be explained by non-linear effects in the medium [110].

Since subtraction of the stimulated Raman contribution is difficult, the pump power dependence of its amplitude was checked. The amplitudes at the maximum of the SRA at  $\lambda = 535$

nm are shown in Fig. 4.18. The amplitudes show a linear power dependence in accord with

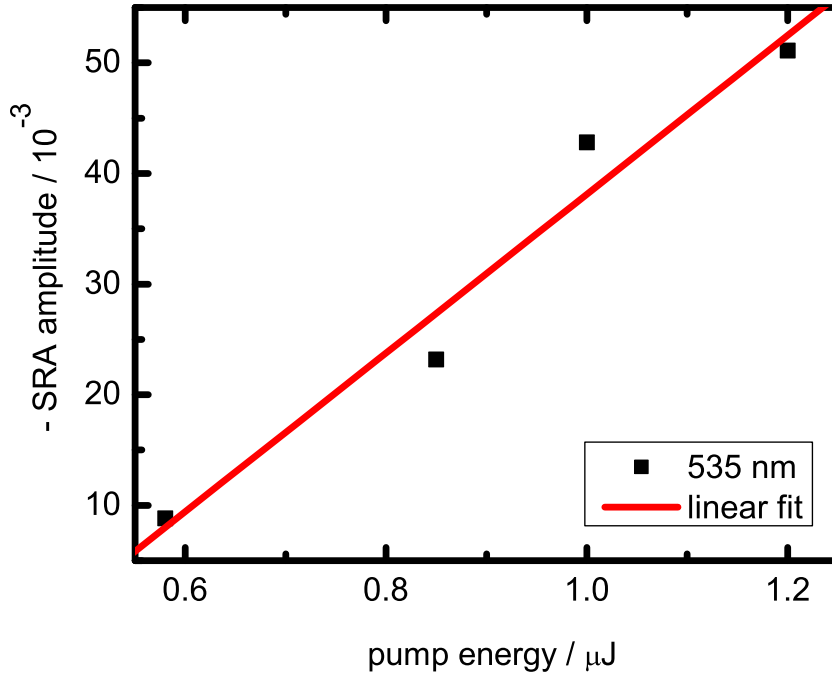


Figure 4.18: *Dependence of the SRA signal from pure n-hexane on the pump energy ( $\lambda_{\text{pump}} = 466 \text{ nm}$ ) at  $\lambda_{\text{probe}} = 535 \text{ nm}$ .*

the theory. The relative strength of the SRA signal with respect to the genuine TA signal cannot be changed by a simple pump power variation.

### 4.1.3 Impulsive Stimulated Raman Scattering

#### 4.1.3.1 Background

Impulsive stimulated Raman scattering (ISRS) is the time analog of the SRA signal, which occurs if the spectral bandwidth of the pump pulse exceeds the frequency of a Raman active mode of the medium. In this case, the pump pulse contains photons at the pump and the Stokes frequency and will excite the respective vibrations coherently [111]. The effect will lead to damped oscillations in the TA signal that correspond to a superposition of all excited Raman modes. At time-zero, *i.e.* for overlapping pump-probe pulses, the signal has the same shape as the XPM.

## 4.1.3.2 Results

Figure 4.19 shows the TA signal of pure  $\text{CCl}_4$  obtained from NOPA excitation at 466 nm,  $\tau = 70$  fs (FWHM of the autocorrelation function). At delays between  $\tau \approx 0.1$  ps for  $\lambda = 480$

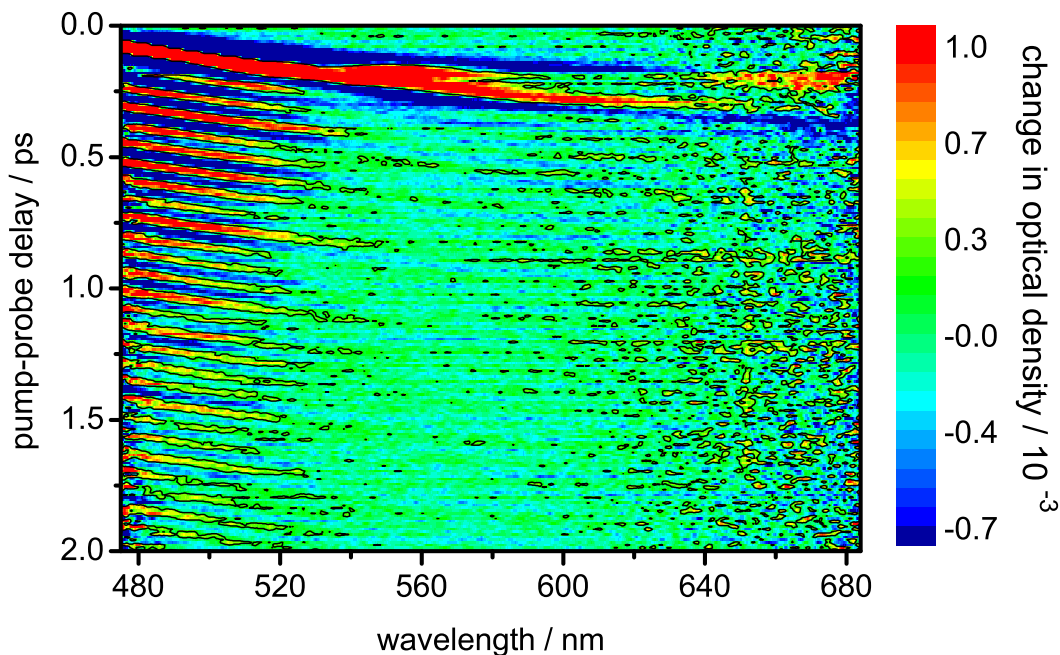


Figure 4.19: *Contour plot representation of the XPM and ISRS signal generated in pure  $\text{CCl}_4$ . The probe pulse is sapphire-SC, the pump pulse is a compressed NOPA pulse centered at 466 nm ( $E_p = 0.65 \mu\text{J}$ )*

nm and  $\tau \approx 0.25$  ps for  $\lambda = 640$  nm, the XPM contribution can be seen. At larger delays, the change in optical density shows oscillations which are best visible for the short wavelengths and persist up to delays of 2 ps. Figure 4.20 shows cuts of the TA signal at four wavelengths. The oscillatory behavior of the ISRS contributions can be seen best for  $\lambda = 500$  nm. The initial behavior is given by the typical XPM signal in each case. The amplitude of the oscillations decreases with increasing detuning from the pump wavelength. A quantitative description of the data following the treatment outlined in Kovalenko [103] was not performed. Instead, the frequencies of the excited Raman modes were obtained by performing a Fourier transform of the signal at 500 nm. The resulting power spectrum is displayed in Fig. 4.21. Although the resolution is low, three modes at  $224 \text{ cm}^{-1}$ ,  $322 \text{ cm}^{-1}$ ,  $474 \text{ cm}^{-1}$  can be discerned.

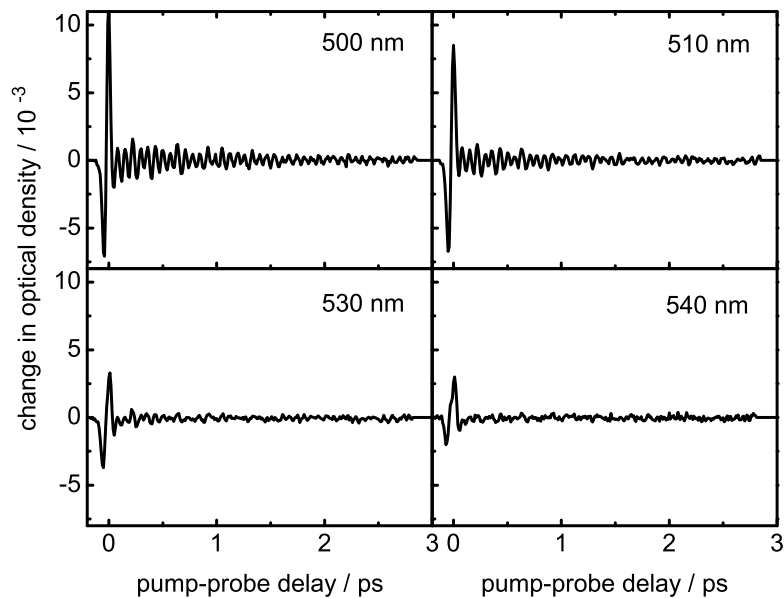


Figure 4.20: *XPM and ISRS signals of pure  $\text{CCl}_4$  for different probe wavelengths.*

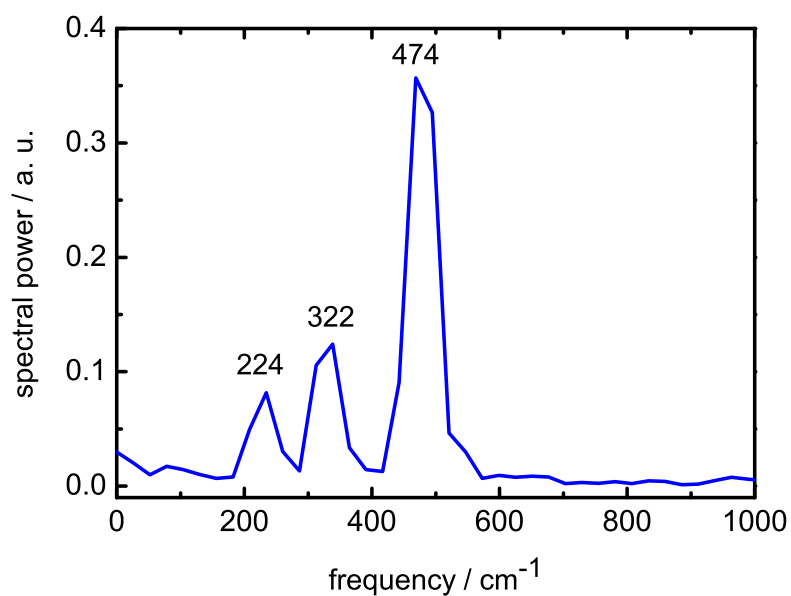


Figure 4.21: *Fourier spectra of the ISRS oscillations generated in pure  $\text{CCl}_4$ .*

#### 4.1.4 Conclusions and implications for the design of the TA setup

From the viewpoint of the experimenter, cross-phase modulation, stimulated Raman scattering and impulsive stimulated Raman scattering are unwanted contributions that deteriorate the performance of the experiment by decreasing the temporal resolution and that might obscure transient absorption signal from the molecule under study even up to several ps (in the case of the ISRS contribution). On the other hand, additional information for the characterization of the experimental parameters, such as SC chirp, time-zero function, instrument response function and the pump pulse width can be obtained from a study of the coherent contributions.

An important conclusion that can be drawn from the above data is that for the experimental setup used in this work, the theoretical description with non-chirped pump pulses and the SC probe pulses as single, linearly chirped pulses provide a good description of the observed XPM data. The likely residual chirp of the compressed NOPA pulses, does not seem to spoil the experiment. This allowed to determine the apparatus time-zero function accurately. One of the main results regarding XPM is that for collimation of the SC using an achromatic lens, a large chirp with a chirp rate of  $\beta = 4.2 \times 10^{-4} \text{ fs}^{-2}$  could be observed, whereas the use of reflective optics results in a much reduced chirp described by  $\beta = 1.8 \times 10^{-3} \text{ fs}^{-2}$ , and the amplitude of the XPM is much smaller (by a factor of 6). Apparently, the reduced chirp is mainly the consequence of the reduction of dispersive material in the beam path. In this “chirp-reduced” setup, the chirp is only approximately linear, because of the increased *relative* amplitude of the non-linear terms. The pump energy dependence of the XPM was found to be linear. But since there are only four data points for each fit only a qualitative statement can be made. A more suitable detector should have been available, since the accuracy and sensitivity of LM-1 is too low. Therefore, the quoted intensities have a large error.

It could be shown that the SRA signal provides an alternative way of determining the pulse shape of the pump pulse inside the sample. However, the signal amplitude of the SRA signal is very large and has a linear power dependence. Therefore, it cannot be decreased by a simple reduction of the pump power.

From the ISRS contribution, which can persist up to several picoseconds, three Raman lines of  $\text{CCl}_4$  could be determined. A comparison with literature data shows the excellent agreement with the lines at  $217 \text{ cm}^{-1}$ ,  $314 \text{ cm}^{-1}$  and  $460 \text{ cm}^{-1}$  found in spontaneous Raman spectra. The other Raman modes of  $\text{CCl}_4$  ( $761 \text{ cm}^{-1}$  and  $790 \text{ cm}^{-1}$ ) are either too weak to be seen in the power spectra of Fig. 4.21 or lie outside the spectral bandwidth of the NOPA pump pulse which is  $\Delta\omega \approx 418 \text{ cm}^{-1}$  as calculated from the pump pulse duration by assuming a transform limited pulse. The data suggest that in cases where the ISRS contribution cannot be avoided, filtering in the Fourier based on the knowledge of the Raman modes might improve the situation.



Since there is good agreement between the theoretical description and the experimental results, the coherent contributions might be handled directly by incorporating them into a global fit of the data as in Ref. [103]. However, the “practical” approach (which was chosen throughout this work) is to realize experiments with a XPM as little as possible, to perform an additional solvent scan and to subtract the unwanted contributions. The following guide lines help: First, *no* unnecessary dispersive optical material should be placed in the probe light beam path. Second, the SC generated in  $\text{CaF}_2$  has a smaller chirp than the one from sapphire (because  $\text{CaF}_2$  is a lower dispersive material). Therefore, all other experimental parameters being identical, a smaller XPM amplitude can be expected. Together with the increased bandwidth, this provides a strong argument for SCG in  $\text{CaF}_2$ , despite the more complicated experimental conditions. ISRS might be reduced by filtering in the Fourier domain.

## 4.2 Photoinduced *cis-trans* isomerization of azobenzene

### 4.2.1 Background

Beginning with its discovery in 1832 [112], azobenzene (AB) and its derivatives have been in the focus of interest because of their enormous potential for applications and as a model system to study thermal and photochemical *cis-trans* isomerizations [18]. AB is isosteric with stilbene, where the central ethylenic unit is replaced by the azo group. The two isomers, *cis*-AB and *trans*-AB and their photochemical isomerization, were first mentioned by Hartley in 1937 [113]. Figure 4.22 shows the isomerization scheme from *trans*-AB to *cis*-AB and *vice versa* (the wavelengths on the arrows indicate photochemical isomerization). Thermodynamically,

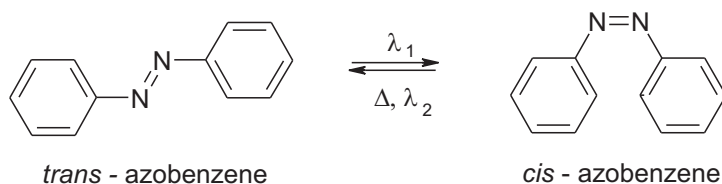


Figure 4.22: *Isomerization scheme of azobenzene.*

*trans*-AB is more stable than *cis*-AB by approximately 90 kJ/mol [114], and *cis*-AB isomerizes thermally to *trans*-AB, as indicated on the arrow. The remarkable property of the photoinduced isomerization reactions is the almost entire lack of by-products, that allows reversible switching over many cycles without the so-called photochemical fatigue. This is the basis for many (industrial) applications. Suitable functionalized AB derivatives have been used to trigger phase transitions in liquid crystal systems, where the *trans*-derivate forms a nematic phase while the *cis*-derivate does not [35, 115]. The change in length and shape from linear for *trans*-AB to bent for *cis*-AB can also be exploited to induce conformational changes in proteins [116, 117, 118], or to evoke phase transitions in emulsions [36]. Further applications include excavator molecules [119, 120] and so-called nano-muscles [20]. Even photoinduced macroscopic motions have been realized in polymeric systems [35, 115].

The photoinduced *cis-trans* isomerization of ABs occurs upon visible and UV irradiation. A spectrum of both isomers in  $\text{CCl}_4$  is shown in Fig. 4.23. Both spectra show a weak band in the visible with a maximum at about 440 nm that corresponds to the forbidden  $S_1(n\pi^*) \leftarrow S_0$  transition, and a much more intensive band in the near UV corresponding to the allowed  $S_2(\pi\pi^*) \leftarrow S_0$  transition with a maximum at approximately 320 nm. ABs were long considered to have no fluorescence due to their extremely low fluorescence quantum yield of  $\Phi \approx 10^{-7}$ . Time-resolved measurements of ABs showed that the isomerization takes place on time scale between few hundred fs to a several ps [31, 38, 121, 122, 123, 124, 125].

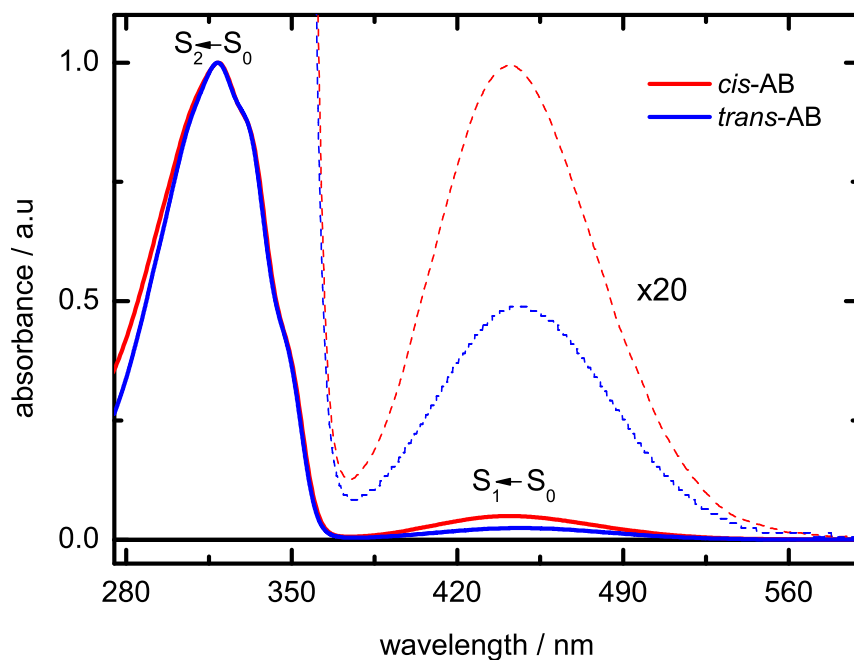


Figure 4.23: UV-VIS absorption spectra of  $0.1 \times 10^{-3}$  mol/l *trans*- and *cis*-AB solutions in  $CCl_4$ .

The photoisomerization yields of ABs violate Kasha's rule [126, 123, 25]. Rau and Lüddecke found that the yields following  $S_1$  excitation are higher than for  $S_2$  excitation by a factor of approximately two, independent from the isomerization direction and also in several solvents (see table 4.2).

Table 4.2: Isomerisation quantum yields of AB [127].

solvent	$\phi_{trans \rightarrow cis}$		$\phi_{cis \rightarrow trans}$	
	$S_1 \leftarrow S_0$	$S_2 \leftarrow S_0$	$S_1 \leftarrow S_0$	$S_2 \leftarrow S_0$
<i>n</i> -hexane	0.25	0.11	0.56	0.27
bromoethane	0.26	0.11	0.58	0.25
ethanol	0.28	0.15	0.51	0.24
water/ethanol(4:1)	0.35	0.21	0.41	0.15

A dual mechanism was suggested to rationalize the results. Accordingly, an inversion on one of the N-atoms of the N-N-double bond *via* an almost planar transition state occurs after excitation to the  $S_1$  state. After excitation to the  $S_2$  state the molecules take a different

route, that involves rotation about the central N-N-bond with a twisted transition state. The two mechanisms are sketched in Fig. 4.24. First *ab-initio* quantum chemical calculations

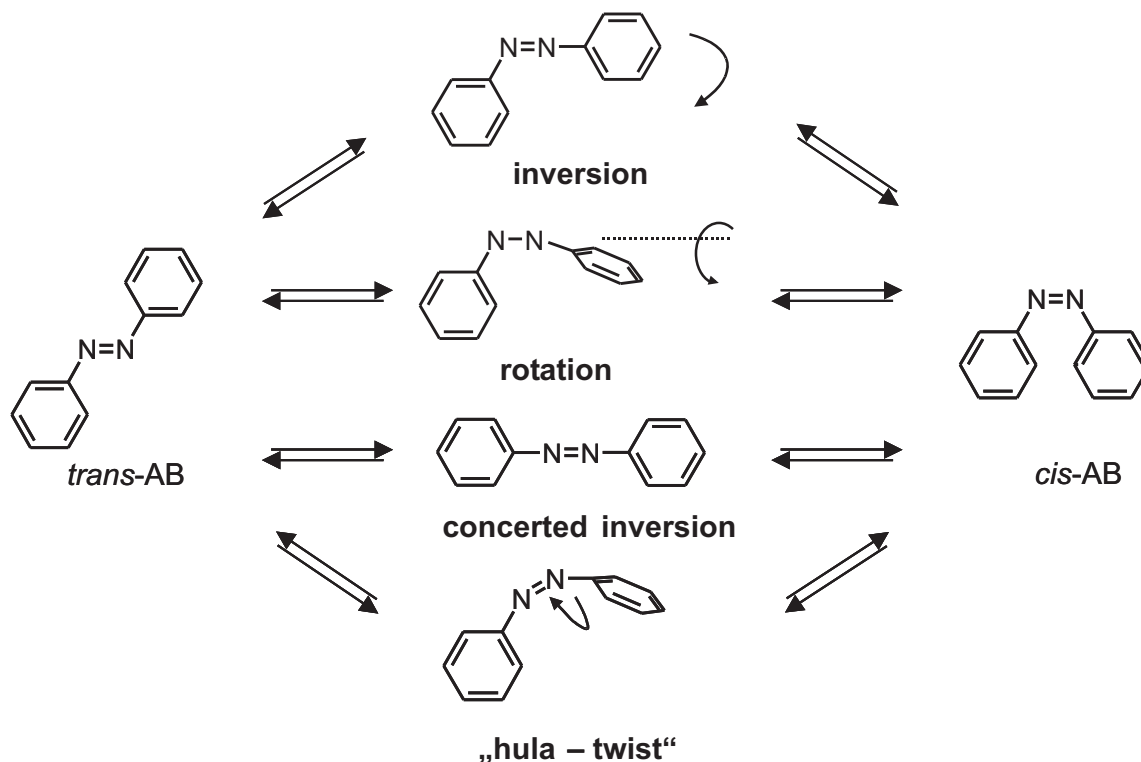


Figure 4.24: *Isomerization mechanism of AB.*

provided assistance for the mechanism [128] and the picture remained unchanged for many years. However, in the last decade, ultrafast spectroscopic experiments as well as numerous theoretical calculations have been performed that have led to a much more complicated and controversially debated picture. One of the most important insights is that pure inversion and pure rotation might not take place at all, and alternative reaction paths such as the concerted inversion, with an almost linear transition state have been suggested [38] (third reaction path in Fig. 4.24). The lowest reaction path shown in Fig. 4.24 is the so-called “hula-twist”, which has been invoked to characterize the isomerization of stilbenes and polyenes [129, 130] and for ABs more recently [125].

Time resolved experimental studies found that the isomerization after excitation into  $S_1$  occurs on a time scale between several hundred fs to a few picoseconds for *trans*-AB, and even faster for *cis*-AB. Most authors favored the inversion pathway, but rotation has also been supported. An important aspect is the possible involvement of a conical intersection (CI) between the  $S_1$  and  $S_0$  surfaces to explain the observed time scales. The most conclusive work probably comes from the study of rotation-restricted AB derivatives [38, 125]. By comparing

the behavior of a rotation-restricted AB and a structurally very similar “open” derivative, Pancur *et al.* [125] found strong evidence to rule out the pure rotational mechanism. To explain the results for excitation into the  $S_2$  state, dual pathways of direct isomerization on the one hand and internal conversion to the  $S_1$  state with a twisted intermediate and subsequent isomerization from  $S_1$  on the other hand have been discussed. Results in favor of efficient relaxation *via* a planar  $S_1$  intermediate have been obtained also [131, 132]. Based on experimental evidence for an optically bright  $S_3$  and  $S_4$  state at similar excitation energies, an extended relaxation scheme was proposed that might resolve these apparent discrepancies [133, 134].

Theoretical calculations have also arrived at different statements, depending on the distinct properties of the calculated potential energy surfaces. There is, however, a general agreement that conical intersections are involved, which have been found for the rotation, inversion and concerted inversion pathways (the “hula-twist” was not explicitly taken into account).

In summary, despite much experimental and theoretical work, the exact mechanism remains unknown, and further experimental work should help to clarify the picture.

#### 4.2.2 Results for *trans-cis* isomerization of azobenzene

The experiments were performed using the chirp-optimized setup of Sec. 3.2.4 at two different excitation wavelengths, with SCG in sapphire. Compressed NOPA pulses centered at 466 nm with 0.45  $\mu\text{J}$  pulse energy and 60 fs (FWHM, from autocorrelation) were used for excitation in the red wing of the  $S_1$  absorption band. The IRF for NOPA excitation typically could be described well by a Gaussian with a FWHM between 80 - 100 fs. Excitation to the overlap region of the  $S_1$  and  $S_2$  bands was performed with pump pulses obtained by SHG of the 775 nm fundamental with an energy of 0.65  $\mu\text{J}$ . The gaussian IRF in this case had a FWHM of 140 - 160 fs.

*Trans*-AB with a purity of 98 % was purchased from Merck and used as provided. *Cis*-AB was obtained from a mixture of both isomers at photochemical equilibrium by column chromatography, with a purity of > 97 % as checked by NMR. All solutions were  $5 \times 10^{-3}$  mol/l using Uvasol, Merck solvents ( $\text{CCl}_4$  and ethanol). Scans for the pure solvents were performed in each case to be able to subtract the solvent contributions to the TA signal. For a typical scan of the AB solutions, the TA signal from up to  $10^4$  laser shots was averaged, and for *trans*-AB at  $\lambda_{\text{pump}} = 466$  nm, five scans were averaged. For *cis*-AB, and for *trans*-AB with excitation at 387 nm only one scan was taken. For each measurement, the time-zero correction was performed as described in Sec. 4.1.1. The solvent signal was subtracted using the time corrected spectra with a correction factor of 0.9 [107].

4.2.2.1 Results after excitation at  $\lambda = 466$  nm

Figure 4.25 shows the time corrected changes in optical density for the pure solvent (part a)) and the *trans*-AB (part b)). Around the zero delay times the signal from pure  $\text{CCl}_4$  in part a) is due to the XPM and shows the features already discussed in the previous section. The maxima of the XPM lie all at the same delay, since the data have been time corrected, *i.e.* the time zero function has been taken into account. At delay times larger than  $\tau \approx 0.2$  ps, only background is observed. The amplitude of the ISRS component is comparable to the noise because of the lowered pump pulse energy.

The signal of the *trans*-AB solution in part b) clearly shows the same XPM features and in addition a broad decaying positive change in transient absorption from  $\lambda = 500$  nm to  $\lambda = 580$  nm of the photoexcited *trans*-AB. Note that the solvent contribution was measured only in the delay range of -0.3 ps to 0.35 ps while the full delay range for the *trans*-AB scan is from -0.3 ps to 13 ps.

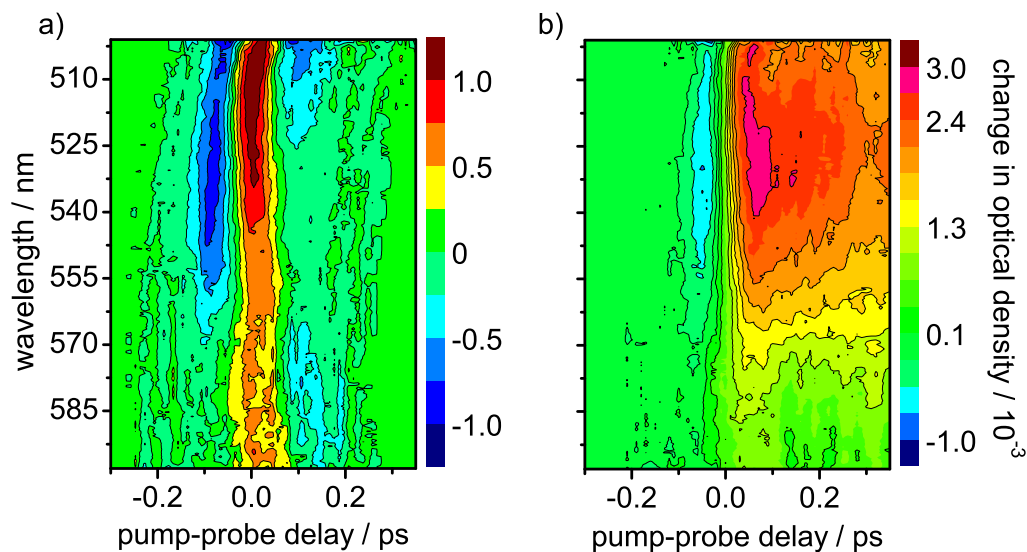


Figure 4.25: Contour plot of the time corrected TA signal after 466 nm excitation of: a) pure  $\text{CCl}_4$  and b)  $5 \times 10^{-3}$  mol/l *trans*-AB in  $\text{CCl}_4$  (XPM not subtracted).

Figure 4.26 shows the subtracted signal, which is now only due to the contributions from the *trans*-AB solute (note the different scales and ranges for the delay times in a) and b)). A positive band of transient absorption can be seen that has its maximum at  $\lambda \approx 520$  nm and decays thereafter. At the maximum delay of  $\tau \approx 13$  ps, the signal has decayed to the background except for the very shortest wavelength.

The effect of the solvent contribution and the subtraction is illustrated in Fig. 4.27, where

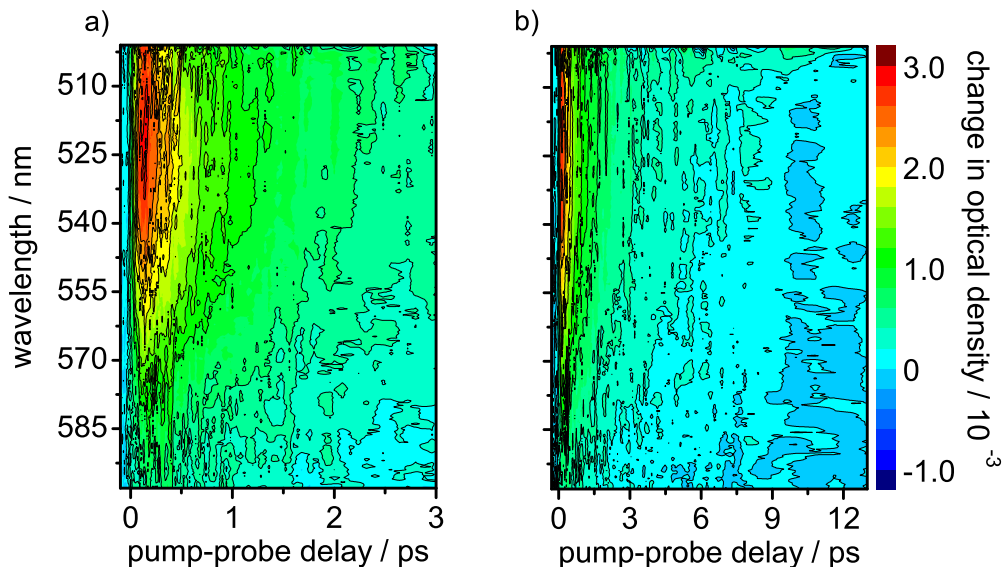


Figure 4.26: Contour plot of the time corrected TA signal of  $5 \times 10^{-3}$  mol/l *trans*-AB after subtraction of the XPM contribution: a) first 3 ps and b) full range up to 13 ps.

cuts at four different wavelengths ( $\lambda = 510$  nm, 535 nm, 550 nm and 560 nm) are shown. The green lines are the TA signal from the pure solvent scan, the blue curves are the raw data from the *trans*-AB solution, the circles are the signal after subtraction, and the red curves are the fits with a sum of two or three exponentials convolved with the IRF according to the Eq. (3.27). For the fits, a non-linear least squares routine based on the Levenberg-Marquardt algorithm [135] was used (see Sec. 3.3.1). As can be seen from Fig. 4.25, the most prominent coherent contribution is the XPM. Since the chosen excitation energy was very low, effects from ISRS have a low amplitude and cannot be distinguished from the noise. The subtracted signal in all four cases does not display residual features from the XPM. The successful time-zero correction is also clearly demonstrated, since all the curves rise at the same delay.

Figures 4.28 and 4.29 show in their upper parts TA data after subtraction at the four selected wavelengths (circles), the fitted temporal profiles as red curves and the first and second decay components (as the blue and green curves, respectively). The third decay component (magenta curve) was only needed for the  $\lambda = 510$  nm case. The inset shows the same for delays up to 2 ps. The lower parts of Figs. 4.28 and 4.29 show the respective residuals as circles. It can be seen that in all cases fits of similar quality could be obtained. The IRF was nearly constant with IRF widths (FWHM)<sup>1</sup> between 80 fs and 101 fs (see Table 4.3). To obtain the best values for the IRF width and the time-zero offset, both values were taken as fixed parameters and

<sup>1</sup>The notation  $\sigma_{IRF}$  will be used for the FWHM values from now on.

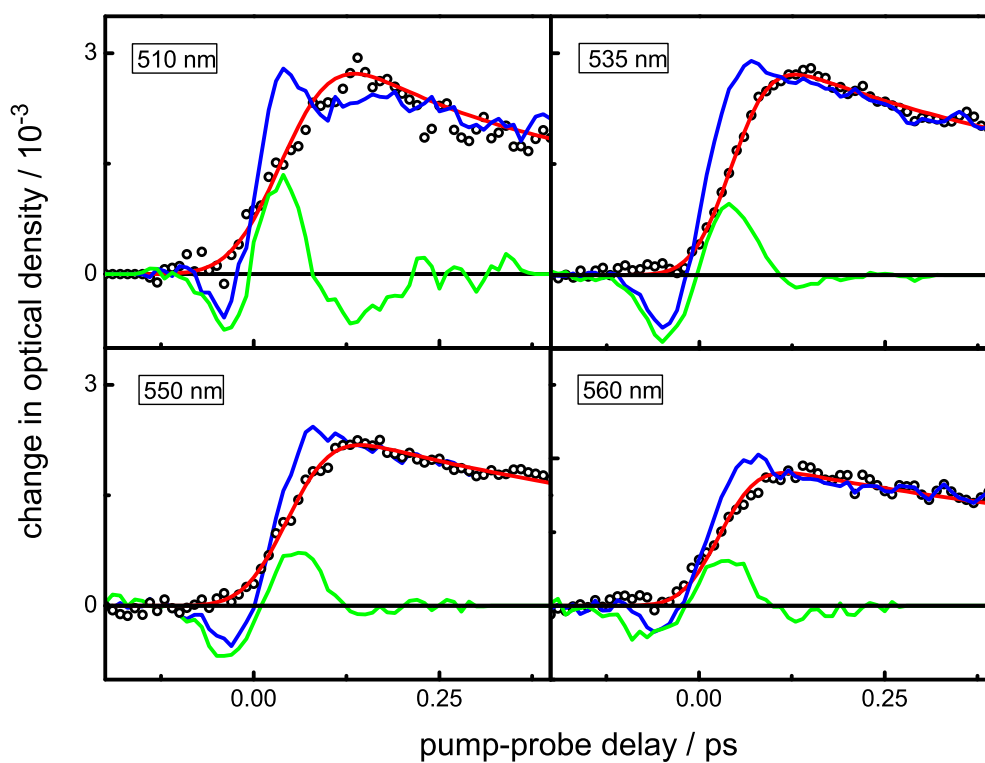


Figure 4.27: TA signal for the first 0.4 ps of *trans*-AB in  $\text{CCl}_4$  after 466 nm excitation at different probe wavelengths. The blue lines represent the measured signal of *trans*-AB in  $\text{CCl}_4$ ; the green lines represent the solvent signal; the circles give the subtracted signal; the red lines are the fits.

fits were performed for an array of values. The  $\chi^2$ -value was taken as criterion to indicate the optimum fit.



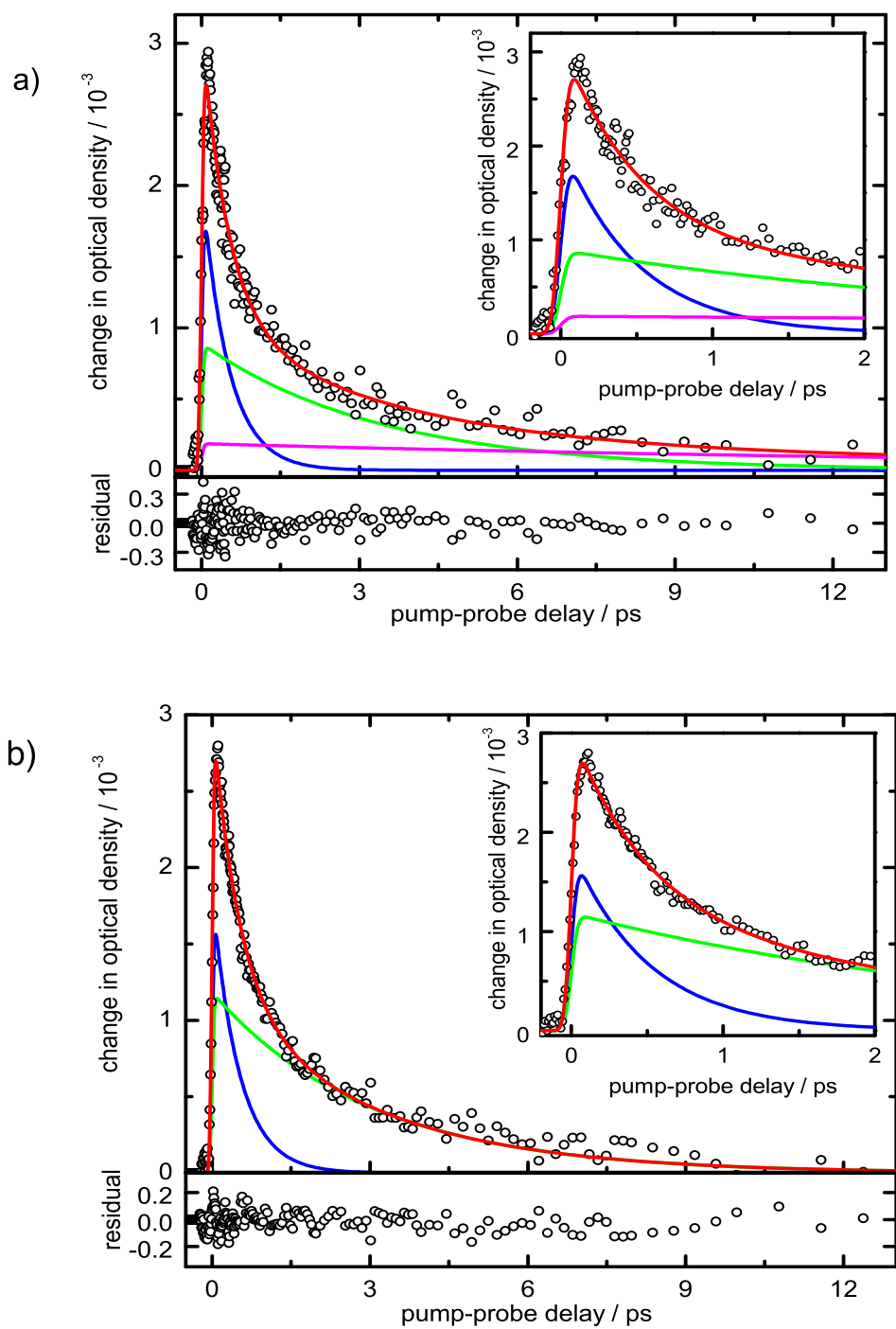


Figure 4.28: TA signal of *trans*-AB in  $\text{CCl}_4$  after 466 nm excitation for  $\lambda_{probe} = 510 \text{ nm}$  (a) and  $\lambda_{probe} = 535 \text{ nm}$  (b).

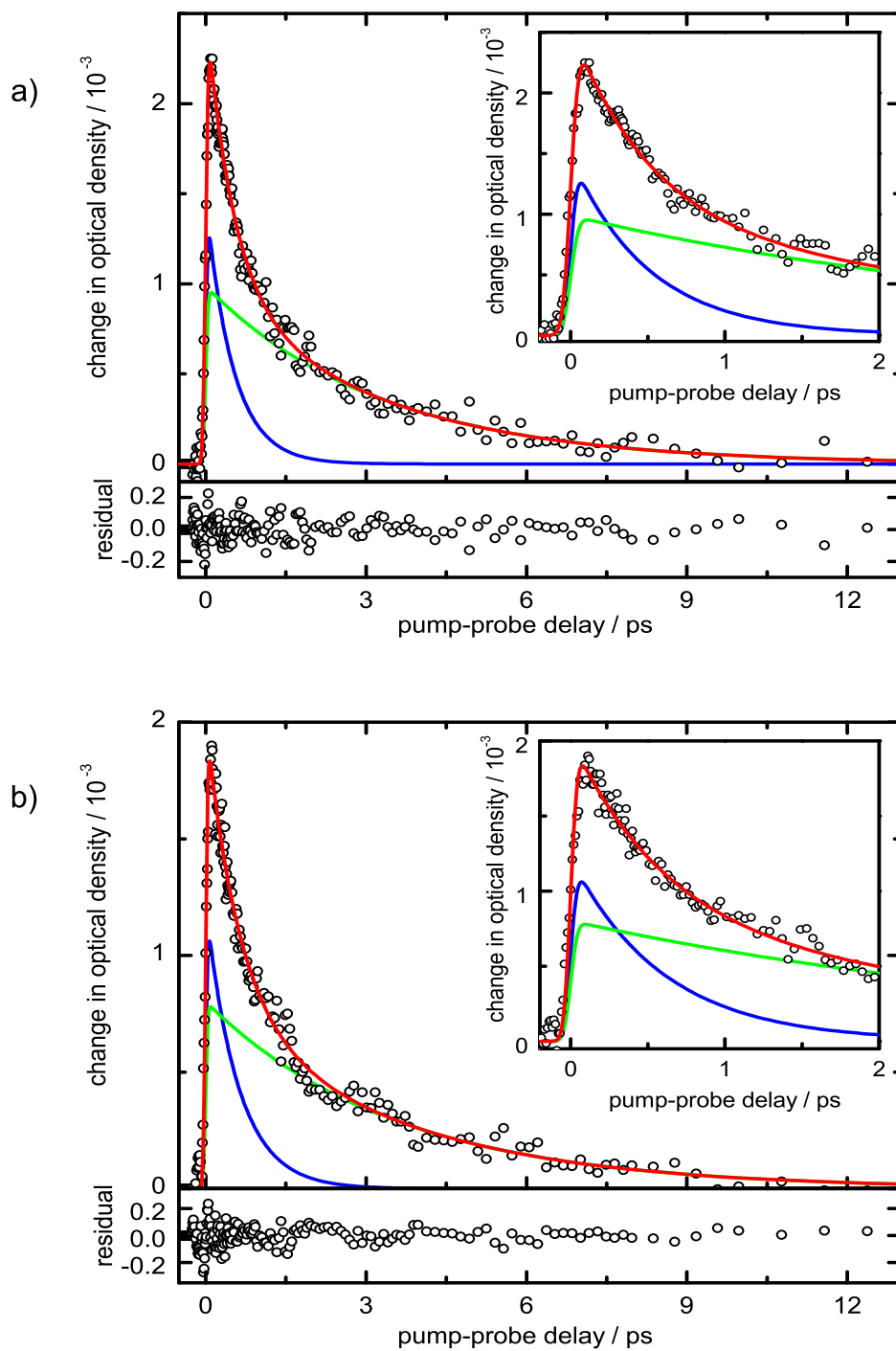


Figure 4.29: TA signal of *trans*-AB in  $\text{CCl}_4$  after 466 nm excitation for  $\lambda_{\text{probe}} = 550 \text{ nm}$  (a) and  $\lambda_{\text{probe}} = 560 \text{ nm}$  (b).

Table 4.3: Fit results of *trans*-AB in CCl<sub>4</sub> after 466 nm excitation

$\lambda_{probe}/\text{nm}$	<i>trans</i> - AB							
	$A_1^a/10^{-3}$	$\tau_1^a/\text{ps}$	$A_2^a/10^{-3}$	$\tau_2^a/\text{ps}$	$A_3^a/10^{-3}$	$\tau_3/\text{ps}$	$\sigma_{IRF}/\text{fs}$	$t_0^b/\text{fs}$
510	1.69 (15)	0.49 (3)	0.90 (1)	3.3 (8)	0.2 (1)	18	101	0
535	1.80 (6)	0.50 (2)	1.10 (6)	2.9 (1)	-	-	80	2
550	1.50 (4)	0.50 (2)	0.90 (4)	3.2 (1)	-	-	96	0
560	1.20 (4)	0.59 (1)	0.80 (4)	3.5 (1)	-	-	81	5

<sup>a</sup>Standard deviation  $2\sigma$  in brackets.

<sup>b</sup>Note that the values of the time-zero offset are constant, but non-zero. This is because only a relative time-zero correction was performed.

Figure 4.30 shows a contour plot of the  $\chi^2$ -values obtained from the fits of the  $\lambda = 535$  nm data as a typical case. The minimum is clearly visible at  $\sigma_{IRF} = 81$  fs and  $t_0 = 2$  fs. The

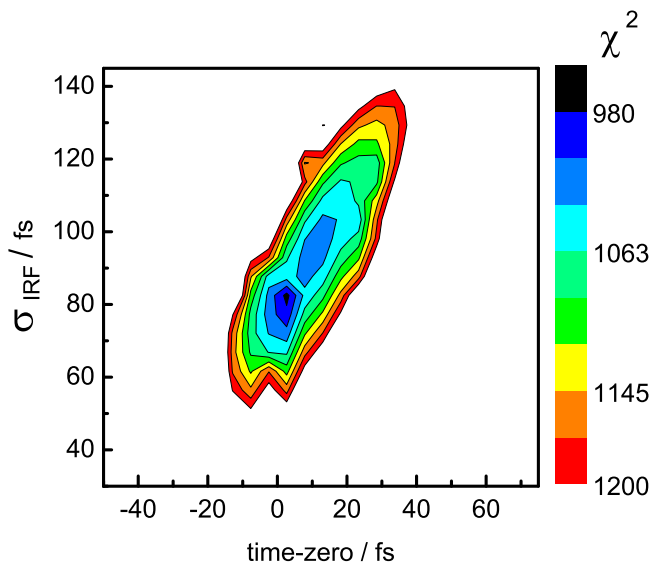


Figure 4.30: Contour plot of the  $\chi^2$ -values for fits of the  $\lambda = 535$  nm data.

fitting parameters that were obtained in this way are listed in Table 4.3. Except for  $\lambda = 510$  nm, all temporal profiles could be described with two exponentials. The third exponential in the case of  $\lambda = 510$  nm has a low amplitude and fits of comparable quality could be obtained for values between  $\tau_3 \approx 8$  ps and  $\tau_3 \approx 20$  ps with only appropriate minor changes of the other parameters. The quoted values of table 4.3 again correspond to the  $\chi^2$ -minimum. The fitted parameters for the two fast decay components are nearly constant. The average decay times are  $\bar{\tau}_1 = 0.52$  ps and  $\bar{\tau}_2 = 3.22$  ps.

4.2.2.2 Results after excitation at  $\lambda = 387$  nm

The transient absorption of *trans*-AB following excitation with 387 nm was measured using ethanol as solvent. Figure 4.31 shows the TA signal after time correction and subtraction of the solvent contributions. Transient absorption occurs over a broad wavelength range from

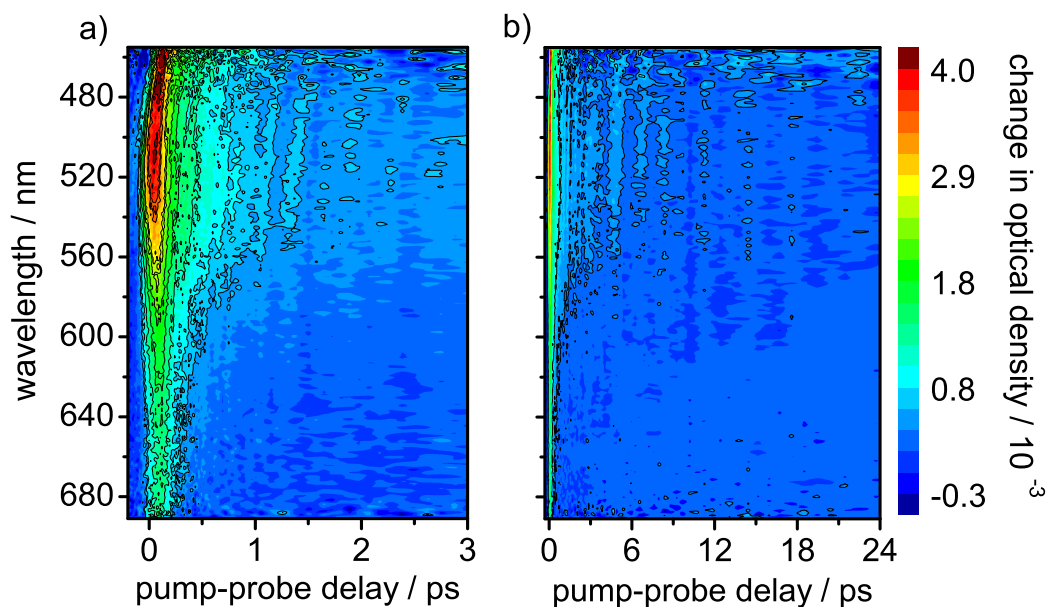


Figure 4.31: Contour plot of the time corrected TA signal of  $5 \times 10^{-3}$  mol/l *trans*-AB after 387 nm excitation (XPM subtracted): a) first 3 ps and b) full range up to 24 ps.

460 nm to 690 nm.

Temporal profiles were analysed at wavelengths of  $\lambda = 500$  nm, 535 nm, 560 nm and 580 nm. Figure 4.32 shows as an example the  $\lambda = 500$  nm case. The upper part of Fig. 4.32 shows the data after subtraction of the solvent contribution as circles and the fitted temporal profile as red line. A satisfying description could only be achieved using three exponential decay components. The blue, green and magenta lines represent the fitted single decay components. The inset shows the raw TA data as blue line, the solvent contribution as orange line and the change in optical density due to the *trans*-AB (circles). The red line is the fit result. The initial rise of the transient absorption is slower than for the 466 nm excitation because of the longer pulse duration of the SHG pump pulses compared to the compressed NOPA pump pulses. The observed difference reflects the increased width of the IRF and not the dynamics of the *trans*-AB molecule. Values of  $\sigma_{IRF}$  between 125 fs and 152 fs were determined from the fits. At the shorter wavelengths, where a fit of the XPM contribution could be performed, a similar value of  $\tau_{cc} = 99$  fs was obtained.

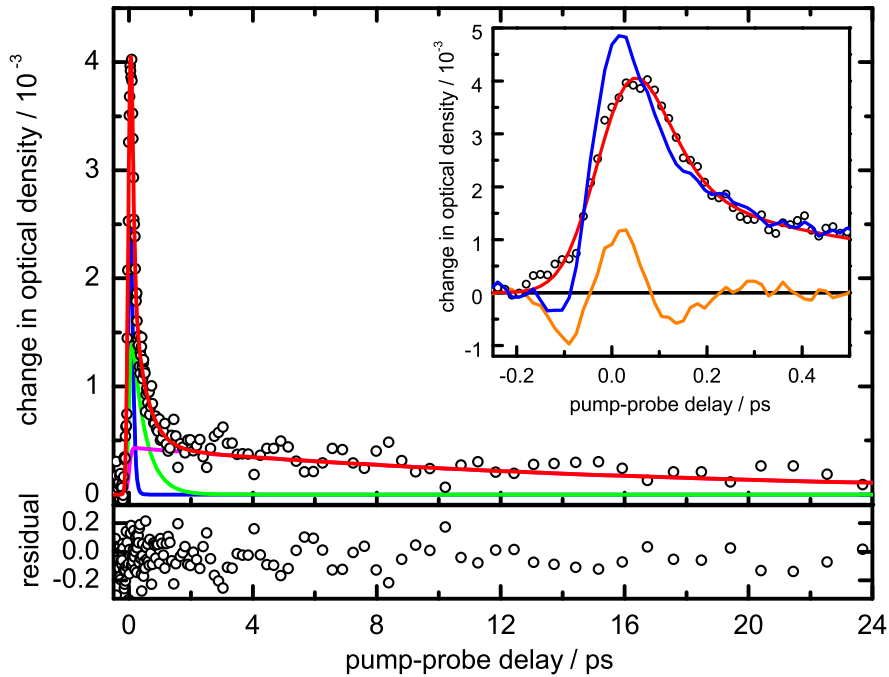


Figure 4.32: TA signal of *trans*-AB at 500 nm after 387 nm excitation: the upper part shows the corrected data together with the fit functions; the inset shows the raw TA data as blue line, the ethanol contribution as orange line, the corrected *trans*-AB signal as circles and the fit as red line.

Table 4.4 shows the parameters that were obtained. All three decay times are approximately constant. The average values for the second and third decay components are  $\overline{\tau_2} = 0.4$  ps and  $\overline{\tau_3} = 13$  ps.

Table 4.4: Fit results of *trans*-AB in ethanol after 387 nm excitation.

$\lambda_{probe}/\text{nm}$	<i>trans</i> - AB						
	$A_1^a/10^{-3}$	$\tau_1^a/\text{ps}$	$A_2^a/10^{-3}$	$\tau_2^a/\text{ps}$	$A_3^a/10^{-3}$	$\tau_3^a/\text{ps}$	$\sigma_{IRF}/\text{fs}$
500	5.9 (3)	0.073 (2)	2.0 (1)	0.41 (3)	0.4 (1)	15 (3)	125
535	4.9 (3)	0.078 (3)	2.1 (1)	0.39 (2)	0.5 (1)	9 (2)	152
550	4.2 (2)	0.080 (8)	1.7 (1)	0.44 (3)	0.4 (1)	12 (2)	140
580	1.9 (2)	0.101 (9)	1.5 (1)	0.38 (3)	0.2 (1)	17 (4)	124

<sup>a</sup>Standard deviation  $2\sigma$  in brackets.

### 4.2.3 Results for *cis-trans* isomerization of azobenzene

For *cis*-AB in  $\text{CCl}_4$ , one scan has been performed for a limited delay range up to 1 ps. Figure 4.33 shows the change in optical density after time correction and subtraction of the solvent contributions. A positive band of transient absorption is observed between  $\lambda = 500$  nm and

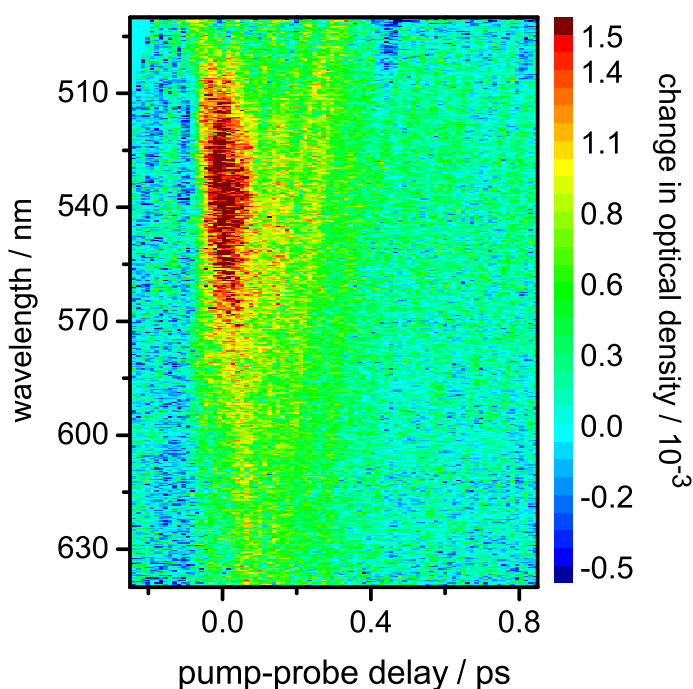


Figure 4.33: Contour plot of time corrected TA signal of  $5 \times 10^{-3}$  mol/l *cis*-AB in  $\text{CCl}_4$  with excitation at 466 nm.

$\lambda = 600$  nm. The maximum of the TA signal occurs at  $\approx 540$  nm. Figure 4.34 shows the temporal profile at  $\lambda_{probe} = 540$  nm. The band decays almost completely within the displayed delay range. As can be seen, the signal-to-noise ratio is too low for a quantitative analysis. Qualitatively, it seems that the TA signal of *cis*-AB decays almost completely within the first ps, *i.e.* faster than *trans*-AB and no slow decay component is apparent.

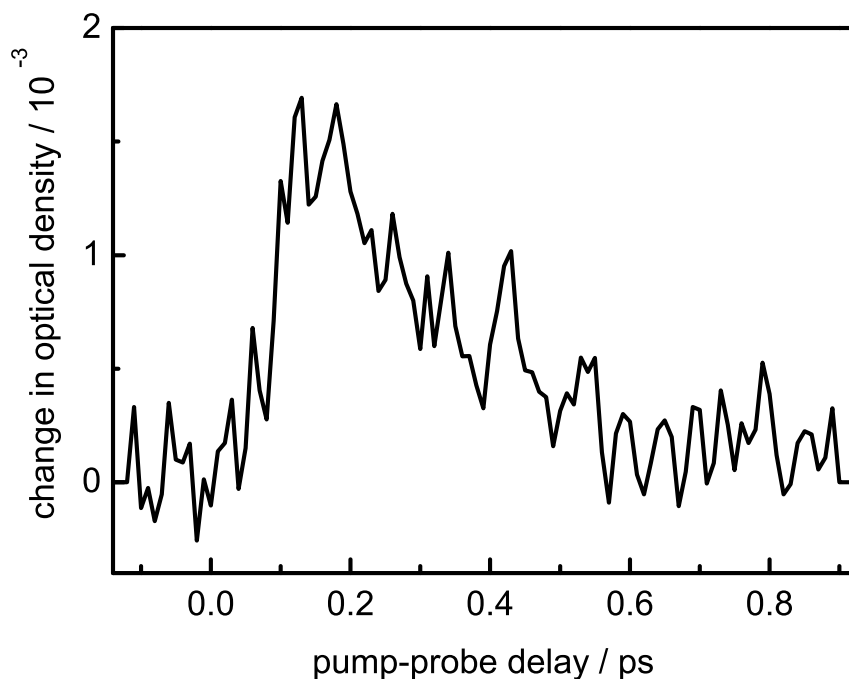


Figure 4.34: Temporal profile of *cis*-AB at  $\lambda_{probe} = 540$  nm after 466 nm excitation. No attempt was made to fit the decay.

#### 4.2.4 Discussion

In the following only the results for the *trans*-AB will be discussed, since the data available for the isomerization of the *cis*-AB are too incomplete for a detailed analysis.

##### 4.2.4.1 Transient absorption time profiles

The observed decay behavior for both excitation wavelengths was different. For 466 nm excitation the time profiles could be described well with two decay components except for the shortest wavelength, where an additional very slow component with a decay time of 18 ps was needed. The decay times of the first and second component were wavelength independent. Average values of  $\bar{\tau}_1 = 0.52$  ps and  $\bar{\tau}_2 = 3.22$  ps were found. The relative amplitude of the slower decay component is lower than for the first, equalling about 50 - 60 %. The amplitude of the third decay component at  $\lambda = 500$  nm is much weaker (only  $\approx 7$  %).

For excitation at  $\lambda = 387$  nm, none of the decays could be described well with only two decay components. All three decay times were not dependent on the detection wavelength within the margin of errors. The first decay component was within the experimental resolution limit

with an average value of  $\overline{\tau}_1 = 0.08$  ps. The slower components had values of  $\overline{\tau}_2 = 0.4$  ps and  $\overline{\tau}_3 = 13$  ps. A comparison of the observed decay constants of this work can be made with published results from Lednev [122], Nägele [121] and Satzger [31, 136]. These results and the present values are summarized in Table 4.5. A direct comparison can be made with

Table 4.5: Results of time-resolved experiments on *trans*-AB and *cis*-AB.

literature		$\lambda_{pump}$ / nm	$\lambda_{probe}$ / nm	$\tau$ / ps
<u><i>trans</i>-AB</u>				
Lednev	[25]	303	370 - 450	0.9 - 1.2 / 13
Lednev	[123]	280	390 - 420	0.8 / 14
Fujino	[126]	267	350 - 650	0.5
Satzger	[136]	266,340	370 - 630	0.13 / 0.42 / 2.9 / 12
Lednev	[25]	390,420	360 - 420	0.6 / 2.6
			500 - 700	0.6 / 2.6
Nägele	[121]	435	459, 563	0.32 / 2.1
Satzger	[31]	480	370 - 580	0.34 / 3 / 12
this work	-	466	500 - 580	0.52 / 3.22 / 18
	-	387	500 - 580	0.08 / 0.4 / 13
<u><i>cis</i>-AB</u>				
Satzger	[136]	266	370 - 630	0.2 / 1.1 / 14
Nägele	[121]	435	max. 360	0.18 / 2 / 20
Satzger	[31]	480	370 - 630	0.1 / 0.9 / 5.6

the results of Ref. [31], which were obtained for excitation at  $\lambda = 480$  nm. Several points are worth noting: First, the third component observed by Satzger *et al.* only contributes to the transient absorption notably at wavelengths less than 520 nm. This is exactly what was observed in this work. Given the low amplitude and corresponding large error bars for this component, the difference of the time constants is not very significant. Second, the decay times of the first and second component clearly correspond to those of Ref. [31]. The slightly larger value (10% by comparison) in both cases can probably be explained by solvent effects. Since the relative amplitude of the decay components are also in accord with literature, the overall agreement of the results with literature can be regarded as excellent.

The results for excitation at  $\lambda = 387$  nm cannot be compared easily to previous published results. The most striking fact is the complete absence of the  $\tau \approx 3$  ps component most commonly observed in the literature [25, 136]. There are only two cases where this component was not relevant: First, the component was found to be very small within a wavelength range from  $\lambda_{probe} = 450 - 600$  nm for excitation of *trans*-AB at 266 nm, and second it was not observed for excitation of *cis*-AB at the same wavelength [136]. At present, it can only be



speculated on the possible causes for the observed discrepancies; however, it seems highly unlikely that experimental errors are responsible, taking into account the excellent agreement of the results at  $\lambda = 466$  nm excitation with literature. The other two components can be related to the respective components found in the literature. While the second decay time agrees very well with published results, the values that were found for the first component are lower than the ones published. However, the quoted time resolutions in the literature are worse than in this work. This might have led the authors to an estimate for the fastest decay constant that is too high and could explain the difference.

#### 4.2.4.2 Interpretation

As the results for the  $S_1(n\pi^*)$  excitation at 466 nm agree very well with those for literature [121, 125, 136], the interpretation of the observed temporal behavior is adopted. Accordingly, the fastest time constant describes the very fast motion of the excited state wave packet out of the Franck-Condon region and the subsequent conversion to the electronic ground states of either the *cis*- or *trans*- isomer. The  $\overline{\tau}_2 = 3.22$  ps component can be interpreted to arise from a fraction of molecules that do not take the direct path and therefore take longer to access the CI. The slowest component can be attributed to the slow relaxation of vibrationally hot molecules in the ground state [31, 121]. This assignment is also in accordance with results from ultrafast infrared and Raman spectroscopy [131, 137].

The interpretation of the results from excitation at 387 nm is not quite as clear. The fastest decay constant for excitation wavelengths between  $\lambda = 266$  nm and  $\lambda = 340$  nm has been interpreted in the literature as ultrafast movement out of Franck-Condon region of the  $S_2(\pi\pi^*)$  state and radiationless relaxation to the  $S_1$  state. It is quite likely that the observed time constant of  $\overline{\tau}_1 = 0.08$  ps can be interpreted in the same way. Therefore, the other components should reflect the dynamics in the  $S_1$  state. Accordingly, the  $\tau = 0.4$  ps component can be interpreted as belonging to direct dynamics towards the  $S_1/S_0$  state conical intersection (CI) and conversion to the ground state, and the  $\tau = 13$  ps component is again cooling of vibrationally hot molecules in the ground state. It is not clear why the  $\tau \approx 3$  ps component after  $\lambda = 387$  nm excitation is absent. Either, the corresponding spectral band has a very low amplitude in the detection wavelength range, or the region of the  $S_1$  surface, where the molecules arrive after conversion from the  $S_2$  state, has a very direct access to the  $S_1/S_0$ -CI.

The results can be summarized as follows:

- On excitation at  $\lambda = 466$  nm the results agree almost quantitatively with those published [31, 121].
- For the  $\lambda = 387$  nm excitation, which is in the overlapping region of the  $S_2$  and  $S_1$  absorption bands, distinct differences with respect to previously observed behavior were found. Although the causes are far from clear, the possible implications can help to extract the picture of the relaxation pathways after  $S_2$  excitation.
- The data demonstrate clearly the ability of the newly built setup to detect very small absorbance changes with high temporal resolution.

### 4.3 Photoinduced isomerization of Fulgides

Fulgides (from the latin word *fulgere* = to shine) are derivatives of bis-methylenesuccinic anhydride, that display a pronounced reversible change of color upon irradiation with light. This behavior, termed photochromism, is basis for their high application potential as optical switches and memory [42, 138, 139]. Fulgides and their photochromism were discovered in 1905 by Stobbe [140]. Figure 4.35 shows the isomerization scheme for the 1-[1-(2,5-dimethyl-3-furyl)ethylidene]-2-isopropylidensuccinanhydrid (from now on, the trade name Aberchrome 540 (ACR 540) will be used).

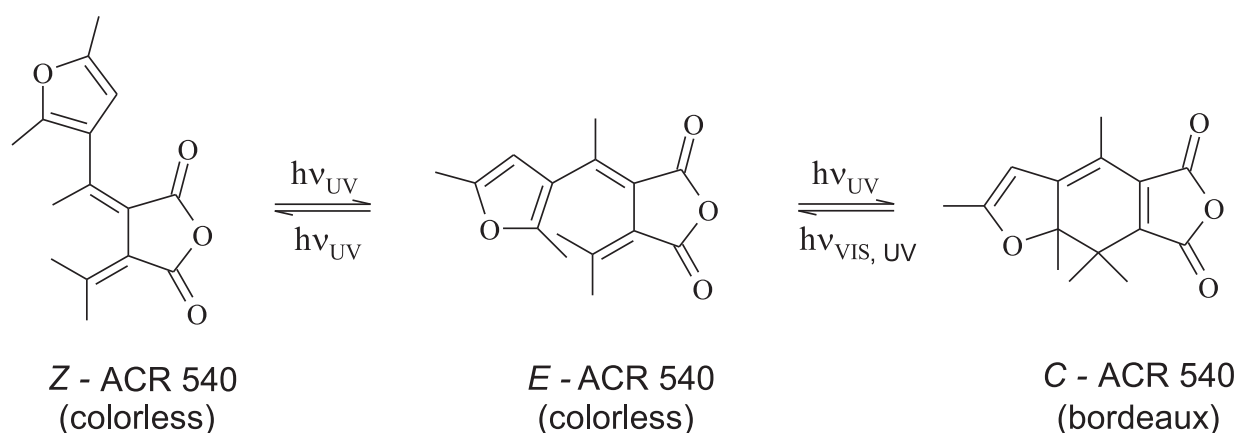


Figure 4.35: Molecular structure and reaction scheme of Aberchrome 540.

The reversible photoinduced ring closure and opening from the *E* to *C* isomer (right half in Fig. 4.35) and back is the basis for the photochromic properties of fulgides. The *E* – *Z* isomerization is the most important competing isomerization process. The exact properties of the fulgides depend on the substituents. With suitable derivatisation, a combination of favorable properties can be achieved which are:

- thermal irreversibility of the ring closure,
- elimination of the thermal *E* – *Z* isomerization and other side reactions,
- high quantum yields and suitable absorption ranges for both isomers,
- low photochemical fatigue.

Aberchrome 540 has already been used successfully in phototypical optical memory devices [44, 141], and as optical switches in biological systems [142] and liquid crystals [143]. Using a molecule in which an anthracene donor, a fulgide switch and a coumarin acceptor were assembled, intramolecular energy transfer modulation could be achieved in liquid solution

[144] and in polymer matrices [145] with high quantum yield and time constants down to 1.2 ps [45, 145].

Knowledge about the details of the reaction mechanism and molecular dynamics, however, is scarce. There is agreement that the photochemical  $E - C$  isomerization proceeds as a conrotatory  $6\pi$  pericyclic ring closure, as expected from the Woodward-Hoffmann rules for a  $\pi-\pi^*$  excitation [146]. However, the precise nature of the excited state is not known. The strong influence of the substituents on the reaction is explained by steric effects. *E.g.* in Aberchrome 540, the thermally allowed disrotatory ring opening is prevented by the substituents at the central methylenic C-atom [147]. X-ray crystallography indeed shows that already the ground state of  $E$ -ACR 540 is highly twisted and non-planar [148, 149]. There are no quantum chemical calculations for the excited states, and calculations for the ground state arrive at different relative stabilities of the isomers.

Experiments using ultrafast techniques have mostly lacked the required temporal resolution. The ultrafast  $E - C$  dynamic has only been resolved in [45, 141] using transient absorption spectroscopy. For excitation of  $E$ -ACR 540 at 392 nm a temporal evolution of the TA signal was found that was explained by a dual mechanism. Accordingly, cyclization can occur on a direct pathway with a time constant of 400 fs, or *via* an intermediate state, which gets populated with a time constant of 700 fs and leads to the  $C$ -isomer on a 100 ps time scale. Similar results were found by Rentzepis *et al.* [150] for a (4-aminophenyl)-fulgimide. Most recent results regarding isomerization in a PMMA matrix [45] however did not find evidence for a dual pathway. No calculations or experiments have been performed for the  $E - Z$  isomerization.

In summary, the knowledge of the nature of the excited states and the underlying molecular dynamics for the  $E - C$  isomerization can be regarded as incomplete, and no information at all is available for the  $E - Z$  isomerization. The results detailed below, although preliminary in nature, are intended to provide additional information.

### 4.3.1 Results on photoisomerization of $Z$ -ACR 540

The experiments were performed with the chirp-optimized setup of Sec. 3.2.4, using SCG in sapphire and SHG pump pulses. A pump energy of  $0.65 \mu\text{J}$  was used. The scattered pump light was reduced by inserting a GG395 filter (Schott) into the beam path behind the cell. The SC was clipped with a cut off filter at 700 nm (Edmund Optics) and a KG1 filter (Schott). The  $Z$ -ACR 540 was purified by column chromatography on silica gel with a 1:6 mixture of diethylether and petrolether as eluent and subsequent recrystallization from *n*-hexane:chloroform (4:1). The purity was checked by thin layer chromatography using the

same eluent, and UV-VIS spectroscopy (UV Probe, Shimadzu Corporation). Typical spectra are shown in Fig. 4.36.

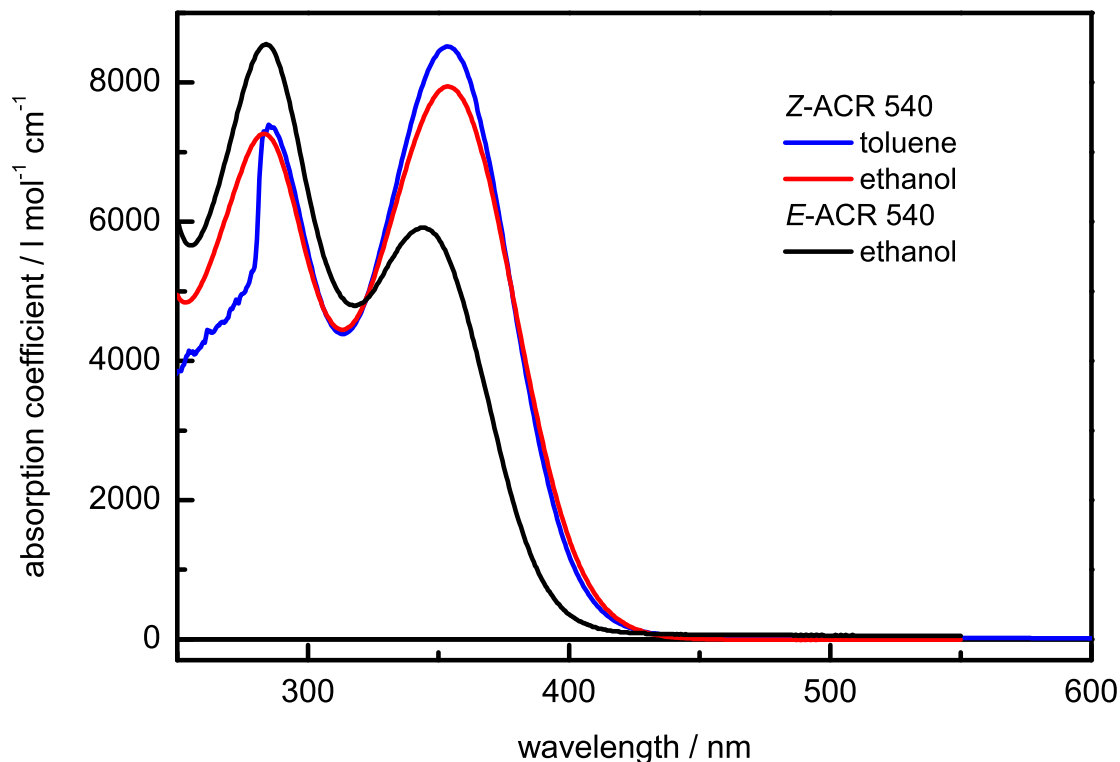


Figure 4.36: UV-VIS absorption spectra of Z- and E-ACR 540 in different solvents for a concentration of  $1 \times 10^{-4}$  mol/l.

Measurements were performed using toluene and ethanol (Uvasol, Merck) as solvents. The concentrations were  $5.3 \times 10^{-4}$  mol/l for the toluene solution and  $1.7 \times 10^{-3}$  mol/l for the ethanol solution. The scans, the time-zero corrections and subtractions of the coherent contribution were performed as for AB. In each case, the presented data are from a single scan.

#### 4.3.1.1 Results for Z-ACR 540 in toluene

Figure 4.37 shows the TA signal of pure toluene after time correction on a scale up to 1.5 ps in part a) and up to 136 ps in part b). A component around zero delay can be seen in part a). This component is only present within the first 0.3 ps and is strongest for the shortest wavelengths in the detection range. An additional component, that shows a slow increase first and thereafter stays nearly constant up to the final delay is clearly visible in part b). The rise

time of  $\tau = 16$  ps of this second component was determined by performing a non-linear least squares fit of the TA signal in the range of 1 ps - 136 ps using the fitting function

$$A = A_0 \left[ 1 - \frac{1}{2} \operatorname{erf} \left( -\frac{t}{\sqrt{2}\sigma_{IRF}} \right) \exp \left( -\frac{t-t_0}{\tau_{rise}} \right) \right]. \quad (4.7)$$

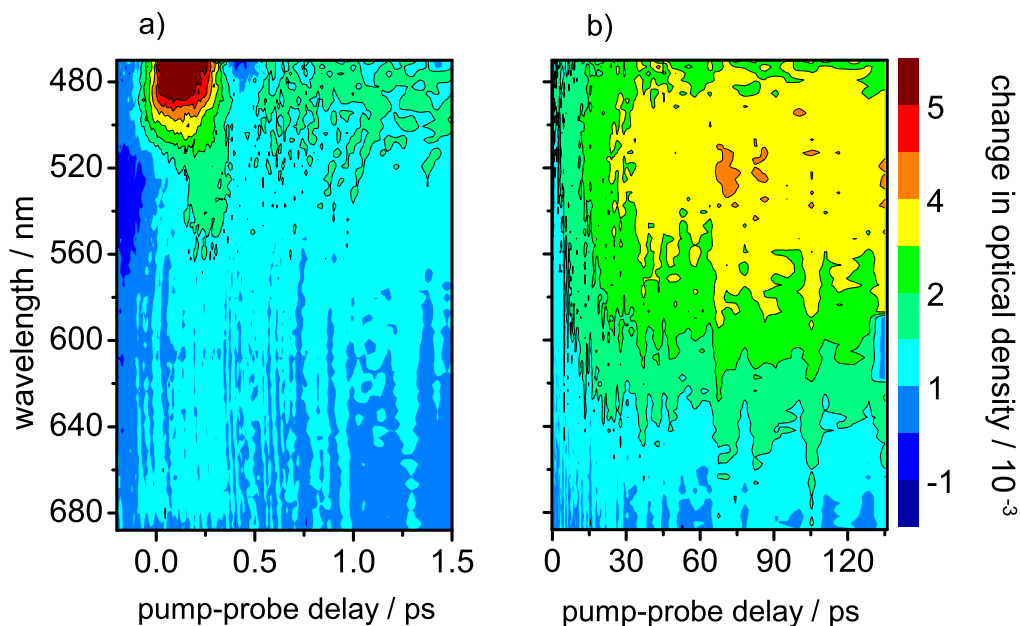


Figure 4.37: Contour plot of the TA signal of pure toluene after 387 nm excitation ( $E_{387} = 0.65 \mu\text{J}$ : a) first 1.5 ps and b) full range (136 ps).

The spectral characteristics of the second component are shown in Fig. 4.38, which shows a cut of the TA data at a delay of  $\tau = 100$  ps. The spectrum is a broad band that extends over the entire wavelength range and has a maximum at about  $\lambda = 540$  nm.

Figure 4.39 shows the time corrected TA signal of the Z-ACR 540 solution after subtraction of the solvent signal. The most important point is that no significant TA contribution occurs after 1 - 1.5 ps (the scale of Fig. 4.39 has been set accordingly). As can be verified from Fig. 4.40, where a cut at  $\lambda_{probe} = 504$  nm is shown, the amplitude of the ACR 540 signal is only 40 % of the total amplitude before subtraction of the solvent component.

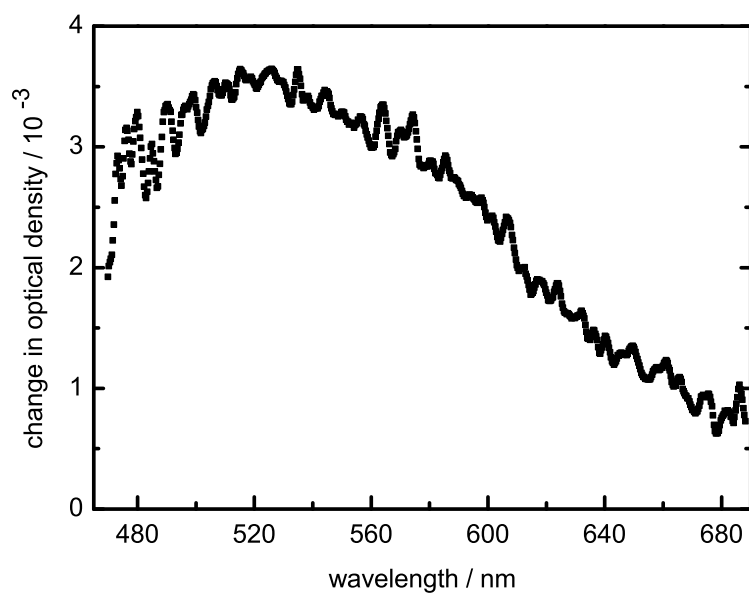


Figure 4.38: TA spectrum of pure toluene after 387 nm excitation at a delay of 100 ps .

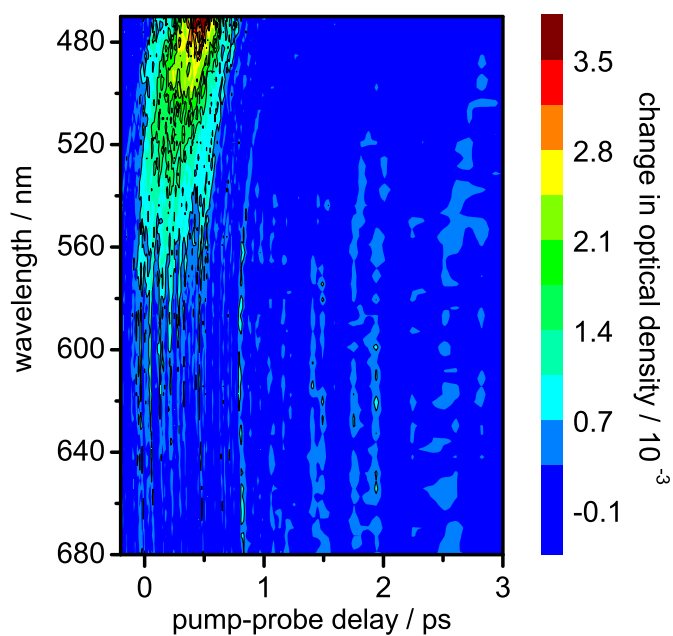


Figure 4.39: Time corrected TA signal of Z-ACR 540 after subtraction of toluene contribution.

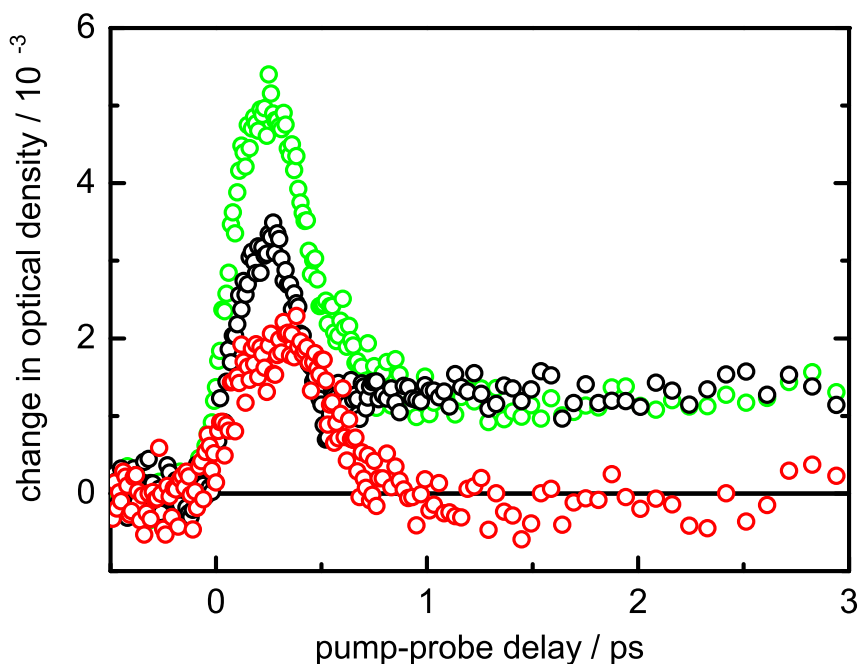


Figure 4.40: TA signal at  $\lambda_{\text{probe}}=504$  nm after 387 nm excitation of: the TA signal of the raw Z-ACR 540 data (green circles), pure toluene (black circles), Z-ACR 540 after subtraction of the toluene contribution (red circles).

The extraordinary large amplitude of the solvent contribution makes its subtraction difficult. Figure 4.40 shows the TA signal at  $\lambda = 504$  nm for the raw data, *i.e.* without the subtraction of the solvent component (green circles), the signal for pure toluene (black circles) and the signal for the Z-ACR 540 solution after subtraction (red circles). As can be seen clearly by comparison of the three signals, the slow component is entirely due to the solvent. In the subtracted signal data, only the fast component remains. In view of the low signal-to-noise amplitude, a quantitative analysis of the Z-ACR 540 was not performed.

In Fig. 4.41 the signal from pure toluene at  $\lambda = 504$  nm is compared to published data. The inset shows Fig. 3 of Ref. [141], which is the TA signal by  $\lambda_{\text{pump}} = 392$  nm excitation of the *E*-isomer of ACR 540. The similarity of both signals is clearly evident.



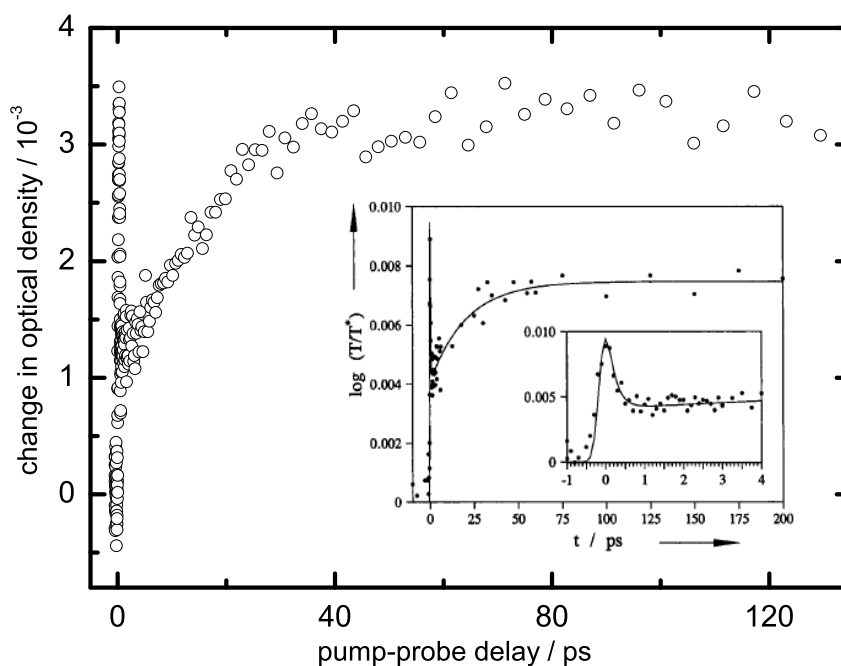


Figure 4.41: Time profile of TA signal for pure toluene at  $\lambda_{probe} = 504$  nm after 387 nm excitation. As inset is shown Fig. 3 of Handschuh et al. and represents the TA signal of E-ACR 540.

#### 4.3.1.2 Results for Z-ACR 540 in ethanol

Ethanol was chosen as a suitable solvent for its absence of any long-time solvent contribution and lower XPM magnitude (see Sec. 4.1.1). Figure 4.42 shows the TA signal of the Z-ACR 540 solution in ethanol after time correction and subtraction of the solvent contribution up to a delay of 4.4 ps. A change in optical density with positive amplitude, which rises immediately at time zero and decays within the first ps, is clearly visible. Figure 4.43 shows a cut at  $\lambda_{probe} = 470$  nm. In the upper part of Fig. 4.43, the circles are the experimental data, and the red line is the fit. The observed TA signal is single exponential with a decay time of  $\tau = 248$  fs and an IRF width of  $\sigma_{IRF} = 132$  fs. The findings from the above are thus confirmed. Further experiments on the same systems (made by A. Petter [109]) with increased detection bandwidth indicate that for shorter wavelengths a much more complex behavior is found. For this reason, no attempt was made to further evaluate the current data.

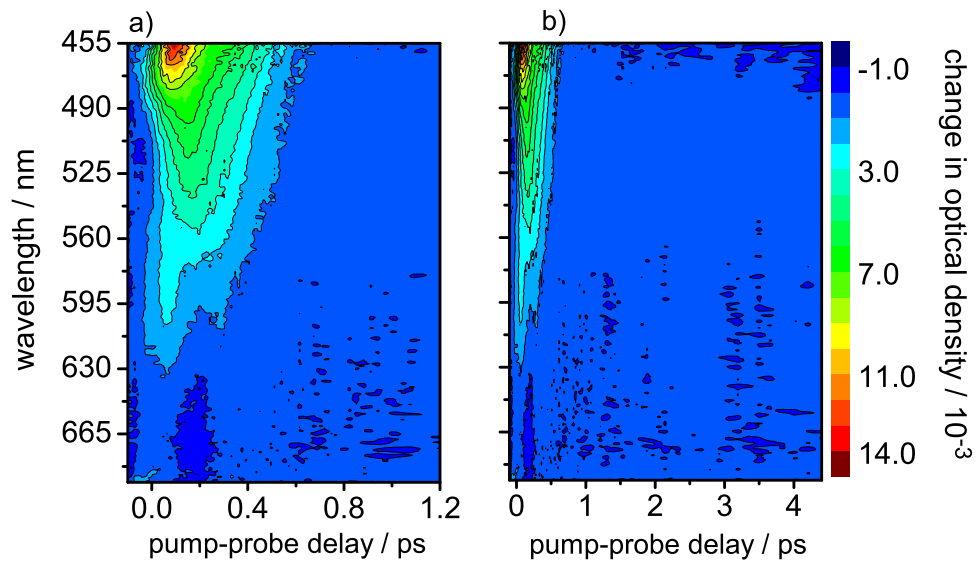


Figure 4.42: Contour plot of the time corrected TA signal of Z-isomer in ethanol after 387 nm excitation ( $E_{387} = 0.65 \mu\text{J}$ , contributions of the ethanol are subtracted): a) first 1.2 ps and b) the complete measured dynamic (4.4 ps).

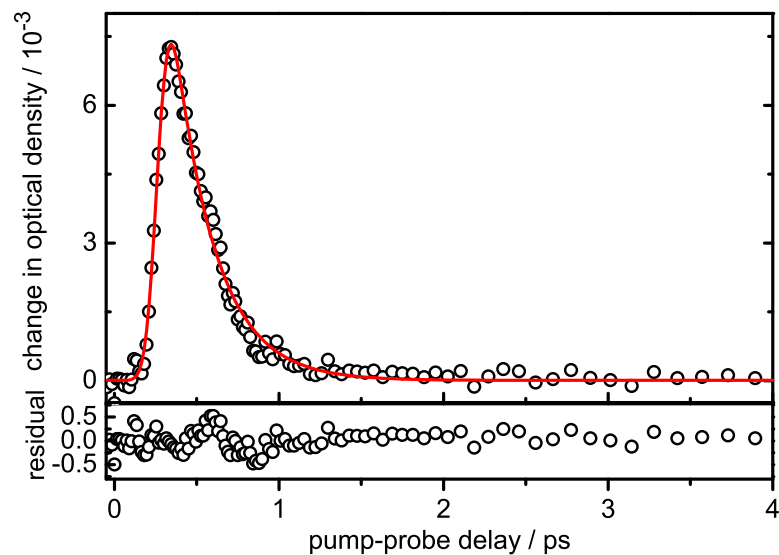


Figure 4.43: Time profile of the TA signal for Z-ACR 540 (circles) at  $\lambda_{\text{probe}} = 470 \text{ nm}$  after 387 nm excitation. The red lines show the fit result. In the lower part the residual is shown.

### 4.3.2 Discussion

In the following, a qualitative discussion of the transient absorption behavior of the photoexcited *Z*-ACR 540 will be given.

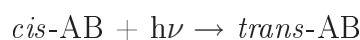
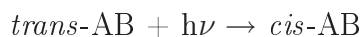
The most striking feature for the experiment performed in toluene were the long time behavior of the transient absorption of the pure solvent with a rise time of  $\tau = 16$  ps. Figure 4.38 shows the component of this spectrum for a delay time of  $t = 100$  ps. This spectrum can be compared with data from Miyasaka *et al.* [151]. Their transient absorption spectrum of toluene obtained from ps-photolysis at 355 nm and taken at  $t = 100$  ps closely resembles the spectrum of Fig. 4.38. The quoted peak position of  $\lambda_{probe} = 555$  nm is close to the peak at  $\lambda_{probe} = 540$  nm for the present data. The difference is not significant considering the flat shape of the absorption band near the maximum. The quoted rise time at the peak wavelength is  $\tau_{rise} = 65 \pm 5$  ps from 10 % to 90 % of the plateau value. Taking into account the 22 ps width of their IRF, this value is in accord with the presented data. It therefore seems reasonably safe to adopt the interpretation of Ref. [151] and to assign this TA component to excimer formation.

An important consequence follows by comparison of the present data of pure toluene with published data from Handschuh *et al.* [141] (see Fig. 4.41). The circles are a cut of the TA signal from pure toluene at  $\lambda_{probe} = 504$  nm, and the inset shows Fig. 3 of Handschuh *et al.* [141]. The comparison suggests that the quoted slow switching time from Ref. [141] and the assumed intermediate excited state actually have to be attributed to toluene. Interestingly, the same authors did observe a distinct different behavior when studying the transient absorption of photoexcited *E*-ACR 540 in a polyatomic environment [45] and concluded that there was only one reaction pathway. This would support further the above hypothesis.

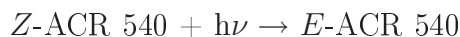
As regards the *Z* – *E* isomerization, no direct comparison can be made with other previous literature data. However, *cis-trans* isomerizations have been found to occur very fast, *e.g.* in ethene [152], azobenzene [18] and rhodopsin [12], and it is believed that conical intersections are involved [153]. It is therefore not surprising that an ultrafast decay time of  $\tau = 248$  fs was found for photoexcited *Z*-ACR 540 in ethanol. The results show clearly that the photoinduced dynamics of fulgides is probably different from what was thought previously. Further experiments should help to clarify the picture which in the light of the presented results seems even more open than ever.

## 5 Summary

In this work the photoinduced isomerization of *trans*- and *cis*-azobenzene according to



and the *cis-trans* photoisomerization of a furylfulgide



were analysed. The photoreactions were investigated using a transient absorption setup. The experiment for the broadband detection of absorbance changes occurring during photoinduced molecular processes was set up. The required sensitivity of less than one part per tenthousand was achieved using a pump-probe-reference scheme with averaging over typically 5000 - 10000 laser pulses. For one pump-probe delay, the change in optical density  $A(\lambda, t)$ , was calculated from the spectral intensities of the probe and reference pulses after passing through the sample.

Either frequency doubled fundamental pulses ( $\lambda = 387$  nm) or compressed pulses from a non-collinear optical parametric amplifier (NOPA) were used as pump pulses. The NOPA pump pulses had a wavelength of  $\lambda_{\text{pump}} = 466$  nm and a typical width of 80 - 100 fs (FWHM). The broadband probe and reference pulses were from supercontinuum generation in sapphire or CaF<sub>2</sub> with a maximum detection range of  $\lambda = 450 - 700$  nm and  $\lambda = 410 - 700$  nm, respectively.

A full characterization of the setup was performed by studying the contributions to the transient absorption signal arising from cross-phase modulation (XPM) in the cell windows alone and for XPM, stimulated Raman amplification (SRA) and impulsive stimulated Raman scattering (ISRS) in the complete cell with hexane, CCl<sub>4</sub> and ethanol solvents. It could be shown that both supercontinua can be described by assuming linearly chirped pulses. Using only reflective optics in the SC beam path a linear chirp rate  $\beta = 1.8 \times 10^{-3}$  fs<sup>-2</sup> and a change of the chirp-dependent time-zero delay of about 120 fs over the full detection range could be achieved.

From the SRA contribution, information about the pulse shape and duration of the pump pulse inside the sample could be gained that helped to find the best setting for the pulse

compression for the NOPA pump pulses. The temporal resolution and sensitivity of the setup also allowed us to determine the Raman modes of  $\text{CCl}_4$  by ISRS. The obtained values of  $224\text{ cm}^{-1}$ ,  $322\text{ cm}^{-1}$ ,  $474\text{ cm}^{-1}$  were in excellent agreement with literature values from spontaneous Raman scattering.

The photoinduced isomerization of *trans*-AB was studied after excitation at  $\lambda_{\text{pump}} = 466\text{ nm}$  (to the  $S_1$  state) and  $\lambda_{\text{pump}} = 387\text{ nm}$  (to the  $S_2$  state) in  $\text{CCl}_4$  and ethanol at room temperature. With the exception of the shortest detection wavelength at  $\lambda = 510\text{ nm}$ , the time profiles for excitation at  $\lambda_{\text{pump}} = 466\text{ nm}$  could be described well with two decay components, that were independent of the detection wavelength. Average values of

$$\bar{\tau}_1 = 0.52(2)\text{ ps and } \bar{\tau}_2 = 3.22(2)\text{ ps}$$

were found. The fastest time constant could be interpreted as very fast motion of the excited state wavepacket out of the Franck-Condon region leading to ultrafast conversion to the  $S_0$  state *via* a CI, while the second component was attributed to molecules that do not take the direct path and access the CI at later time. At  $\lambda = 510\text{ nm}$  a much weaker third component of  $\tau = 18\text{ ps}$  was found, that was assigned to relaxation of vibrational hot molecules in the electronic ground state. The observed results are in excellent agreement with the literature and demonstrate the ability of the new setup to detect very small absorbance changes with high temporal resolution.

For  $\lambda_{\text{pump}} = 387\text{ nm}$ , three decay components with

$$\bar{\tau}_1 = 0.08(5)\text{ ps, } \bar{\tau}_2 = 0.4(3)\text{ ps and } \bar{\tau}_3 = 13(3)\text{ ps}$$

were found. In accordance with literature, the fastest component could be interpreted as ultrafast movement out of the Franck-Condon region and conversion to the  $S_1$  state. The second decay time was attributed to dynamics in the  $S_1$  state towards the  $S_1/S_0$ -CI and the slowest component was again assigned to cooling of vibrational hot molecules in  $S_0$  state. In contrast to literature, no  $\tau \approx 3\text{ ps}$  component was observed. This might have been due to the limited detection wavelength range or specific properties of the molecular dynamics at the chosen excitation wavelength.

The photoinduced isomerization of the furylfulgide *Z*-ACR 540 was studied after excitation at  $\lambda_{\text{pump}} = 387\text{ nm}$  with detection between  $\lambda = 455\text{ nm}$  and  $\lambda = 700\text{ nm}$ . Toluene and ethanol were used as solvents. In toluene a short-lived component only present within the first  $0.3\text{ ps}$  and a long lived second component were found that had a rise time of  $\tau = 16\text{ ps}$  and did not decay within the experimental time range. Based on the temporal properties and spectral characteristics this component was assigned to the photoinduced formation of toluene excimers. The result suggests that the analysis of a similar component in the literature has to

be reconsidered. By contrast, in ethanol only one single fast decay component of  $\tau = 248(2)$  fs was found. The time scale of the process could be interpreted as hint to a possible involvement of a conical intersection in the *cis-trans* isomerization of furylfulgides.

# Bibliography

- [1] S. Arrhenius, *Rev. Gen. Sci. Pur. Appl.*, 1911, **22**, 266–275.
- [2] T. H. Maiman, *Nature*, 1960, **187**, 493.
- [3] R. W. Hellwarth, *Bull. Am. Phys. Soc.*, 1961, **6**, 414.
- [4] C. Rullière, *Femtosecond Laser Pulses, Principles and Experiments*, Springer-Verlag, 1 ed., 1998.
- [5] P. M. W. French, *Rep. Prog. Phys.*, 1995, **58**, 169–267.
- [6] S. L. Shapiro, *Ultrashort Light Pulses*, Springer-Verlag, Berlin, Heidelberg, New York, 1977.
- [7] R. L. Fork, C. Brito, C. H. P. C. Becker, and C. V. Shank, *Opt. Lett.*, 1987, **12**, 483–485.
- [8] R. Kienberger, E. Goulielmakis, M. Uiberacker, A. Baltuska, V. Yakovlev, F. Bammer, A. Scrinzi, T. Westerwalbesloh, U. Kleineberg, U. Heinzmann, M. Drescher, and F. Krausz, *Nature*, 2004, **427**, 817–821.
- [9] A. H. Zewail, *J. Phys. Chem. A*, 2000, **104**, 5660–5694.
- [10] A. Douhal and J. Santamaria, *Femtochemistry and Femtobiology: Ultrafast Dynamics in Ultrafast Molecular Science*, World Scientific, Singapur, 1 ed., 2002.
- [11] R. Jiminez and G. R. Fleming In *Advances in Photosynthesis*, pp. 63–73, 1996.
- [12] R. W. Schoenlein, L. A. Peteanu, Q. Wang, R. A. Mathies, and C. V. Shank, *Science*, 1991, **254**, 412.
- [13] F. Gai, K. C. Hasson, and P. A. Anfinrud, *Springer Series in Chemical Physics*, 1996, **62**(Ultrafast Phenomena X), 353–354.

- [14] S. Hahn and G. Stock, *Chem. Phys.*, 2000, **259**, 297–312.
- [15] P. R. Callis, *Annu. Rev. Phys. Chem.*, 1983, **34**, 329–357.
- [16] C. E. Crespo-Hernández, B. Cohen, P. M. Hare, and B. Kohler, *Chem. Rev.*, 2004, **104**, 1977–2019.
- [17] T. Pancur, N. K. Schwalb, F. Renth, and F. Temps, *Chemical Physics*, 2005, **313**, 199–212.
- [18] H. Rau in *Photochromism: Molecules and Systems*, ed. H. A. Dürr and H. Bouas-Laurent; Elsevier, 1990; book chapter 4, pp. 165–192.
- [19] B. L. Feringa, *Molecular Switches*, WILEY-VCH, 2001.
- [20] Y. Yu, M. Nakano, and T. Ikeda, *Nature*, 2003, **425**, 145.
- [21] E. W. G. Diau, J. Casanova, J. D. Roberts, and A. H. Zewail, *Proc. Natl. Acad. Sci. USA*, 2000, **97**, 1376–1379.
- [22] W. Fuss, K. K. Pushpa, W. Rettig, W. E. Schmid, and S. A. Trushin, *Photochem. Photobiol. Sci.*, 2002, **1**, 255–262.
- [23] S. Takeuchi and T. Tahara, *Chem. Phys. Lett.*, 1997, **277**, 340–346.
- [24] T. Gustavsson, L. Cassara, V. Gulbinas, G. G. Gurzadyan, J. C. Mialocq, S. Pommeret, M. Sorgius, and P. van der Meulen, *J. Phys. Chem. A*, 1998, **102**, 4229–4245.
- [25] I. K. Lednev, T.-Q. Ye, R. E. Hester, and J. N. Moore, *J. Chem. Phys.*, 1996, **100**, 13338–13341.
- [26] S. A. Kovalenko, N. Eilers-König, T. A. Senyushkina, and N. P. Ernsting, *J. Phys. Chem. A*, 2001, **105**, 4834–4843.
- [27] R. A. Alfano, *The Supercontinuum Laser Source*, 1989.
- [28] V. P. Kandidov, O. G. Kosareva, I. S. Golubtsov, W. Liu, A. Becker, N. Azozbek, C. M. Bowden, and S. L. Chin, *Appl. Phys. B*, 2003, **77**, 149–165.
- [29] J.-M. L. Pecourt, J. Peon, and B. Kohler, *J. Am. Chem. Soc.*, 2001, **123**, 10370–10378.
- [30] J. Peon, J. D. Hoerner, and B. Kohler, *Liquid Dynamics: Experiment, Simulation, and Theory*, 2002, **820**, 122–135.



- [31] H. Satzger, S. Sporlein, C. Root, J. Wachtveitl, W. Zinth, and P. Gilch, *Chem. Phys. Lett.*, 2003, **372**, 216–223.
- [32] M. Klessinger and J. Michl, *Excited states and photochemistry of organic molecules*, VCH Publisher, Inc., 1995.
- [33] I. Willner, S. Rubin, and A. Riklin, *J. Am. Chem. Soc.*, 1991, **113**, 3321–3325.
- [34] J. R. Kumita, O. S. Smart, and G. A. Woolley, *Proc. Natl. Acad. Sci.*, 2000, **97**, 3803.
- [35] T. Ikeda and O. Tsutsumi, *Science*, 1995, **268**, 1873–1875.
- [36] I. Porcar, P. Perrin, and C. Tribet, *Langmuir*, 2001, **17**, 6905–6909.
- [37] T. Hugel, N. B. Holland, A. Cattani, L. Moroder, M. Seitz, and H. E. Gaub, *Science*, 2002, **296**(5570), 1103–1106.
- [38] E. W. G. Diau, *J. Phys. Chem. A*, 2004, **108**, 950–956.
- [39] A. Cembran, F. Bernadi, M. Garavelli, L. Gagliardi, and G. Orlandi, *J. Am. Chem. Soc.*, 2004, **126**, 3234–3243.
- [40] H. G. Heller, *IEE Proceedings, Part I: Solid-State and Electron Devices*, 1983, **130**, 209–211.
- [41] H. G. Heller, K. Koh, C. Elliot, and J. Whittall, *Molecular Crystals and Liquid Crystals Science and Technology, Section A: Molecular Crystals and Liquid Crystals*, 1994, **246**, 79–86.
- [42] Y. Yokoyama, *Chem. Rev.*, 2000, **100**, 1717–1739.
- [43] M. Seibold, M. Handschuh, H. Port, and H. C. Wolf, *J. Lumin.*, 1997, **72-74**, 454–456.
- [44] Y. C. Liang, A. S. Dvornikov, and P. M. Rentzepis, *Proc. Natl. Acad. Sci. USA*, 2003, **100**, 8109–8112.
- [45] H. Port, P. Gärtner, M. Hennrich, I. Ramsteiner, and T. Schöck, *Mol. Cryst. Liq. Cryst.*, 2005, **430**, 15–21.
- [46] F. Waiblinger, J. Keck, M. Stein, A. P. Fluegge, H. E. A. Kramer, and D. Leppard, *J. Phys. Chem. A*, 2000, **104**, 1100–1106.
- [47] C. Chudoba, E. Riedle, M. Pfeiffer, and T. Elsaesser, *Chem. Phys. Lett.*, 1996, **263**, 622–628.

- [48] S. Lochbrunner, A. J. Wurzer, and E. Riedle, *J. Phys. Chem. A*, 2003, **107**, 10580–10590.
- [49] T. Elsaesser, *Femtosecond Chem.*, 1995, **2**, 563–579.
- [50] W. Fuss, P. Hering, K. L. Kompa, S. Lochbrunner, T. Schikarski, W. E. Schmid, and S. A. Trushin, *Berichte der Bunsen-Gesellschaft*, 1997, **101**, 500–509.
- [51] M. Garavelli, P. Celani, F. Bernardi, M. A. Robb, and M. Olivucci, *J. Am. Chem. Soc.*, 1997, **119**, 11487–11494.
- [52] S. A. Trushin, W. Fuss, W. E. Schmid, and K. L. Kompa, *J. Phys. Chem. A*, 1998, **102**, 4129–4137.
- [53] W. Fuss, T. Schikarski, W. E. Schmid, S. Trushin, and K. L. Kompa, *Chem. Phys. Lett.*, 1996, **262**, 675–682.
- [54] A. J. Wurzer, T. Wilhelm, J. Piel, and E. Riedle, *Chem. Phys. Lett.*, 1999, **299**, 296–302.
- [55] E. W. G. Diau, C. Kotting, T. I. Solling, and A. H. Zewail, *Chem. Phys. Chem.*, 2002, **3**, 57–78.
- [56] P. Cattaneo and M. Persico, *Theoretical Chemistry Accounts*, 2000, **103**, 390–398.
- [57] H. Niedrig in *Lehrbuch der Experimentalphysik*, Vol. 3; Walter de Gruyter, Berlin, New York, 9 ed., 1993.
- [58] J. C. Diels and W. Rudolph, *Ultrashort Laser Pulse Phenomena*, Academic Press, San Diego, 1 ed., 1996.
- [59] W. Kaiser, *Ultrashort Laser Pulses*, Springer, 1993.
- [60] J. M. Hopkins and W. Sibbett, *Spektrum der Wissenschaft*, 2000, pp. 66–73.
- [61] P. Maine, D. Strickland, P. Bado, M. Pesset, and G. Mourou, *IEEE J. Quantum Electron.*, 1988, **QE-24**, 398–404.
- [62] K. L. Sala, G. A. Kenney-Wallace, and G. E. Hall, *IEEE J. Quantum Electron.*, 1980, **16**, 990–996.
- [63] R. Trebino, K. W. Delong, D. N. Fittinghoff, J. N. Sweetser, M. A. Krumbugel, B. A. Richman, and D. J. Kane, *Rev. Sci. Instrum.*, 1997, **68**, 3277–3295.
- [64] L. Gallmann, D. H. Sutter, N. Matuschek, G. Steinmeyer, C. Iaconis, and I. A. Walmsley, *Opt. Lett.*, 1999, **24**, 1314–1316.

- [65] L. Gallmann, G. Steinmeyer, D. H. Sutter, T. Rupp, C. Iaconis, I. A. Walmsley, and U. Keller, *Opt. Lett.*, 2001, **26**, 96–98.
- [66] T. M. Shuman, M. E. Anderson, J. Bromage, C. Iaconis, L. Waxer, and I. A. Walmsley, *Optics Express*, 1999, **5**, 134–143.
- [67] T. Elsaesser, *Ultrafast Phenomena*, Springer, 1998.
- [68] T. Kobayashi and A. Shirakawa, *IEICE Trans. Electron.*, 1998, **E81-C**, 246–253.
- [69] V. G. Dmitriev, G. G. Gurzadyan, and D. N. Nikogosyan, *Handbook of Nonlinear Optical Crystals*, Springer-Verlag, 1 ed., 1991.
- [70] E. Riedle, M. Beutter, S. Lochbrunner, J. Piel, S. Schenkl, S. Sporlein, and W. Zinth, *Appl. Phys. B*, 2000, **71**, 457–465.
- [71] D. K. Negus, M. K. Reed, and M. K. Steiner-Shepard, *Opt. Lett.*, 1994, **19**, 1855–1857.
- [72] G. Cerullo, M. Nisoli, and S. de Silvestri, *Appl. Phys. Lett.*, 1997, **71**, 3616–3618.
- [73] A. Shirakawa, I. Sakane, M. Takasaka, and T. Kobayashi, *Appl. Phys. Lett.*, 1999, **74**, 2268–2270.
- [74] K. Kato, *IEEE J. Quantum Electron.*, 1986, **QE-22**, 1013–1014.
- [75] G. M. Gale, M. Cavallari, T. J. Driscoll, and F. Hache, *Opt. Lett.*, 1995, **20**, 1562–1564.
- [76] G. M. Gale, M. Cavallari, and F. Hache, *J. Opt. Soc. Am. B*, 1998, **15**, 702–714.
- [77] T. Kobayashi and A. Shirakawa, *Appl. Phys. B*, 2000, **70**, 239–246.
- [78] G. Cerullo and S. D. Silvestria, *Rev. Sci. Instr.*, 2003, **74**, 1–18.
- [79] I. Ross, P. Matousek, G. New, and K. Osvay, *J. Opt. Soc. Am. B*, 2002, **19**, 2945.
- [80] J. Limpert, C. Aguergaray, S. Montant, I. M.-H. S. Petit, D. Descamps, , E. Cormier, and F. Salin, *Optics Express*, 2005, **13**, 7386.
- [81] R. L. Fork, O. E. Martinez, and J. P. Gordon, *Opt. Lett.*, 1984, **9**, 150–152.
- [82] R. R. Alfano and S. L. Shapiro, *Phys. Rev. Lett.*, 1970, **24**, 584–587.
- [83] R. L. Fork, C. V. Shank, and R. T. Yen, *Appl. Phys. Lett.*, 1982, **41**, 223–225.
- [84] P. Corkum and C. Rolland, *Physical Review Letters*, 1986, **57**, 2268–2271.

- [85] R. L. Fork, C. V. Shank, C. Hirlimann, R. Yen, and W. J. Tomlinson, *Opt. Lett.*, 1983, **8**, 1–3.
- [86] J. H. Marburger, *Prog. Quantum Electron*, 1975, **4**, 35.
- [87] Y. R. Shen, *Prog. Quantum Electron*, 1975, **4**, 1.
- [88] N. Bloembergen, *Opt. Commun.*, 1973, **8**, 285.
- [89] A. Zheltikov, *Appl. Phys. B: Lasers and Optics*, 2003, **77**, 143–147.
- [90] B.R.Suydam, *Self-steeping of optical pulses*, 1989.
- [91] G. Yang and Y. R. Shen, *Opt. Lett.*, 1984, **9**, 510–512.
- [92] A. Brodeur and S. L. Chin, *J. Opt. Soc. Am. B*, 1999, **16**, 637–650.
- [93] I. Golub, *Opt. Lett.*, 1990, **15**, 305.
- [94] B. A. Horn, J. L. Herek, and A. H. Zewail, *J. Am. Chem. Soc.*, 1996, **118**, 8755–8756.
- [95] H. Lippert, H. H. Ritze, I. V. Hertel, and W. Radloff, *Chem. Phys. Chem.*, 2004, **5**, 1423–1427.
- [96] H. R. Schanz *Femtosecond Broadband-Fluorescence Upconversion* PhD thesis, Humboldt-Universität zu Berlin, 2002.
- [97] S. Mukamel, *Principles of Nonlinear Optics and Spectroscopy*, Oxford University Press, New York, 1995.
- [98] E. P. Ippen, C. V. Shank, and A. Dienes, *Appl. Phys. Lett.*, 1972, **21**, 348.
- [99] T. Pancur *Untersuchung der Isomerisierungsdynamik von Azobenzolen und der strahlungslosen Desaktivierung von Nukleobasen mit Hilfe der Femtosekunden-Fluoreszenzspektroskopie* PhD thesis, Kiel, 2004.
- [100] E. B. Treacy, *IEEE J. Quantum Electron.*, 1969, **QE-5**, 454–458.
- [101] G. Cheriaux, P. Rousseau, F. Salin, J. P. Chambaret, B. Walker, and L. F. Dimauro, *Opt. Lett.*, 1996, **21**, 414–416.
- [102] F. Renth unpublished results.
- [103] S. A. Kovalenko, A. L. Dobryakov, J. Ruthmann, and N. P. Ernstring, *Phys. Rev. A*, 1999, **59**, 2369–2384.

- [104] A. L. Dobryakov, S. A. Kovalenko, and N. P. Ernsting, *J. Chem. Phys.*, 2003, **119**, 988–1002.
- [105] K. Ekvall, P. van der Meulen, C. Dhollande, L.-E. Berg, S. Pommeret, R. Naskrecki, and J.-C. Mialocq, *J. Appl. Phys.*, 2000, **87**, 2340–2352.
- [106] K. Ekvall *Time Resolved Laser Spectroscopy Non-linear polarisation studies in condensed phase and Lifetime studies of alkaline earth hydrides* PhD thesis, Stockholm, 2000.
- [107] M. Lorenc, M. Ziolk, R. Naskrecki, J. Karolczak, J. Kubicki, and A. Maciejewski, *Appl. Phys. B*, 2002, **74**, 19.
- [108] M. Ziolk, M. Lorenc, and R. Naskrecki, *Appl. Phys. B*, 2001, **72**, 843.
- [109] A. Petter, *Diploma Thesis, Kiel*, 2005.
- [110] W. Zinth and W. Kaiser, *Opt. Commun.*, 1980, **32**, 507.
- [111] D. W. McCamant, P. Kukura, and R. A. Mathies, *Rev. Sci. Inst.*, 2004, **75**, 4971–4980.
- [112] J. Falbe. and M. Regnitz, *Römpe Chemie Lexikon*, Thieme Verlag Stuttgart, 1995.
- [113] G. S. Hartley, *Nature*, 1937, **140**, 281.
- [114] H. Rau, *Angew. Chem.*, 1973, **6**, 248–258.
- [115] A. Natansohn and P. Rochon, *Chem. Rev.*, 2002, **102**, 4139–4175.
- [116] S. Spörlein, H. Carstens, H. Satzger, C. Renner, R. Behrendt, L. Moroder, P. Tavan, W. Zinth, and J. Wachtveitl, *Proc. Natl. Acad. Sci. USA*, 2002, **99**, 7998–8002.
- [117] D. M. Junge and D. V. McGrath, *J. Am. Chem. Soc.*, 1999, **121**, 4912–4913.
- [118] A. Archut, F. Vögtle, L. De Cola, G. C. Azzellini, V. Balzani, P. S. Ramanujam, and R. H. Berg, *Chem. Eur. J.*, 1998, **4**, 699–706.
- [119] R. Herges and T. Winkler, *Eur. J. Org. Chem.*, 2001, pp. 4419–4422.
- [120] H. Morrison, *Biological Applications of Photochemical Switches*, John Wiley & Sons, New York, Chichester, Brisbane, Toronto, Singapore, 2 ed., 1993.
- [121] T. Nägele, R. Hoche, W. Zinth, and J. Wachtveitl, *Chem. Phys. Lett.*, 1997, **272**, 48.
- [122] I. K. Lednev, T.-Q. Ye, P. Matousek, M. Towrie, P. Foggi, F. V. R. Neuwahl, S. Umphathy, R. E. Hester, and J. N. Moore, *Chem. Phys. Lett.*, 1998, **290**, 68–74.

- [123] I. K. Lednev, T.-Q. Ye, L. C. Abbott, R. E. Hester, and J. N. Moore, *J. Phys. Chem. A*, 1998, **102**, 9161–9166.
- [124] Y. C. Lu, C. W. Chang, and E. W. G. Diau, *J. Chin. Chem. Soc.*, 2002, **49**, 693–701.
- [125] T. Pancur, F. Renth, F. Temps, B. Harbaum, A. Krueger, R. Herges, and C. Naether, *Phys. Chem. Chem. Phys.*, 2005, **7**, 1985–1989.
- [126] T. Fujino, S. Y. Arzhantsev, and T. Tahara, *Bull. Chem. Soc. Jpn.*, 2002, **75**, 1031–1040.
- [127] P. Bortolus and S. Monti, *J. Phys. Chem.*, 1979, **83**, 648–652.
- [128] S. Monti, G. Orlandi, and P. Palmieri, *Chem. Phys.*, 1982, **71**, 87–99.
- [129] W. Fuß, C. Kosmidis, W. E. Schmidt, and S. A. Trushin, *Chem. Phys. Lett.*, 2004, **385**, 423–430.
- [130] K. Ishii, S. Takeuchi, and T. Tahara, *Chem. Phys. Lett.*, 2004, **398**, 400.
- [131] T. Fujino, S. Y. Arzhantsev, and T. Tahara, *J. Phys. Chem. A*, 2001, **105**, 8123–8129.
- [132] T. Fujino and T. Tahara, *J. Phys. Chem. A*, 2000, **104**, 4203–4210.
- [133] T. Schultz, J. Quenneville, B. Levine, A. Toniolo, T. J. Martinez, S. Lochbrunner, M. Schmitt, J. P. Shaffer, M. Z. Zgierski, and A. Stolow, *J. Am. Chem. Soc.*, 2003, **125**, 8098–8099.
- [134] A. Stolow, *Annu. Rev. Phys. Chem.*, 2003, **54**, 89–119.
- [135] F. Renth unpublished results.
- [136] H. Satzger, C. Root, and M. Braun, *J. Phys. Chem. A*, 2004, **108**, 6265–6271.
- [137] P. Hamm, S. M. Ohline, and W. Zinth, *J. Chem. Phys.*, 1997, **106**, 519–529.
- [138] T. Kardinahl and H. Franke, *Appl. Phys. A*, 1995, **61**, 23–27.
- [139] F. M. Raymo and M. Tomasulo, *Chem. Soc. Rev.*, 2005, **34**, 327–336.
- [140] H. Stobbe, *Ber. Dtsch. Chem. Ges.*, 1905, **38**, 3673–3682.
- [141] M. Handschuh, M. Seibold, H. Port, and H. C. Wolf, *J. Phys. Chem. A*, 1997, **101**, 502–506.
- [142] O. Pieroni, A. Fissi, N. Angelini, and F. Lenci, *Acc. Chem. Res.*, 2001, **34**, 9.

- [143] A. S. Z. Janicki and G. B. jr. Schuster, *J. Am. Chem. Soc.*, 1995, **117**, 8524–8527.
- [144] J. Walz, K. Ulrich, H. Port, H. C. Wolf, J. Wonner, and F. Effenberg, *Chem. Phys. Lett.*, 1993, **213**, 321.
- [145] H. Port, M. Hennrich, M. Seibold, and H. C. Wolf, *Proceedings - Electrochemical Society*, 1998, **98-25**(Excitonic Processes in Condensed Matter), 61–70.
- [146] C. Lenoble and R. S. Becker, *J. Phys. Chem.*, 1986, **90**, 2651–2654.
- [147] H. G. Heller and J. R. Langan, *Journal of the Chemical Society, Perkin Transactions 2: Physical Organic Chemistry (1972-1999)*, 1981, pp. 341–343.
- [148] Y. Yoshioka and M. Irie, *Electron. J. Theor. Chem.*, 1996, **1**, 183–190.
- [149] Y. Yokoyama, S. Uchida, Y. Yokoyama, Y. Sugawara, and Y. Kurita, *J. Am. Chem. Soc.*, 1996, **118**, 3100–3107.
- [150] A. S. Dvornikov, Y. Liang, C. S. Cruse, and P. M. Rentzepis, *J. Phys. Chem.*, 2004, pp. 8652–8658.
- [151] H. Miyasaka, H. Masuhara, and N. Mataga, *J. Phys. Chem.*, 1985, **89**, 1631.
- [152] W. Radloff, V. Stert, T. Freudenberg, I. V. Hertel, C. Jouvét, C. Dedonder-Lardeux, and D. Solgadi, *Phys. Lett.*, 1997, **281**, 20.
- [153] W. Domcke, D. R. Yarkony, and H. Köppel, *Conical Intersections: Electronic Structure, Dynamics and Spectroscopy*, Eds. Scientific: Singapore, 2004.

## Acknowledgment

I feel lucky I had the chance to meet and work together with people that helped me to dive into the amazing world of science, always ready to support me during this fascinating excursion.

I would like to express my warm gratitude to Prof. Dr. F. Temps who offered me this possibility to step in the femto-laboratory. This was one of my biggest achievements so far and without the help of this great Professor I could never imagine that the science would capture me so much.

I thank to my advisor, colleague and friend Dr. F. Renth. Thank you Falk for your enormous contribution to the success of this work. Your support along these four years made my steps easier and safer. I thank you very much for days and nights spent in the lab.

It is my pleasure to continue with two friends and colleagues: Jens Riedel and Anke Petter. Your help for the success of this thesis is also invaluable. I could never reward your continuous support and warm words. Thank you Anke for being near me during the last four months. Jens, I wish you good luck for your thesis.

I want to thank Prof. Dr. H. Mäder for his enormously countable humor. His thrilling lectures showed me how wonderful the science is.

I want to thank our secretary Ms. U. von der Heydt at the Chair. Your good advices and nice smiles made me feel very comfortable.

I want to thank all my colleagues at the Chair: Harald Studzinski, Thomas Pancur, Nina Schwalb and all those we worked together. You all were very nice and I enjoyed the time with all of you. I have to mention here all my friends in Kiel and all over the world. They always brought a piece of "home" in my heart.

I always tried to make my way through chemistry and I thank for the help Dr. J. Gripp for his introduction into the mystery of chromatography. For implementation of all my crazy ideas I want to thank K. Warns and K. D. Will as well as the whole workshop team.

For his patience and support I want to thank my husband Eugen. He gave me an immeasurable moral support and let me feel proud to do science. Many thanks to his parents Nina and Valeriu Foca as well as his brother Adrian and his family for their care.

Finally I want to thank my sister Cornelia and my brother Sandel with his family for encouraging me to start this nice work.

After all, this work would be not imaginable without the support and help of my beloved parents Adriana and Ion Horoiu. I do not know how much they understood from what I did, but I continuously felt their great support and I will never be able to reward their enormous care. Romania is far, nevertheless their hearts beat always near me!



# Curriculum Vitae

## Personal Data

Name	Magdalena Foca (born Horoiu)
Date of birth	the 10 <sup>th</sup> of June, 1974
Place of birth	Scanteiesti, Romania
Citizenship	Romania
Parents	Adriana and Ion Horoiu

## Education

1980 - 1984	Primary School, Scanteiesti, Romania
1984 - 1988	Secondary School, Galati, Romania
1988 - 1992	Theoretical High School "Vasile Alecsandri", Galati, Romania
1992 - 1997	Studies at the Faculty of Physics, "Alexandru Ioan Cuza" University, Iasi, Romania
June 1997	State examination and diploma thesis at Faculty of Physics "Alexandru Ioan Cuza" University, Iasi, Romania
1997 - 1999	Master of Science at Faculty of Physics "Alexandru Ioan Cuza" University, Iasi, Romania
Since September 2001	PhD work at the Institute of Physical Chemistry of the Christian Albrechts University, Kiel, Germany
Supervisor:	Prof. Dr. F. Temps

## Professional activities

1997-1999	Physics teacher at the General school no. 18, Galati, Romania
1999-2001	Physics teacher at the "Traian" High School , Galati, Romania

Hiermit erkläre ich an Eides Statt, dass die vorliegende Abhandlung - abgesehen von Beratung durch meinen Betreuer Herrn Prof. Dr. F. Temps - nach Inhalt und Form meine eigene Arbeit ist. Ich habe bisher keinen Promotionsversuch unternommen.

Magdalena Foca